# ADVANCED MICROSTRUCTURAL CHARACTERIZATION OF HIGH STRENGTH LOW ALLOY STEELS

# ADVANCED MICROSTRUCTURE CHARACTERIZATION OF HIGH STRENGTH LOW ALLOY STEELS

BY

**CHEN GU, B.Eng., M.Eng.**

A Thesis Submitted to the School of Graduate Studies in Partial Fulfilment

of the Requirements for the Degree Doctor of Philosophy

McMaster University DOCTOR OF PHILOSOPHY (2023) Hamilton, Ontario

(Materials Science and Engineering)

TITLE: Advanced Microstructure Characterization of High Strength low alloy Steels

AUTHOR: Chen Gu

M.Eng. in Materials Science and Engineering (University of Science and Technology Beijing)

B.Eng. in Metallurgical Engineering (University of Science and Technology Beijing)

SUPERVISORS: Prof. Nabil Bassim & Prof. Hatem Zurob

Faculty of Engineering, McMaster University, Hamilton, Ontario, Canada

NUMBER OF PAGES: xxii, 216

# Abstract

Fine/nanoscale carbonitrides of microalloying elements such as Nb, Ti, and V play a significant role in the strengthening of HSLA steels. Site-specific analysis of the precipitates in different heterogeneous microstructural areas within realistic alloys is limited and the competition of different precipitates has not been discussed in detail. In this work, the relationship of precipitates/clusters with microstructure has been analyzed by site-specific methods and a simple model has been created to describe the competition between strain-induced precipitation and (Ti, Nb) (C, N).

Firstly, the spatial distribution of precipitates and microstructure heterogeneity in an X70 steel were investigated by site-specific analysis method. The quantitative analyze the precipitates reveals that strain-induced precipitation of fine NbC particles (5-20 nm) on dislocations was suppressed by the large (Ti, Nb) (C, N) precipitates. The similarity of precipitates in each location suggests that the local features (such as strain and grain size) in the final microstructure arise from phase transformations during cooling.

Secondly, the microstructural evolution during coiling and its effects on the mechanical properties of a vanadium microalloyed steel were investigated. Experimental findings showed that during holding at 500 ºC, nano precipitates (<10 nm) containing V and N nucleated heterogeneously, primarily in areas with high Kernel Average Misorientation (KAM) values. These areas contained a larger number of dislocations, which acted as

nucleation sites for the precipitates. The effect of precipitation strengthening was not significant and was offset by softening caused by the aging of bainite and associated recovery of dislocations.

Thirdly, in the HSLA steel with both V and Nb additions, nano precipitates were found to preferentially form around dislocations and grain/sub-grain boundaries in high KAM areas associated with bainite. Precipitates were frequently observed around cementite in low KAM areas, which were identified as granular bainite. Interphase clusters were also discovered in low KAM areas behind the ferrite/austenite interface. Analysis of the results indicated that the precipitation of micro-alloyed particles on cementite may reduce the contribution of precipitation hardening achievable through microalloying.

Finally, a competition model between strain-induced precipitates (SIP) and epitaxial growth in micro-alloyed austenite has been developed. Using this model, it is possible to estimate the effects of process parameters (T, applied strain), the number density of pre-existing TiN particles, and steel composition on the precipitation process.

Through the various studies achieved here, the aim to understand the relationship between the precipitates and different microstructures and develop the competition models has been accomplished. These works provide a relatively new workflow to investigate the precipitates within the steel, especially in site-specific areas, and also allow us to predict the precipitation of NbC by selecting desired temperature range, applied strain, and number density of pre-existing TiN precipitates.

# Acknowledgments

I would like to express my deepest appreciation to my supervisors Dr. Hatem Zurob and Nabil Bassim for their guidance, constant support, and encouragement throughout my Ph.D. work. I appreciate the time and funding that they have generously dedicated to my work to perform many interesting experiments and the most expensively exciting analytical microscopy. I would like to sincerely thank my supervisory committee member Dr. Colin Scott for his helpful suggestions and discussions. The fruitful discussions with Prof. Yves Brechet are also gratefully appreciated.

Many thanks to Dr. Carmen Andrei, Dr.Gabriel Arcuri, Chris Butcher, Travis Casagrande, Dr. Natalie Hamada, Dr. Brian Langelier, Jhoynner Martinez, Andy Duft, Dr. Xiang Wang and Dr. Hui Yuan of the Canadian Centre of Electron Microscopy, for the electron microscopy/sample preparation training and for their generosity in sharing their insight and knowledge with me. I would also like to thank Dr. Xiaogang Li and Doug Culley for their help with sample preparation and heat treatment, and Ed McCaffery for technical assistance.

I would also like to acknowledge the sponsorships from EVRAZ North America steel corporations through an NSERC CRD Grant. Discussions with Dr. Michael J. Gaudet and Jing Su are much appreciated, thanks for their insightful comments and suggestions. I am grateful to Dr. Fateh Fazeli and Dr. Shalchi Amirkhiz, Babakgreatly from CanmetMATERIALS (Hamilton, Canada) for the dilatometer experiment and TEM

characterization. I am also very grateful to Mary-Anne Bechamp and Samantha Kandilas for having things organized and providing the best working environment.

Furthermore, I would also like to express thanks to my colleagues for the cherished time spent together in the JHE and CCEM. I also appreciate all the other colleagues, friends, staff, and professors from McMaster University, especially from the Department of Materials Science and Engineering, for their assistance and guidance and for being part of my Ph.D. journey.

Lastly, I wish to conclude by expressing my warmest gratitude to my parents, husband, and whole family for their infinite love and support. Their tremendous understanding and encouragement over the past few years gave me the strength and power to accomplish this research.

.

# Table of Contents

# List of Figures

# List of Tables



**Table 4- 1. Summary of mechanical properties of S1, S2, S3 and S4.**..... 108

# List of Abbreviations and Symbols

| Abbr. | Full Description |
|---|---|
| ADF | Annular Dark-Field |
| AF | Acicular Ferrite |
| AHSS | High Strength Steel |
| APT | Atom Probe Tomography |
| BF | Bainitic Ferrite |
| BH | Bake Hardened |
| CBED | Convergent Beam Electron Diffraction |
| CCT | Continuous Cooling Transformation |
| CLSM | Confocal Laser Scanning Microscopy |
| $C_{Nb}$ | Instantaneous Concentration of Nb |
| CNT | Classical Nucleation Theory |

| | |
|---|---|
| DP | Dual-Phase |
| EBSD | Electron Backscatter Diffraction |
| EBSP | Electron Backscatter Pattern |
| EDM | Electrical Discharge Machining |
| EDS | Energy Dispersive Spectroscopy |
| EDX | Energy Dispersive X-Ray |
| EELS | Electron Energy Loss Spectroscopy |
| FIB | Focus Ion Beam |
| GB | Granular Bainite |
| GND | Geometrically Necessary Dislocations |
| GP | Guinier–Preston |
| HAADF | High-Angle Annular Dark-Field |
| HB | High Base |
| HOLZ | Higher-Order Laue Zones |
| HOP | Online Heat-Treatment Process |

| | |
|---|---|
| HRTEM | High-Resolution Transmission Electron Microscopy |
| HSLA | High-Strength Low-Alloy Steel |
| HSS | High Strength Steel |
| HT | High Temperature |
| IGF | Intragranular Acicular Ferrite |
| KAM | Kernel Average Misorientation |
| $K_B$ | Boltzmann Constant |
| LB | Low Base |
| LEAP | Local Electrode Atom Probe |
| $M_T$ | Taylor Factor |
| NBD | Nano-Beam Diffraction |
| ND | Normal Direction |
| OM | Optical Microscope |
| PF | Polygonal Ferrite |

| | |
|---|---|
| PFIB | Plasma Focused Ion Beam |
| RD | Rolling Direction |
| ROI | Region Of Interest |
| SAD | Selected Area Diffraction |
| SAED | Selected Area Electron Diffraction |
| SEM | Scanning Electron Microscope |
| SIP | Strain Induced Precipitates |
| STEM | Scanning Transmission Electron Microscopy |
| TD | Transverse Direction |
| TEM | Transmission Electron Microscopy |
| TMP | Thermo-Mechanically Processing |
| TOF | Time-Of-Flight |
| TTT | Time-Temperature-Transformation |
| XRD | X-Ray Diffraction |
| YS | Yield Strength |

| | |
|---|---|
| $YS_B$ | Yield Strength of Bainite |
| $YS_F$ | Yield Strength of Ferrite |

# Chapter 1 Introduction

## 1.1 Background

Steel design has increasingly focused on the enhancement of strength without compromising ductility. According to a general classification based on strength, steels can be divided into low-strength steels; conventional High strength steel (HSS), and advanced high-strength steel (AHSS) [1-3]. High strength low alloy steel (HSLA) with limited alloy elements (such as niobium, titanium, vanadium, and aluminum) is a category of conventional HSS with ~ 550 MPa yield strength. HSLA has higher mechanical resistance and yield strength, low impact transition temperature, and good weldability compared to conventional carbon steels. These mechanical properties enable it to be widely used in oil and gas pipelines, automobile components, etc.[2-8]. Steelmakers can change many parameters of the manufacturing process, such as the alloy composition or thermo-mechanical processing (TMP), to improve the strength and ductility of steel.

Most steels use a variety of strengthening methods (like solid solution strengthening, grain refinement, work hardening, transformation strengthening, precipitation hardening, etc.) to produce the composite strengthening effect[5]. Precipitation hardening plays the main role in the strengthening of HSLA, which is achieved by the formation of complex precipitates of the type MX, where M is an alloying element (like Ti, Nb, and/or V) and X is C and/or N[2, 9, 10].

It is reported that a change in composition or the processing conditions can affect the onset and kinetics of precipitation and ultimately microstructure refinement[5]. Different microstructures will also influence the strength thus it is also important to understand the kinetics of phase transformations in HSLA steels to design and obtain optimal microstructures. Besides that, nano-scale precipitation and cluster-strengthened steels have drawn increasing attention due to their excellent mechanical properties[1, 11, 12]. But the early stages of precipitation and cluster formation are not very well understood.

Due to the small volume fraction and size (less than 10 nm) of nanoprecipitation and clusters, traditional characterization techniques (Scanning Electron Microscope or Transmission electron microscopy) cannot provide statistical information related to precipitation. Correlative use of Atom Probe Tomography and other electron microscopy techniques (Scanning Transmission electron microscopy, High resolution-TEM, etc) will help us to distinguish clustering and precipitation and enable a better understanding of the morphology of nano precipitates, clusters, and their relationships in HSLA steels. It is worth mentioning that other analysis techniques such as selective chemical dissolution and inductively coupled plasma mass spectrometry (ICP-MS) method analysis (for precipitate volume fraction data), and small-angle neutron scattering ( for particle size distributions) are also used in the study of precipitates. In most of the existing literature, precipitates in micro-alloyed steels have been investigated extensively using TEM. However, the analysis is carried out either on thin TEM foils prepared by electropolishing or as carbon extraction replicas from polished surfaces[13-26]. Other Due to the limitations of these sample

preparation methods, the precipitates/clusters analyzed in most of the literature are hard to be site-specific. Thus, precipitates/clusters in different regions within the microstructure have not been investigated and discussed in detail. A site-specific characterization method brings insights into precipitation/cluster characteristics with respect to the local microstructure features.

Besides, the absence of strain-induced precipitation of NbC is frequently observed in conventional Nb-Ti micro-alloyed steel[3, 27]. The competition between TiN and NbC in Nb+Ti steel has not been well established/discussed yet[28-30].

Based on these facts, this project is initiated to have a better and deeper understanding of microstructure (ferrite, cluster, precipitates, and dislocation) in HSLA steel by advanced techniques, such as CLSM, and the correlative use of EBSD, APT, and TEM. A new model has also been constructed to describe the competition between SIP and pre-existing TiN precipitates.

## 1.2 Thesis outline

Following the regulations of McMaster University, this research project is presented in a sandwich thesis format, containing 4 coherent, peer-reviewed, scholarly works between an introductory chapter outlining the general background and objectives and a final conclusive chapter describing the engineering and scientific achievements of the research. A summary of the contents of each chapter is provided below:

**Chapter 1** is an introductory chapter that outlines the research theme, relevant background, and general research objectives.

**Chapter 2** is a comprehensive literature review chapter that covers the fundamental background, microstructure, precipitates of HSLA, and advanced characterization techniques for the analysis of precipitates. An overview of the significance of precipitate strengthening in HSLA is outlined. The advantages and wide-ranging applications of different characterization techniques are reviewed thoroughly.

**Chapter 3** is the first published, peer-reviewed article, *"Advanced Characterization of Precipitation and Microstructure Heterogeneity in X70 Steel"*. This paper investigates the spatial distribution of precipitates and microstructure heterogeneity in an X70 steel by using advanced characterization techniques (EBSD, FIB, APT, TEM). Quantitative analysis by TEM and 3D atom probe tomography (APT) revealed that strain-induced precipitation of fine (5-20 nm) NbC particles was suppressed by uniformly dispersed (Ti,Nb)(C,N). The absence of strain-induced precipitation was discussed. The similarity of precipitates in each location suggests that the local features (strain, grain size) in the final microstructure arise from phase transformations during cooling.

**Chapter 4** *"Evolution of the Microstructure and Mechanical Properties of a V-Containing Microalloyed Steel During Coiling"*. This chapter is to understand the microstructural evolution during coiling and its effects on the mechanical properties of vanadium microalloyed steel. Experimental results demonstrated that nano precipitates (VN, <10 nm)

nucleated during holding at 500 ºC were more commonly found in areas with a high value of the Kernel Average Misorientation (KAM) because these areas have a larger number of dislocations which act as nucleation sites for the precipitates. The evolution during coiling of the mechanical properties and their relationship with the microstructure are investigated and discussed. This work was accepted by Materials Science and Engineering A.

**Chapter 5** *Site-specific Analysis of Precipitates During the Coiling of an HSLA Steel Containing V and Nb*. In this chapter, precipitation during coiling at 500 ºC, was investigated by advanced characterization techniques including EBSD, FIB, TEM, and EBSD in an HSLA steel containing V and Nb additions. During coiling, nano precipitates are distributed heterogeneously in the studied material. The results indicate that variations in the spatial distribution of precipitates are due to variations in the microstructure formed during cooling to the coiling temperature. Analysis of the results indicates that the precipitation of micro-alloyed particles on cementite may lower the precipitation hardening contribution that could be achieved by microalloying. This work is under review in the Journal of Materials Research and Technology.

**Chapter 6** *A Model for the Competition between Strain-Induced Precipitates and Epitaxial Growth in Microalloyed Austenite*. This chapter introduced the model developed for describing the competition of strain-induced precipitates (SIP) and TiN in Microalloyed Austenite. This model is successfully applied to an extensive data set obtained by transmission electron microscopy (TEM) for a given alloy content. Given the alloy composition, the model is able to predict the precipitation of NbC by selecting desired

temperature range, applied strain, and number density of pre-existing TiN precipitates. This work is under review in the Journal of Materials Research and Technology.

**Chapter 7** is a concluding chapter that summarizes the important findings from each of the previous chapters and discusses the significance of these conclusions. Finally, future work drawing on these conclusions is proposed and outlined.

## 1.3 References

[1] S. Mukherjee, I. Timokhina, C. Zhu, S.P. Ringer, P.D. Hodgson, Clustering and precipitation processes in a ferritic titanium-molybdenum microalloyed steel, Journal of Alloys and Compounds 690 (2017) 621-632.

[2] V.M.H. KONSTRUKCIJSKA, High-strength low-alloy (HSLA) steels, Materiali in tehnologije 45(4) (2011) 295-301.

[3] B. Ma, A study of processing, microstructure and mechanical properties of ultra-high strength microalloyed steel hot band coils for automotive applications, University of Pittsburgh, 2017.

[4] W. Bleck, E. Ratte, Fundamentals of Cold Formable HSLA Steels, International Symposium on Niobium Microalloyed Sheet Steel for Automotive Application, S. Hashimoto, S. Jansto, H. Mohrbacher, F. Siciliano, Eds. TMS (The Minerals, Metals & Materials Society), 2006, pp. 551-564.

[5] T. Gladman, The physical metallurgy of microalloyed steels, Maney Pub1997.

[6] A. Davenport, L. Brossard, R. Miner, Precipitation in microalloyed high-strength low-alloy steels, JOM 27(6) (1975) 21-27.

[7] M. Charleux, W. Poole, M. Militzer, A. Deschamps, Precipitation behavior and its effect on strengthening of an HSLA-Nb/Ti steel, Metallurgical and Materials Transactions A 32 (2001) 1635-1647.

[8] D. Belato Rosado, W. De Waele, D. Vanderschueren, S. Hertelé, Latest developments in mechanical properties and metallurgical features of high strength line pipe steels, 5th

International Conference on Sustainable Construction and Design, Ghent University, Laboratory Soete, 2013.

[9] H.J. Kong, C.T. Liu, A review on nano-scale precipitation in steels, Technologies 6(1) (2018) 36.

[10] T. Gladman, Precipitation hardening in metals, Materials science and technology 15(1) (1999) 30-36.

[11] Z. Xiong, I. Timokhina, E. Pereloma, Clustering, nano-scale precipitation and strengthening of steels, Progress in Materials Science 118 (2021) 100764.

[12] K.Y. Xie, T. Zheng, J.M. Cairney, H. Kaul, J.G. Williams, F.J. Barbaro, C.R. Killmore, S.P. Ringer, Strengthening from Nb-rich clusters in a Nb-microalloyed steel, Scripta Materialia 66(9) (2012) 710-713.

[13] C. Klinkenberg, K. Hulka, W. Bleck, Niobium carbide precipitation in microalloyed steel, steel research international 75(11) (2004) 744-752.

[14] Z. Jia, R. Misra, R. O'malley, S. Jansto, Fine-scale precipitation and mechanical properties of thin slab processed titanium–niobium bearing high strength steels, Materials Science and Engineering: A 528(22-23) (2011) 7077-7083.

[15] F. Bu, X. Wang, S. Yang, C. Shang, R. Misra, Contribution of interphase precipitation on yield strength in thermomechanically simulated Ti–Nb and Ti–Nb–Mo microalloyed steels, Materials Science and Engineering: A 620 (2015) 22-29.

[16] H.-J. Kestenbach, S. Campos, E. Morales, Role of interphase precipitation in microalloyed hot strip steels, Materials science and technology 22(6) (2006) 615-626.

[17] H. Dong, H. Chen, W. Wang, Y. Zhang, G. Miyamoto, T. Furuhara, C. Zhang, Z. Yang, S. van der Zwaag, Analysis of the interaction between moving α/γ interfaces and interphase precipitated carbides during cyclic phase transformations in a Nb-containing Fe-C-Mn alloy, Acta Materialia 158 (2018) 167-179.

[18] S. Clark, V. Janik, A. Rijkenberg, S. Sridhar, Analysis of the extent of interphase precipitation in V-HSLA steels through in-situ characterization of the γ/α transformation, Materials Characterization 115 (2016) 83-89.

[19] A. Davenport, F. Berry, R. Honeycombe, Interphase precipitation in iron alloys, Metal Science Journal 2(1) (1968) 104-106.

[20] R. Okamoto, A. Borgenstam, J. Ågren, Interphase precipitation in niobium-microalloyed steels, Acta Materialia 58(14) (2010) 4783-4790.

[21] S. Liang, X. Wang, C. Andrei, H.S. Zurob, NbC precipitation during two-pass hot deformation of a nickel-based model alloy at 700° C: Experiments and modelling, Materials Science and Engineering: A 802 (2021) 140447.

[22] S. Liang, X. Wang, H.S. Zurob, NbC precipitation during multi-pass deformation of a nickel-based model alloy: Experiments and modelling, Materials Science and Engineering: A 772 (2020) 138748.

[23] B. Dutta, E.J. Palmiere, C.M. Sellars, Modelling the kinetics of strain induced precipitation in Nb microalloyed steels, Acta materialia 49(5) (2001) 785-794.

[24] P. Gong, E.J. Palmiere, W.M. Rainforth, Characterisation of strain-induced precipitation behaviour in microalloyed steels during thermomechanical controlled processing, Materials Characterization 124 (2017) 83-89.

[25] D. Poddar, P. Cizek, H. Beladi, P.D. Hodgson, Evolution of strain-induced precipitates in a model austenitic Fe–30Ni–Nb steel and their effect on the flow behaviour, Acta materialia 80 (2014) 1-15.

[26] V. Challa, W. Zhou, R. Misra, R. O'Malley, S. Jansto, The effect of coiling temperature on the microstructure and mechanical properties of a niobium–titanium microalloyed steel processed via thin slab casting, Materials Science and Engineering: A 595 (2014) 143-153.

[27] C. Gu, M.J. Gaudet, J. Su, B. Langelier, H. Yuan, N. Bassim, H. Zurob, Advanced Characterization of Precipitation and Microstructure Heterogeneity in X70 Steel, Metallurgical and Materials Transactions A (2022) 1-8.

[28] X. Ma, C. Miao, B. Langelier, S. Subramanian, Suppression of strain-induced precipitation of NbC by epitaxial growth of NbC on pre-existing TiN in Nb-Ti microalloyed steel, Materials & Design 132 (2017) 244-249.

[29] F. Perrard, A. Deschamps, P. Maugis, Modelling the precipitation of NbC on dislocations in α-Fe, Acta Materialia 55(4) (2007) 1255-1266.

[30] A. Deschamps, Y. Brechet, Influence of predeformation and ageing of an Al–Zn–Mg alloy—II. Modeling of precipitation kinetics and yield stress, Acta Materialia 47(1) (1998) 293-305.

# Chapter 2 Literature Review

## 2.1 Introduction of HSLA

### 2.1.1 Composition

Steel is a major structural material for the transportation and construction sectors. It can be divided into three major categories according to its strength: low-strength steels; conventional high-strength steel (HSS); and the new advanced high-stress steel (AHSS)[1-3]. Conventional HSS includes BH (bake-hardened), carbon-manganese, and HSLA (high-strength low-alloy)[4]. The material used in this project is HSLA steel with microalloying additions. HSLA usually contains 0.05–0.25% carbon content and small amounts of alloy elements (<0.1%), such as Nb, V, Ti, and Al, which improve the strength by the formation of stable carbides (NbC, VC, TiC, etc), nitrides (TiN, NbN, etc) or carbonitrides (Ti, Nb)(C, N). The alloying elements frequently used in HSLA steels are shown in **Table 2- 1**.

**Table 2- 1. Alloying elements frequently used in HSLA steels [5]**

| Element | Amount in HSLA/wt-% | Influence |
|---|---|---|
| C | <0·25 | Strengthener |
| Mn | 0·5–2 | Delays austenite decomposition during accelerated cooling[22] |
| | | Mild solid solution strengthener |
| | | Decreases ductile to brittle transition temperature |
| Si | 0·1–0·5 | Deoxidiser in molten steel |
| | | Solid solution strengthener |
| Al | >0·02 | Deoxidiser |
| | | Limits grain growth (AlN) |
| Nb | 0·02–0·06 | Very strong ferrite strengthener [Nb(C,N)] |
| | | Grain size control |
| | | Delays $\gamma$ to $\alpha$ transformation |
| Ti | 0–0·06 | Grain size control (TiN formation) |
| | | Strong ferrite strengthener |
| V | 0–0·1 | Strong ferrite strengthener (VN) |
| N | <0·012 | Forms TiN, VN and AlN |
| Mo | 0–0·3 | Promotes bainite formation |
| | | Ferrite strengthener |
| Ni | 0–0·5 | Increases fracture toughness |
| Cu | 0–0·55 | Improves corrosion resistance |
| | | Ferrite strengthener |
| Cr | 0–1·25 | Improves atmospheric corrosion resistance (when Cu is also added) |

### 2.1.2 Development and Applications

The trend of improving the strength and other properties has led to a major increase in research to develop HSLA, which provides increased strength with equivalent, or improved, ductility. The developments in micro-alloyed steels from 1940 to 2000 are summarised in **Figure 2- 1Figure 2- 1. Development in micro-alloyed steels [5].**

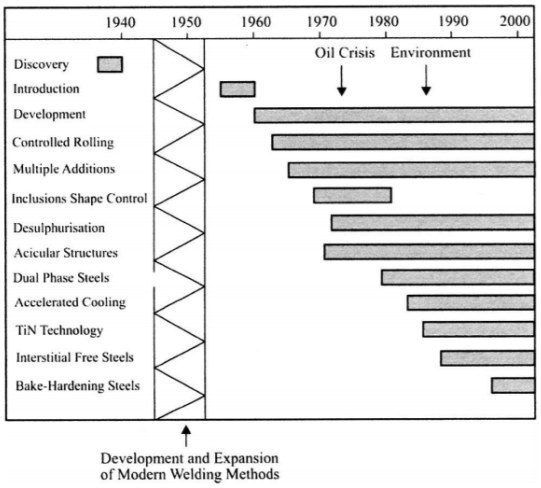


**Figure 2- 1. Development in micro-alloyed steels [5].**

HSLA includes weathering steels, micro-alloyed ferrite-pearlite steels, as-rolled pearlitic steels, acicular ferrite (low-carbon bainite) steels, dual-phase steels, and inclusion-shape-controlled steels. Compared to conventional carbon steels, HSLA has higher yield strength, good weldability, and low impact transition temperature. It has been widely used in oil and gas pipelines (such as API 5L steel grades), automobile components(due to favorable strength-to-weight ratio), storage tanks(ASTM A573), construction and farm machinery, industrial equipment, etc.[1, 2]. **Table 2- 2** shows the mechanical properties of pipeline steels, which is a category of HSLA. The two-digit number following the "X" indicates the Minimum Yield Strength (in 000's psi) of pipe produced to this grade.

**Table 2- 2. Mechanical properties of different pipeline steels[4].**

| Grade | YS/MPa | TS/MPa | YR/% | El% |
|---|---|---|---|---|
| X65 | ⩾448 | ⩾530 | ⩽90 | ⩾24 |
| X70 | ⩾482 | ⩾565 | ⩽90 | ⩾23 |
| X80 | ⩾551 | 620–827 | ⩽93 | ⩾22 |
| X100 | ⩾690 | ⩾760 | 90 | |
| X120 | ⩾883 | ⩾1023 | 90 | |

### 2.1.3 Strengthening Mechanisms.

Hardening mechanisms are often used in a variety of combinations to achieve the desired performance, especially yield strength in steels. These mechanisms typically work by blocking the motion of dislocations in the steel and include grain refinement, precipitation hardening, solid solution strengthening, work hardening, transformation strengthening, and

texture strength[4]. The main strengthening mechanisms in HSLA are grain refinement, precipitation hardening, solid solution strengthening, and dislocation strengthening. The effect of different mechanisms on the strength increment is shown in **Figure 2- 2**.

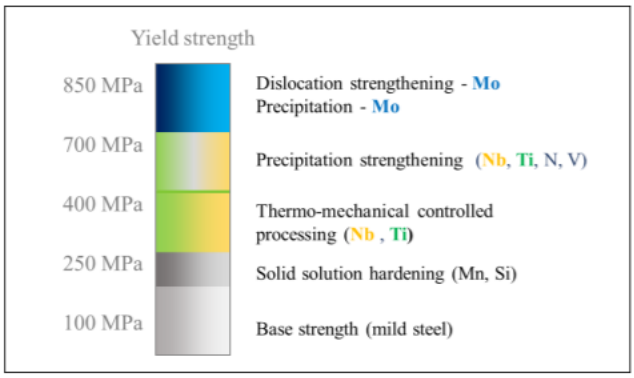


**Figure 2- 2. Strength contribution of HSLA steel [6].**

### *2.1.3.1. Grain refinement*

Dislocations tend to pile up at grain boundaries and prevent further plastic deformation when they travel through a material. The effective area of grain boundaries will increase with the reduction of grain size decreases, thus both the strength and toughness (though toughness may be lowered below a critical grain size.) of the material will be increased. Hall-Petch equation ($\sigma 0=\sigma t+k_0 \times d^{-1/2}$ (Equation 2- 1)) is usually used to describe the quantitative relationship between grain size and yield strength in metals[7]:

$$\sigma_0 = \sigma_t + k_0 \times d^{-1/2} \quad \text{(Equation 2- 1)}$$

where:

$\sigma_0$ – yield strength

$\sigma_t$ – yield strength of a single crystal

$k_0$ – constant, Hall-Petch factor

d – grain size

### *2.1.3.2. Solid solution strengthening:*

Interstitial solid solution strengthening from the C atom is one of the most economic and the most effective strengthening method in steel materials. Solid solution strengthening of other soluble atoms is also widely used in steel [4]. Interstitial or substitutional impurities distort the lattice and generate stress, which can interact with dislocation strain fields and hinder dislocation motion. Alloys for solid solution strengthening including silicon, manganese, chromium, copper, and nickel, etc. The contribution of solid solution strengthening to the yield stress of ferrite has been estimated from the literature [8-11]:

$$\sigma_0 + \sigma_{ss} + \sigma_{iss}\ [\text{MPa}] = 54+32\text{Mn}+83\text{Si}+678\text{P}+39\text{Cu}+31\text{Cr}+11\text{Mo}+5000(C_{free} + N_{free}) \quad \text{(Equation 2- 2)}$$

where the solute content is expressed in mass%.

### *2.1.3.3. Dislocation strengthening*

When a dislocation glides, its strain field will interact with those of adjacent dislocations in a variety of ways to prevent its movement and thus improve strength, which is called dislocation strengthening. Dislocation strengthening can improve both the yield strength and the tensile strength of the material when the dislocation density is low, while it mainly improves the yield strength of the material when the dislocation density is high and has

little effect on the tensile strength. Many important theories have been proposed to explain the mechanism of dislocation strengthening, including forest dislocation theory, long-term stress field theory, tangled dislocation network length theory (Mesh length), dislocation Pile-up, dislocation theory of cross-section (Intersection), jog, etc.[12]. The contribution of dislocations to the strength is calculated using the Taylor equation[7, 8, 10]:

$$\sigma_d = \alpha M \mu b \rho^{0.5} \approx 7.34 \times 10^{-6} \rho_D^{0.5} \qquad \text{(Equation 2- 3)}$$

where α is a constant, M is the average Taylor factor, and αM = 0.38. The shear modulus, μ, is approximated as $8\times10^4$ MPa and b is the magnitude of the Burgers vector ($b\approx2.5\times10^{-10}$ m).

#### *2.1.3.4. Precipitation hardening*

The second phase precipitates will form when alloying in a material is above a specific solubility concentration given by the phase diagram. The tiny second-phase precipitates will act as pinning points to dislocation motion, similar to solute atoms. Precipitation strengthening depends on how dislocations interact with precipitates[13]. Two mechanisms (the precipitate shearing mechanism and the Orowan looping mechanism[14]) are used to explain the interaction between precipitates and dislocation, as shown in **Figure 2- 3**. Dislocations can travel through the precipitates easily when the precipitates are small, which is known as the precipitate shearing mechanism. When the particle exhibits relative "softness," the dislocation shears the particle, resulting in various forms of strengthening, including chemical strengthening, stacking fault strengthening, coherency strengthening,

modulus strengthening, and order strengthening. As the dislocation cuts through the particle, it generates ledges at the particle/matrix interface upon entry and exit. The creation of additional interfaces between the matrix and particle increases the interfacial energy and, consequently, enhances the resistance against the dislocation's motion. This phenomenon contributes to the mechanism of chemical strengthening, which can be expressed as[14]:

$$\Delta\tau_{chemical} = \frac{\sqrt{\gamma}}{b} \times (\frac{4rf}{\pi T})^{1/2} \quad \text{(Equation 2- 4)}$$

where γ is interfacial energy and T is the line tension of dislocation (usually taken to be $Gb^2/2$. f is the volume fraction of the precipitates; r is the radius of the precipitates.

When the precipitates are large, Orowan looping mechanism takes place, as dislocations can not cut through the incoherent precipitates[15-19]. The precipitation hardening contribution to yield strength was estimated by the modified Ashby-Orowan formula [20, 21] as:

$$\sigma_p = 10.8\frac{\sqrt{f}}{d}\ln(1630d) \quad \text{(Equation 2- 5)}$$

where $\sigma_p$ represents the precipitation strengthening increment in MPa, and d is the diameter(μm) of the precipitates.

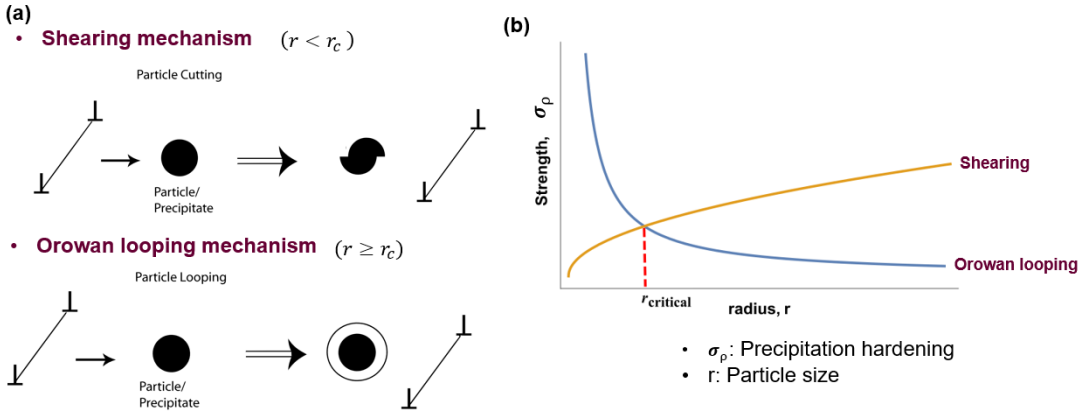


**Figure 2- 3 (a)Schematic of the shearing mechanism and the Orowan looping mechanism (b)two stages for a characteristic one-peak precipitation-strengthening curve [14].**

Precipitation strengthening is a very important method in steel and remains an area of active research and technological development. Various precipitates(TiN, NbC, (Nb, Ti)(C, N), Cu, etc.), which play a very important role in stabilizing the microstructure, grain refinement, and suppressing the recrystallization of steels[22], have been used to improve the strength in high-grade steels (>1 GPa)[23]. This project will focus on the precipitate strengthening in the steel.

In summary, the strengthening effect produced by a single strengthening method is limited, or it will be saturated after the strengthening effect reaches a certain degree. Therefore, most steel materials use a variety of strengthening methods to produce a composite strengthening effect, which gives rise to the superposition of the strengthening effect of various strengthening methods.

### 2.1.4 Processing of High-Strength Low-Alloy Steel (HSLA)

HSLA is produced by controlling thermo-mechanical processing parameters and chemical composition from the austenite or austenite plus ferrite phase, to meet mechanical property requirements. These mechanical properties depend upon microstructural features, while weldability is usually influenced by composition[2]. Microalloying elements affect ferrite microstructure in several ways, such as altering transformation temperature[5]. It is also reported that the low alloy element will influence the nucleation of precipitates in steel and then affect the mechanical properties.

Thermo-mechanical processing (TMP), which can improve the toughness and strength of steels by grain refinement, is one of the most simple and cost-effective ways to produce HSLA. First, the steel will be heated above the transformation temperature and then rolled on a hot strip mill, after multi-pass rolling, the sheet will be water-cooled on the run-out table before being coiled[1-3, 24]. The microstructure will be changed at different controlled-rolling stages. Typically, TMP includes 3 main processing stages: reheating and soaking, roughing and finishing rolling, controlled cooling, and coiling. The typical mill layout for the TMP process is shown in **Figure 2- 4** and typical temperatures and features of TMP are shown in **Table 2-3**.

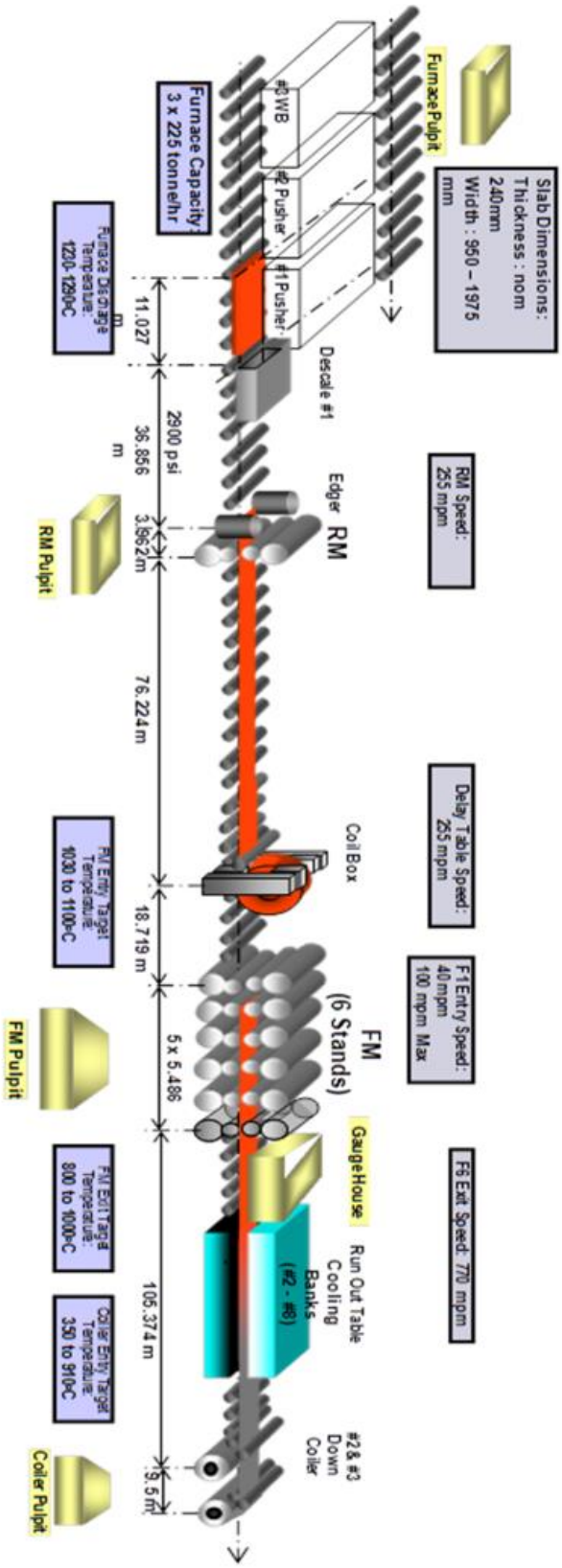
Furnace Pulpit
Slab Dimensions:
Thickness : nom
240mm
Width : 960 – 1975
mm
#2 WB
#2 Pusher
#1 Pusher
Furnace Capacity:
3 x 225 tonne/hr
Furnace Discharge
Temperature:
1220-1290oC
11.027 m
Descale #1
2900 psi
36.856 m
Edger
RM
RM Speed:
25 mpm
3.962m
RM Pulpit
76.224 m
Delay Table Speed:
25 mpm
Coil Box
FM
(6 Stands)
F1 Entry Speed:
40 mpm
100 mpm Max
F6 Exit Speed: 770 mpm
FM Entry Target
Temperature:
1030 to 1100oC
18.719 m
5 x 5.486
FM Pulpit
GaugeHouse
Run Out Table
Cooling
Banks
(#2 - #8)
FM Exit Target
Temperature:
800 to 1000oC
105.374 m
Coiler Entry Target
Temperature:
350 to 910oC
#2 & #3
Down
Coiler
9.5 m
Coiler Pulpit

**Figure 2- 4. Schematic of typical mill layout[24].**

**Table 2-3. Overview of TMP stages, typical temperatures and features[25]**

| **Processing Parameters** | **Features** |
|---|---|
| Reheating (+ soaking): 1250℃ and 1300℃ | • Austenitization<br>• Getting the desired microstructure<br>• Dissolve the microalloying precipitates, so that all the solutes stay in the solution. |
| Roughing rolling (1150℃ to 1050℃） | • Several passes and relatively high reductions are applied to break down the as-cast microstructure and remove heterogeneities of the microstructure.<br>• Reduction ratio (%) 40-75<br>• repeated grain refinement by recrystallization. |
| Finishing rolling (low-temperature austenite region (between Tnr1 and Ar3) | • Strain accumulation<br>• formation of pancaked grains and deformation bands<br>• Produce a fine, polygonal austenitic grain.<br>• Maintain within the range of the Tnr and Ar3; |
| Cooling (~700℃, 20-50℃/s) | • Enhances grain refinement of ferrite.<br>• Prevents formation of pearlite during cooling.<br>• Formation of SIP |
| Coiling (~600℃) | • Reduce excess hardness and residual stresses.<br>• Formation of matrix precipitates |

#### *2.1.4.1. Reheating and soaking*

In order to get the desired microstructure and dissolve the microalloying precipitates, the cast slab will be austenitized to a temperature between 1250℃ and 1300℃ first. Then the whole slab will be soaked for a long time. Soaking time and temperature are very important parameters to be controlled. The austenite grain size has an exponential relationship with the soaking temperature. Therefore, in order to control the grain size, the lowest soaking temperature should be used to dissolve microalloying elements while maintaining a small austenite grain size. Usually, the soaking temperature is determined by the niobium, titanium (TiN is very stable), and carbon contents for most steel grades.

#### *2.1.4.2. Roughing and finish rolling*

A two-step rolling process is typically conducted after a long soaking time.

The first is roughing rolling: the slab will be cooled down to temperatures from 1150℃ to 1050℃, which breaks down the as-cast microstructure and removes heterogeneities of the microstructure by several passes and relatively high reductions. The entry temperature and reduction for each pass will influence the final austenite grain size before being transferred to the finishing rolling stage.

In the finishing rolling stage, the grain size is ready for pancaking and strain accumulation. Complete static recrystallization no longer takes place between rolling passes (due to the temperature range). In the low-temperature austenite region (between the non-

recrystallization temperature $T_{nr1}$ and the austenite transformation temperature $A_{r3}$), the formation of pancaked grains and deformation bands will cause strain retention during deformation. As a result, the number of nucleation sites (for the γ to α transformation) is increased, which promotes grain size reduction, and thus improves both strength and toughness.

#### *2.1.4.3 Controlled cooling and coiling*

Most of the precipitates that account for precipitation strengthening form during the cooling and coiling process. So the cooling and coiling conditions exert a major effect on the final microstructure and hence the mechanical properties[25].

The cooling process is essentially determined by the requirements of the final products from customers. **Figure 2- 5** shows the influence of accelerated cooling during controlled rolling. Further grain refinement can be achieved by employing faster cooling rates, which lowers the transformation start temperature and thus provides more nuclei in the undercooled austenite. Ferrite–pearlite microstructure (providing a yield strength level of about 500 MPa) forms with air cooling, ferrite and bainite (or bainite and martensite, provide about 700 MPa yield strength) appear in the accelerated cooling.

After controlled cooling, the steel sheets will be coiled, which influences the strength of HSLA. The reactions within the coil can be assumed to be isothermal because of the large thermal mass of the coil. During the coiling process, the size of precipitates will be

increased with the increase in temperatures and holding times. The precipitation strengthening increment is strongly affected by the coiling temperature[3]. The shape of the precipitates and the number of atoms within each precipitate will also change over coiling time[1]. In order to achieve consistent mechanical properties, controlling of coiling temperatures (within-coil and from the coil to coil, finishing temperature) and coiling time are very important.

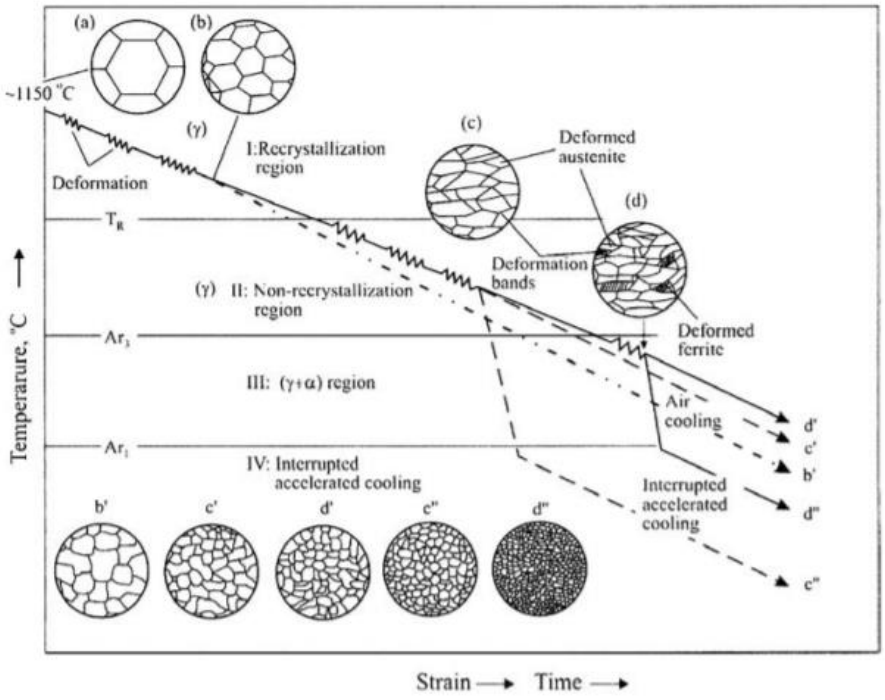


**Figure 2- 5. Schematic diagram of the influence of accelerated cooling on the microstructure of low-carbon micro-alloyed steel products during controlled rolling[12].**

## 2.2 Microstructure of HSLA steel

The mechanical properties of steels (such as strength, toughness, ductility, hardness, etc.) are also strongly influenced by the microstructure, which is largely determined by alloy composition and cooling rate. The microstructural constituents are indicated by the grain size, fraction of matrix (e.g., polygonal ferrite, acicular ferrite, bainitic ferrite, pearlite, bainite, martensite, etc.), size, shape, and volume fraction of precipitates and dislocation density. The main microstructure in the HSLA steel will be introduced in this chapter. **Table 2-4Table 2- 1** and **Figure 2-6** show the microstructures obtained in line pipe HSLA using different processing conditions.

**Table 2-4. Microstructures obtained using different processing conditions(TMCP：thermo-mechanical controlled processing, AcC: accelerated cooling process, HOP: online heat-treatment process)[25]**

| API 5L | Processing | Microstructure |
|---|---|---|
| X70 | TMCP | Polygonal Ferrite (PF) + Pearlite Band (P) |
| | | Bainite (B) |
| | TMCP + QT | Bainite (B) + Martensite (M) + Ferrite (F)* |
| | TMCP + AcC +QT | Fine-grained Bainite |
| X80 | TMCP + AcC | Lower Bainite (LB) |
| | | Ferrite (F) + Bainite (B) Dual Phase (DP)* |
| | | Lower Bainite (B) + Lath Martensite (M) |
| | TMCP + AcC + HOP | Bainite (B) + Martensite-austenite (MA)* |
| X100 | TMCP | Ferrite (F) + Bainite (B) |
| | TMCP + AcC + HOP | Ferrite (F) + Bainite (B) Dual Phase (DP)* |
| X120 | TMCP + AcC | Lower Bainite (LB) |
| | | Ferrite (F) + Martensite (M) Dual Phase (DP)* |
| | | Tempered Lath Martensite (TLM)* |

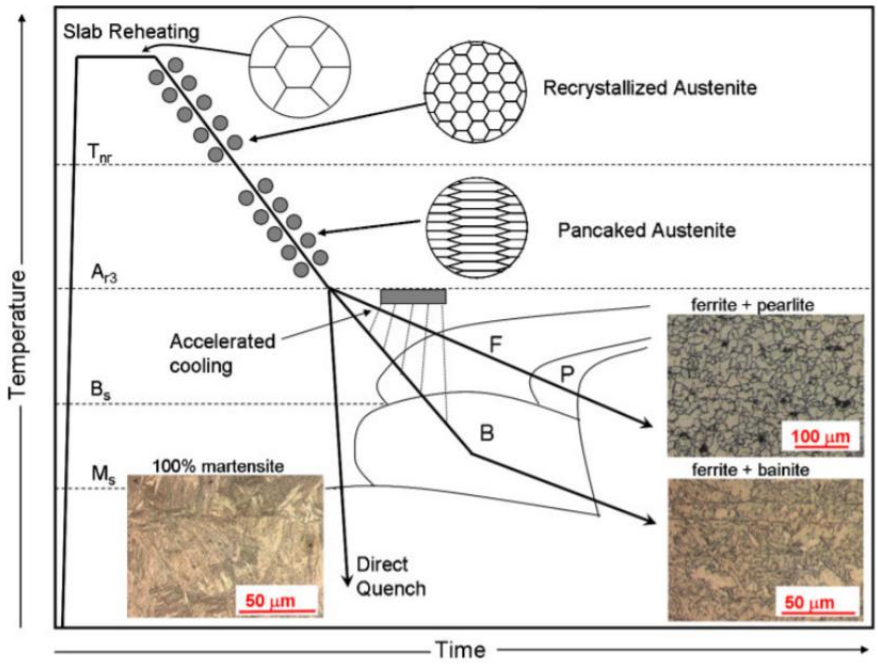


**Figure 2-6. Schematic diagram of thermomechanical processing (TMP) and microstructures that result from this process[5].**

### 2.2.1 Matrix

As shown in **Figure 2-7**, the transformation from γ to α can result in the formation of a variety of products. There are three main ferritic constituents that form in metals: allotriomorphic ferrite(or polygonal ferrite), Widmanstatten side plates, and acicular ferrite[26].

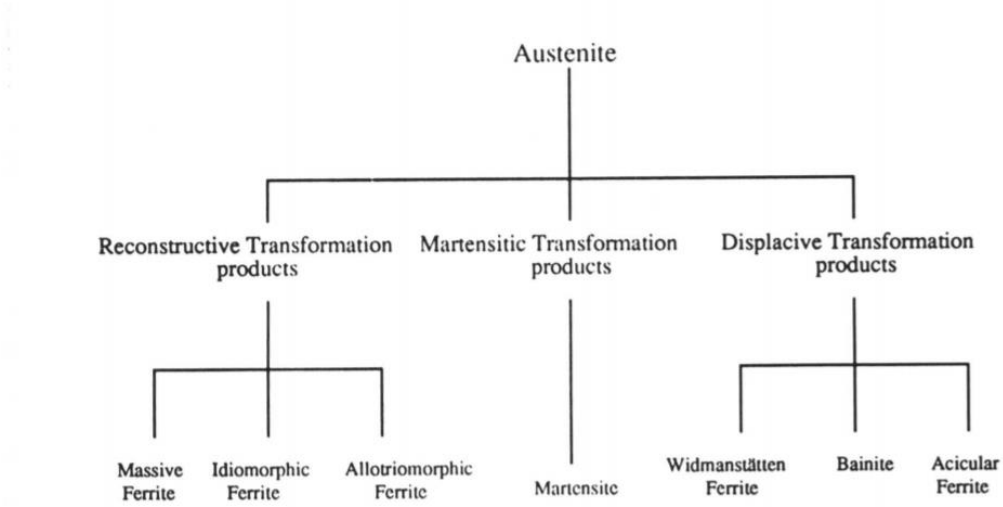


**Figure 2-7. Classification of transformation products formed during γ to α transformation according to the nucleation and growth mechanisms[27].**

### *2.2.1.1 Allotriomorphic ferrite*

Ferrites can be classified into allotriomorphic ferrite and idiomorphic ferrite by reconstructive transformation mechanism. as shown in **Figure 2-8**[26, 28, 29]. Idiomorph ferrite, which nucleates somewhere within the grain, has a crystallographically facetted shape. By contrast, allotriomorph ferrite grows more rapidly along the austenite grain surface and thus its contours do not reflect its internal crystalline symmetry. It has a semi-coherent interface with the other adjacent grain during the growth stage, which can be treated in terms of the normal migration of planar γ/α interfaces.

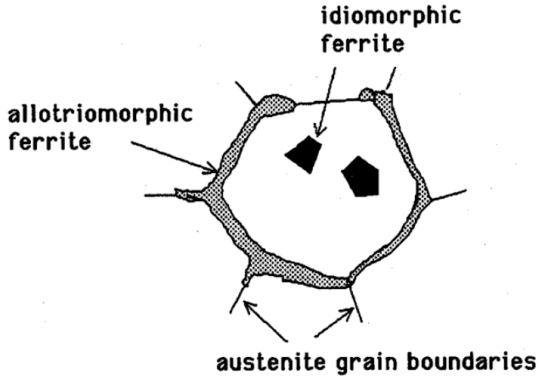


**Figure 2-8. Schematic of allotriomorphic ferrite and idiomorph ferrite[30].**

Allotriomorphic ferrite (α) is the first phase to form on cooling below the Ae3 temperature with low cooling rates. Thus, a high-volume fraction of allotriomorphic ferrite would limit the amount of austenite left for the formation of other decomposition products. It was reported that a large width of allotriomorphic ferrite offers little resistance to cleavage crack propagation at low temperatures, it is bad for weld metal toughness[29].

#### *2.2.1.2 Widmanstatten Ferrite*

Widmanstatten ferrite is another phase formed by the transformation of γ below Ae3, as shown in **Figure 2-9**. Widmanstatten ferrite grows by a displacive mechanism and consequently has higher stored energy, which is different from allotriomorphic ferrite. It is reported that the transformation start temperature for Widmanstatten ferrite is known to increase with austenite grain size.

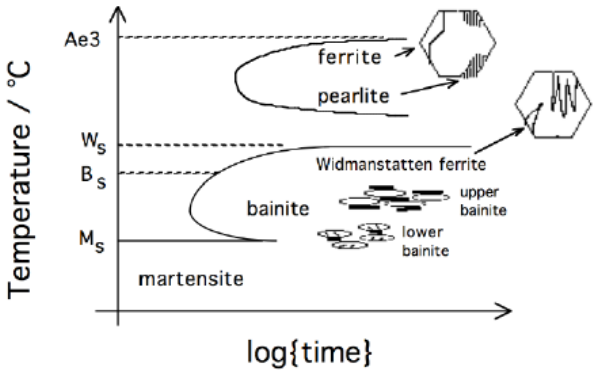


**Figure 2-9. Widmanstatten ferrite on the TTT diagram[30].**

The long plate characteristic of Widmanstatten ferrite is usually a prominent feature of low-carbon steel. This structure is an extension of the self-crystalline side plate of grain boundary ferrite, in which the ferrite follows the K-S orientation of austenite grain. Widmanstatten ferrite has the shape of a thin wedge on an optical scale. It can be divided into primary Widmanstatten ferrite (Widmanstatten ferrite primary side plates) and secondary Widmanstatten ferrite (nucleate from previously formed grain boundary allotriomorphic ferrite) according to nucleation sites, as shown in **Figure 2-10**.

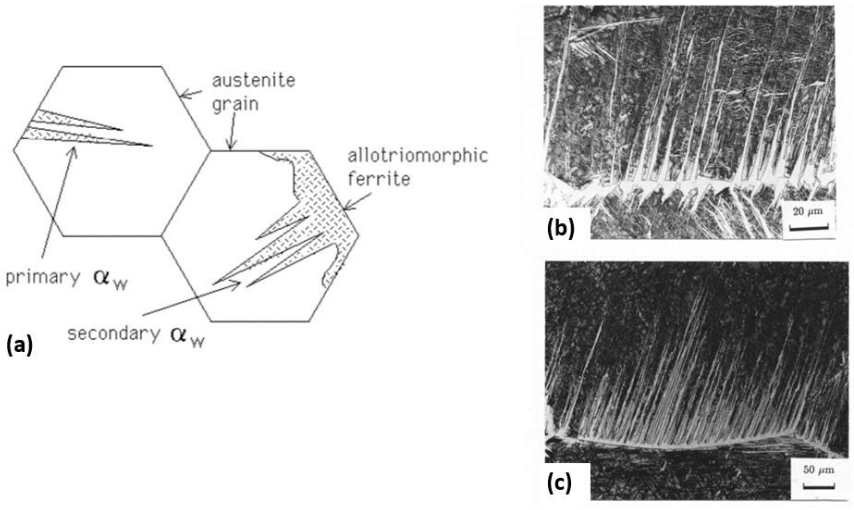

**Figure 2-10. (a) Morphology of primary and secondary Widmanstatten ferrite; (b) Primary Widmanstatten ferrite. (c) Secondary Widmanstatten ferrite[30].**

Research on the Widmanstatten ferrite shows that it could be bad for toughness and it could also benefit both toughness and strength. Some have shown that Widmanstatten ferrite can arrest cracks, which might be expected since large fractions of Widmanstatten ferrite are usually associated with refined microstructures[28].

### *2.2.1.3 Bainite//Acicular ferrite microstructure*

Bainite or acicular ferrite can be obtained under identical isothermal transformation conditions in the same (inclusion-rich) steel. Bainite is formed when the austenite grain size is small enough for nucleation on the grain surface to predominate (subsequent growth will overwhelm the grain interior). When the grain size of γ is large, intragranular nucleation on inclusions dominates, so acicular ferrite can be obtained, as shown in **Figure 2-11**[29].

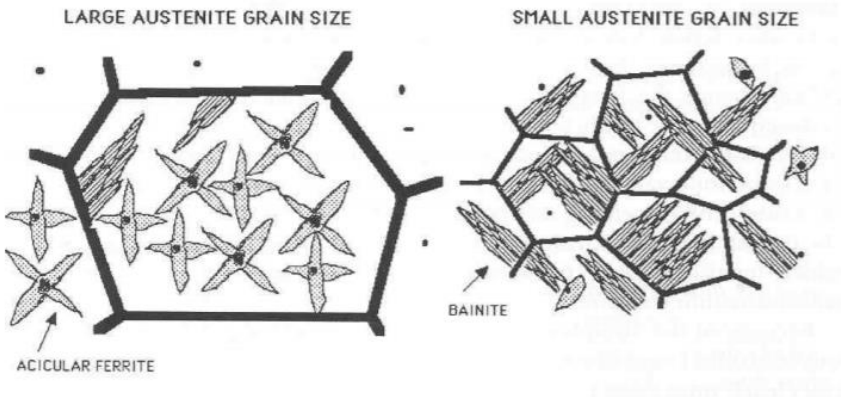


**Figure 2-11. Schematic of the effect of austenite grain size in determining whether the microstructure is predominantly acicular ferrite or bainite[29].**

Any factor that increases the number density or potency of intragranular nucleation sites at the cost of γ grain boundary sites favors a transition from a bainitic to an acicular ferrite microstructure. There are many ways to achieve the transformation, for example: increasing the size of γ grains, inactive layers of allotriomorphic ferrite, decorating thin grain boundaries, adding inclusion content, or rendering the boundaries impotent [29]. It is reported that acicular ferrite is essentially identical to bainite. They have similar transformation mechanisms (the incomplete reaction phenomenon, an invariant-plane strain shape deformation accompanying growth, a large dislocation density, etc.), but their microstructures might differ in detail. Acicular ferrite nucleate intragranular at point sites so that parallel formations of plates cannot develop, whereas bainite grows as a series of parallel platelets emanating from γ grain surfaces[29]. In this section, we will give a brief introduction to acicular ferrite.

(1) General Characteristics and Morphology

"Acicular ferrite" αa is a phase most commonly observed as austenite transforms during the cooling (occurs at below Bainite start temperature) of low–alloy steel. It is called acicular due to its needle shape in 2D sections. These turn out to be, lenticular plates (typically about 10μm long, 1 μm wide, with an aspect ratio smaller than 0.1) in 3D. The morphology of Acicular ferrite is shown in **Figure 2-12**.

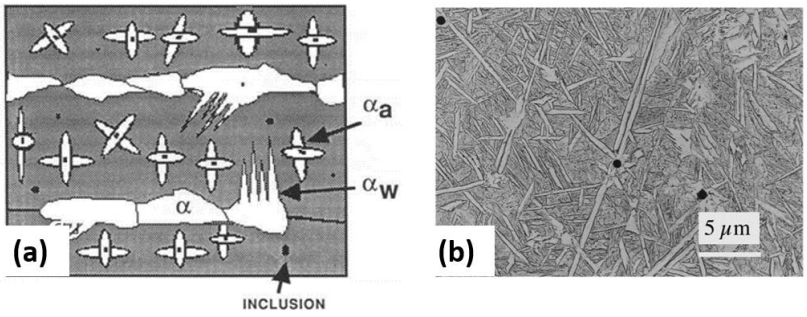


**Figure 2-12. (a) Schematic of acicular ferrite and Widmanstatten Ferrite ;(b) Replica transmission electron micrograph of acicular ferrite plates in a steel weld deposit[29].**

(2) Formation

As shown in **Figure 2-12**(a), inclusions (oxides or other compounds) in the austenite grains stimulate the nucleation of acicular ferrite. Acicular ferrites nucleate on inclusions during the early stages of transformation and then form autocatalytically. Alloying elements (like Nb, Ti, V, Mo) in the material can help the formation of acicular ferrite. The growth of acicular ferrite is displacive and is accompanied by an invariant–plane strain shape deformation. The size, thickness, and amount of the acicular ferrite plates will be influenced by the transformation temperature, cooling rate, and austenite size.

(3) Mechanical properties-Toughening

Acicular ferrite has chaotic ordering (Lack of order) which increases the toughness of the material. The high-angle grain boundary of acicular ferrite will change the direction of the cleavage crack, thus it gives a superior toughness. The good combination of toughness and

strength provided by acicular ferrite makes it to be a desirable microstructure for pipe steel to meet low-cost requirements [29].

#### *2.2.1.4 Martensite/ Austenite (M/A)*

In continuously cooled low-carbon and micro-alloyed steels, austenite is locally enriched with carbon during the transformation and is thereby stabilized during the decomposition of austenite into ferrite and/or bainite. Hence, some of the parent austenite may be retained at room temperature or partially transform to martensite/ austenite below the martensite start temperature. Four different morphologies of M/A particles are reported by Li and Baker [31]: M/A islands(sizes 0.5 ~ 5 μm), connected particles along prior austenite grain boundaries, M/A-C particles consisting of M/A and a second phase(carbide and ferrite) and elongated stringer particles(length <10 μm, width 0.2 ~ 2 μm) along with bainitic ferrite laths.

### 2.2.2 Precipitates

As mentioned above, precipitation hardening is a significant method to improve the strength of steel. The Ashby-Orowan equation indicates that the smaller the spacing between particles (L), the higher the strengthening amount. It is also reported that nano-scale precipitation and cluster-strengthened steels show excellent mechanical properties. So to obtain the largest amount of strengthening, a high volume fraction of nanoscale precipitates should be achieved[25].

### *2.2.2.1 Types of precipitates*

According to the misfit between the second phase and the matrix, precipitates can be classified as coherent, semi-coherent, and incoherent precipitates. They can also be classified into deformable phase and non-deformable phase categories according to the mechanism of dislocation movement across the precipitation. Here we will describe the precipitation in HSLA steel according to the matrix: a) precipitation in austenite; b) Precipitation in ferrite.

#### ***2.2.2.1.1 Precipitation in Austenite-strain induced precipitation (SIP)***

Precipitates formed in austenite are mostly due to a supersaturated austenite solid solution as the solubility of micro-alloy carbide/nitride reduces as temperature decreases. Homogenous nucleation is not possible due to the large misfit between the matrix and precipitate. Instead, precipitation often occurs through a strain-induced precipitation mechanism. Precipitates that nucleate on dislocations are referred to as strain-induced precipitation(SIP), which usually form as carbide/nitride {MX (M = Al, Nb, Ti, V; X = C, N)} or carbonitride { $MCx\ N1-x$ ($x$ is the mole fraction of C in the interstitial sublattice}. A common example is the SIP of Nb(C, N) and TiN, which are employed in controlled rolling to suppress recrystallization in order to obtain “pancaked” austenite.

(1) mechanism

SIP precipitates heterogeneously because of the large lattice misfit (~15% for VN, ~25% for NbC) between the matrix and precipitates. The misfit can be largely accommodated when they form on dislocations. This is the reason why the precipitates prefer to nucleate

on the dislocation network during the hot deformation of micro-alloyed steels. SIP is semi-coherent having the Cube-on-Cube OR with the austenitic matrix.

When hot deformation is applied in the austenite region, the introduction of dislocations (in the form of dislocation tangles, cell structure, or microbands), dislocation nodes are created and provide nucleation sites for the precipitation of carbides/nitrides. As mentioned in section 2.1.3, it is necessary to consider mechanisms that will impede dislocation movement, ie. will require higher stresses to activate the movement of dislocations, to strengthen the steel. Dislocation strengthening is also one of the important strengthening methods in HSLA steel. Dislocation density and morphology will influence both the tensile strength and yield strength of the material. So it is also important to understand the dislocation configuration in steels[12].

(2) Strengthening effect

Strain-induced precipitation (SIP) is very important to grain refinement and strain accumulation in the roughing and finishing stages of micro-alloyed steels during TMP.

***2.2.2.1.2 Precipitation in Ferrite***

Because of their small size (2-5 nm in diameter), the particles which precipitate during or after the phase are one of the most effective at precipitate strengthening. As shown in **Figure 2-13**, there are 2 types of precipitates in ferrite: interphase precipitation (during the decomposition of the Austenite) and matrix precipitation (from supersaturated Ferrite).

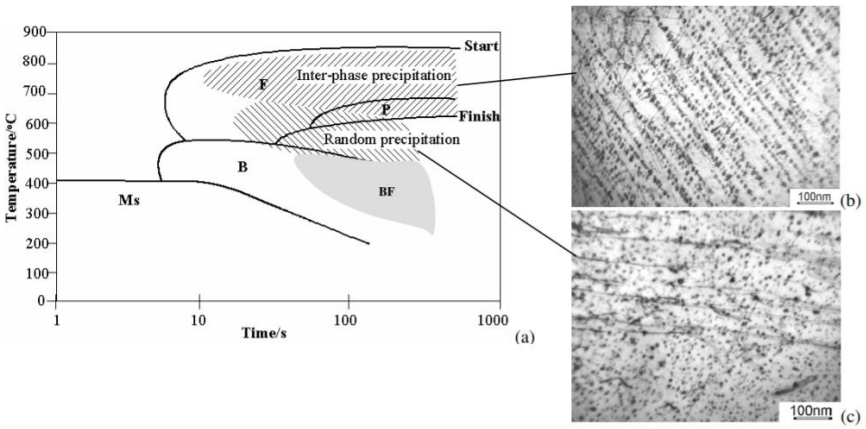


**Figure 2-13. CCT diagram for micro-alloyed steel indicating approximate regions of interphase and random precipitation[32].**

### 2.2.2.1.2.1 interphase precipitation

Interphase precipitation which is a non-random dispersion of precipitates aligned in rows takes place during γ/α transformation[12, 25, 33].

(1) Morphologies and orientation

Interphase precipitation has various morphologies, such as planar interphase precipitation(**Figure 2-14**a), curved interphase precipitation(**Figure 2-14**c,d), and fibrous interphase precipitation(**Figure 2-14**d) as shown in **Figure 2-14**. The characteristic morphologies of interphase precipitation are closely related to the thermomechanical processing conditions of the steel, and dependent on the transformation thermodynamics and kinetics[25].

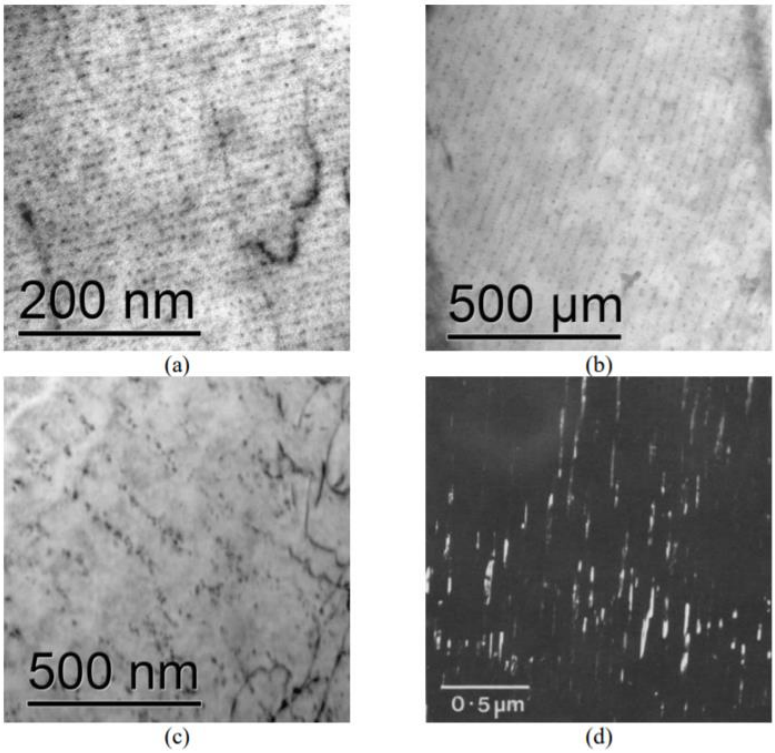


**Figure 2-14. TEM images of thin foil specimens showing (a) planar interphase precipitation, (b) curved interphase precipitation with uniform sheet spacing, (c) curved interphase precipitation with random sheet spacing, and (d) fibrous interphase precipitation(dark field)[34, 35].**

It is reported in many papers that the Kurdjumov-Sachs (K-S) relationship is adapted between interphase precipitates and the ferrite matrix, which is,

$$(111)\ MC//(110)\alpha$$

$$[110]MC//\ [111]\ \alpha$$

where MC means micro-alloy carbides.

In order to minimize the nucleation-free energy, interphase precipitates also formed in a unique variant of the Baker-Nutting (B-N) orientation relationship with the ferrite matrix. B-N relationship is:

(001) MC// (001) α

[110]MC// [010] α

(2) Mechanism

Several mechanisms of interphase precipitation have been proposed to explain interphase precipitation: a) the planar and curved ledge mechanism; b) the structural ledges mechanism and super ledge mechanism; c) the bowing mechanism; d) the ledge mechanism. The commonly adopted one was the "ledge mechanism", by Davenport and Honeycombe[36].

(3) Strengthening Effect

Interphase precipitation provides a good combination of toughness and strength for hot-rolled steels with a low carbon concentration. V micro-alloy steels have a larger solubility and can dissolve large amounts of V-carbonitride at relatively moderate temperatures, making them particularly suitable for producing interphase precipitation. While in Ti and Nb steels, the tendency for inter-phase precipitation is increased with transformation temperature.

#### 2.2.2.1.2.2 matrix precipitation

Precipitation from supersaturated ferrite occurs following the austenite-to-ferrite transformation and is commonly known as matrix precipitation. The process can occur after rapid cooling to the low-temperature phase region (from about 700 ºC and below) either during coiling or upon reheating during a sub-critical annealing or normalizing treatment[21, 37]. It is worth mentioning that matrix precipitation in ferrite could be heterogeneous and homogeneous.

(1) Morphologies and orientation

The interface will gain speed relative to the rate of precipitation on lowering the temperature, thus precipitations occur behind the migrating γ/α-boundary. So these particles are randomly distributed instead of aligning in rows, but they also follow different variants of the B-N (N-W is also reported) orientation relationship to reduce the interfacial energy [15].

(2) Strengthening effect

Significant strengthening can also be obtained from matrix precipitation. As reported in Y.F. Shen's publication [38], matrix precipitates with an average diameter of 10 nm contribute about 450 MPa to the yield strength of a 0.04C HSLA steel, having 0.08Ti, 0.18Mo, 0.011Nb, and 0.015V (wt%).

#### *2.2.2.2 Clusters*

Solute-rich groupings of atoms without ordered arrangement are defined as clusters, which are different from precipitates and are characterized by a crystal structure distinct from the matrix. The study in CASTRIP steel with 0.084 wt.% Nb shows that Nb-rich solute clusters are powerful strengthening agents[39]. And it has been reported in Al–Cu alloys, solute clusters appear to be very similar to Guinier–Preston (GP) zones and occur as fully coherent plates, or discs that are one atomic layer thick on the {0 0 1} plane of the a-ferrite matrix[39]. The morphology of the cluster is shown in **Figure 2-15**(a: regular shape-linear; b: unregular shape.)

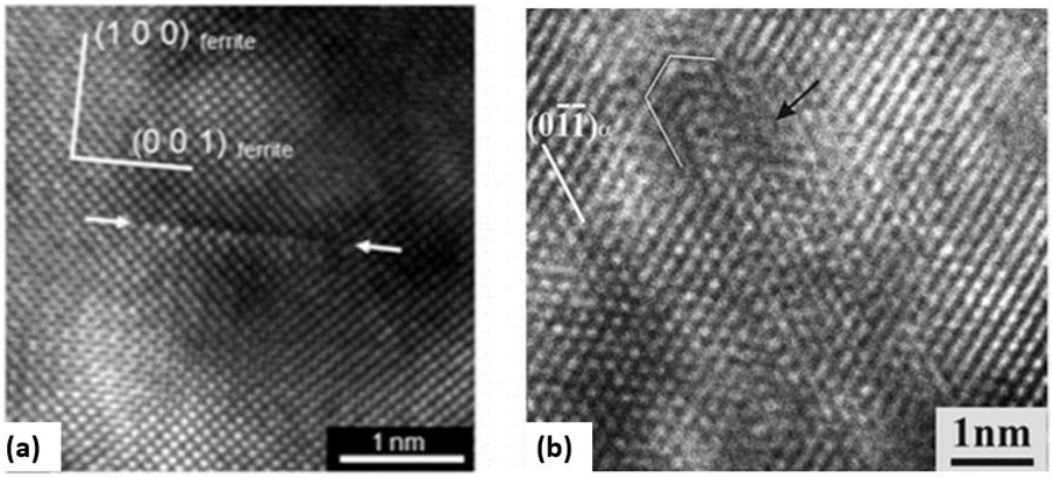


**Figure 2-15. (a) GP zone-like cluster ;( b)HRTEM of a cluster in the ferrite matrix[13, 39].**

The size and the number density of precipitates will influence the yield strength increment and the resultant ductility change. Both interphase precipitation and matrix precipitation can have a significant strengthening effect if their size and volume fraction are suitably controlled through thermomechanical processing[25, 40].

### *2.2.2.3 Solubility product-Ksp*

The reaction of a micro-alloying element [M] with an interstitial [X](wt%), both dissolved in the γ/α, generates a compound [MX] at a temperature T is given as:

$$[M] + [X] \leftrightarrow (MX) \qquad \text{(Equation 2- 6)}$$

$$ks = [M]\,[X]$$

Solubility product is defined by:

$$\lg ks = A - B/T$$

A, B: constants for a given system.

The solubility products (Ks) of the micro-alloy carbides and nitrides are compared in **Figure 2-16**. Many conclusions can be drawn from this data: a) in γ, nitrides are more stable than carbides. b) TiN is markedly more stable than other carbides and nitrides. c) VC is far more soluble than other carbides and nitrides, etc.[2, 24, 41].

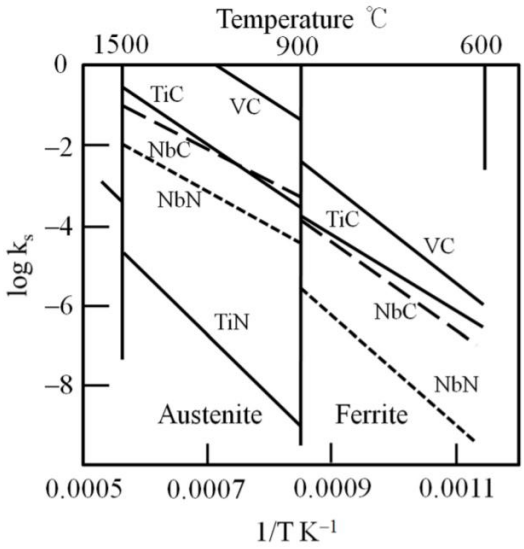


**Figure 2-16. Temperature dependence of the solubility products of VC, TiC, NbC, NbN, and TiN in γ and α, respectively[37].**

### *2.2.2.4 Precipitates kinetics*

In the classical precipitation model, there are two major stages: (i) nucleation and growth (ii) growth and coarsening. The nucleation rate depends on the chemical driving force and the dislocation density. The growth and coarsening processes are facilitated by the fast pipe diffusion due to the dislocation network, similar to that inside the grain boundary[24, 41].

#### *2.2.2.4.1 Nucleation and growth*

(1) Nucleation barrier and driving force.

The nucleation of a new phase is driven by a reduction in the Gibbs' free energy of the system. The most common theoretical model describing the nucleation process is the classical nucleation theory (CNT). In CNT, a spontaneously formed embryotic nucleus must overcome a nucleation barrier (a maximum in the Gibbs' free energy change due to the formation of the nucleus) to be thermodynamically stable and grow, as shown in **Figure 2-17**.

The driving force for nucleation decreases Gibbs' free energy while the creation of an interface between the matrix and the precipitate increases Gibbs's free energy:

$$\Delta G = \frac{4\pi r^3}{3}\Delta G_m + 4\pi\sigma r^2 \qquad \text{(Equation 2- 7)}$$

with $r$ the radius of the nucleus, $\Delta Gm$ is the driving force for nucleation ($\Delta G_m \leq 0$, when nucleation is favorable) and $\sigma$ is the interfacial energy.

$\Delta G$ has a maximum value with respect to $r$ when $d\Delta G/\, dr = 0$. This maximum value, $\Delta G^*$, is the nucleation barrier. The nucleation barrier is given by:

$$\Delta G^* = \frac{16\pi\sigma^3}{3{\Delta G_m}^2} \qquad \text{(Equation 2- 8)}$$

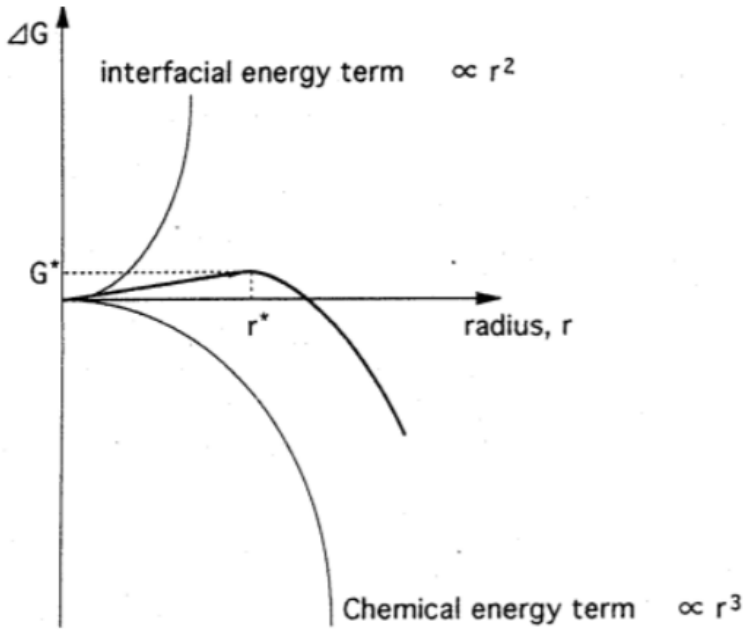


**Figure 2-17. The change in Gibbs free energy of a spherical nucleus with respect to its radius[42].**

(2) Nucleation rate

For hard particles, the Ashby-Orowan mechanism predicts that the only parameter that determines precipitation reinforcement is particle spacing. Therefore, to obtain the maximum possible strengthening, the nucleation rate that determines precipitation dispersion density should be maximized. According to the theory of nucleation, the relationship between nucleation rate ($\dot{N}$) and critical energy for nucleation ($\Delta G^*$) is described by the following equation[2]:

$$\dot{N} \propto exp^{\frac{-\Delta G^*}{kT}} \qquad \text{(Equation 2- 9)}$$

Where $T$ - temperature, $k$ - Boltzmann constant.

It can be concluded that when the critical energy of nucleation decreases, the rate of nucleation formation and the quantity density of precipitates can be increased exponentially. Reducing the interfacial and elastic strain energy, increasing the nucleation driving force; and increasing the sites for nucleation will help to reduce the nucleation energy barrier[40].

(3) Growth rate

According to Zurob's model [41], the growth rate of the nuclei is controlled by the diffusion of microalloying element M, shown as:

$$\frac{dr}{dt}|growth = \frac{D_{eff}}{r}\frac{C_M - C_M^r}{C_M^p - C_M^{eq}} + \frac{1}{N}\frac{dN}{dt}(\alpha r^* - r) \qquad \text{(Equation 2- 10)}$$

$$D_{eff} = D_{pipe}\pi R_{core}^2\rho + D_{bulk}(1 - \pi R_{core}^2\rho) \qquad \text{(Equation 2- 11)}$$

where $D$eff is the effective diffusion coefficient. $C_M{}^r$, $C_M{}^P$, and $C_M{}^{eq}$ denote the composition of M in equilibrium with a precipitate particle of radius $r$, the composition of M of the precipitate, and the composition of M in equilibrium with a planar precipitate, respectively. $D$eff is an average of the pipe diffusion coefficient $D_{\text{pipe}}$ and the bulk diffusion coefficient $D_{\text{bulk}}$ depending on the dislocation density $\rho$ and the cross-section area of the dislocation core $\pi R^2$.

***2.2.2.4.2 Growth and coarsening***

When a precipitate has nucleated, it may grow to reduce its surface-to-volume ratio, due to the Gibbs-Thomson effect. This is known as the growth and coarsening regimes of precipitation. Coarsening occurs because eliminating interfaces reduces the total energy

of the system. In fact, large particles grow faster than small particles during precipitation, large particles grow at the expense of small particles during classical coarsening. So the average particle size will increase with time. Ostwald ripening can be assumed to occur after precipitation " completion". The coarsening rate was given by Zurob as[24, 41]:

$$\frac{dr}{dt}|coarsen. = \frac{D_{eff}}{r}\frac{C_M - C_M^{27r/23}}{C_M^p - C_M^{eq}} \quad \text{(Equation 2- 12)}$$

$$\frac{dN}{dt}\left|coarsen = \frac{dr}{dt}\right| coarsen. \cdot \left[\frac{r^* C_M}{r(C_M^p - C_M)}\left(\frac{3}{4\pi r^3} - 2N + \frac{4\pi r^3 N^2}{3}\right) - 3N\right] \quad \text{(Equation 2- 13)}$$

where $C_M{}^{27r/23}$ is the solute M concentration of the matrix in equilibrium with a precipitate of radius 27r/23.

When the decrease of precipitate density by coarsening is greater than the increase of the precipitates density by nucleation, it means nucleation and growth stage transfers to the growth and coarsening stage[24, 41], i.e.

$$-\frac{dN}{dt}|growth + coarsening > \frac{dN}{dt}|nucleation \quad \text{(Equation 2- 14)}$$

The average rate of changes in particle size and number density of nuclei under conditions of simultaneous growth and coarsening are given below:

$$\frac{dr}{dt} = (1 - f_{coarse})\frac{dr}{dt}|growth + f_{coarse}\frac{dr}{dt}|coarsening \quad \text{(Equation 2- 15)}$$

$$\frac{dN}{dt} = f_{coarse}\frac{dN}{dt}|coarsening \qquad (\frac{dN}{dt}|growth = 0) \quad \text{(Equation 2- 16)}$$

$$f_{coarse} = 1 - \mathrm{erf}\left(4\left(\frac{r}{r^*} - 1\right)\right) \quad \text{(Equation 2- 17)}$$

***2.2.2.4.3 Precipitation–time–temperature (PTT) diagrams***

The kinetics of precipitation can also be expressed in precipitation—time—temperature (PTT) diagrams. PTT diagrams for micro-alloyed steels have been determined by other authors using theoretical equations, transmission microscopy, or the stress relaxation method[43, 44]. **Figure 2- 18** shows the PTT diagram for Nb, Ti, and V steel, it is seen that the minimum incubation time, which corresponds to the nose of the curve, depends on the strain[44].

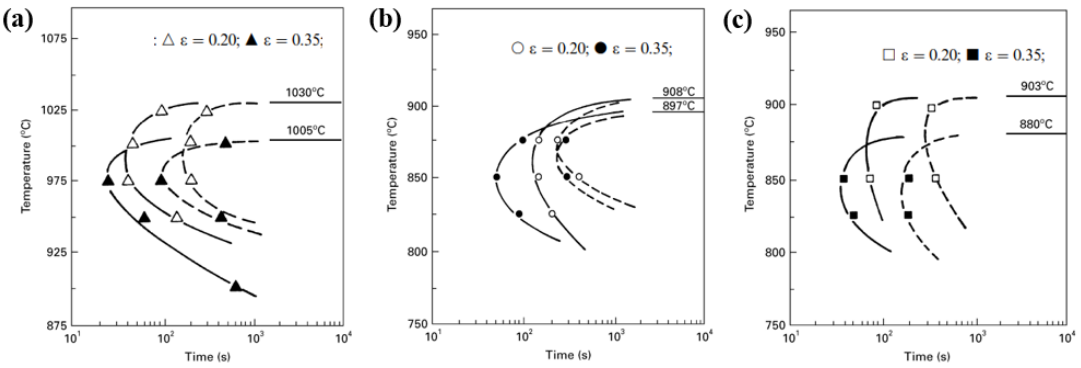


**Figure 2- 18. PTT diagrams for the strain-induced precipitates in (a)Nb, (b)Ti, and (c)V steel. (Solid line-start time of SIP, dash line-finish times of SIP)[44]**

## 2.3 Critical Reflection on the Literature:

The contribution to the strengthening of HSLA due to the formation of precipitates and the evolution of the matrix in the HSLA steel has been studied by several groups. However, there are still some unanswered questions in the literature:

### 2.3.1 Quantitative analysis of precipitation

Most of the literature about the precipitates is still very qualitative. Quantitative analysis in mixed precipitates is not easy sometimes due to the difficulty in quantifying the light elements, like C and N. The characterization of clusters in HSLA steel is also difficult because of the limitation in conventional TEM. When multiple microalloying elements are present, it will be harder to tell whether they form a single population of mixed/complex carbonitrides, or do they form two populations of precipitates because of the limitation of the characterization technique. And without quantitative analysis of precipitation, we don't know the role of alloying element additions. For example, adding V and Mo seems to increase strength in some cases, but often we are not able to detect where the V and Mo are present and how they helped to increase strength. In that case, we can't make a very good design of the steel that efficiently uses the alloying element additions.

### 2.3.2 Site-specific analysis of the precipitates in HSLA steel

Extensive research has been conducted on the precipitates in microalloyed steels using TEM. However, most of the literature analyzes thin TEM foils prepared by electropolishing

or carbon extraction replicas from polished surfaces, which are not site-specific in most cases and hard for detailed investigation and discussion of precipitates in different regions within the microstructure[45-58]. This is particularly challenging given the complex microstructure of steels, which includes variations of dislocation density, grain size, and austenite decomposition products such as polygonal ferrite-PF, acicular ferrite-AF, granular bainite-GB, and bainitic ferrite-BF[59-61]. For instance, hot-rolled line pipe steels often contain PF, AF, and GB/BF, and conventional random sampling methods are inadequate for determining whether interphase precipitation has occurred during the formation of PF or the extent of micro-alloyed precipitation within PF, AF, and BF. A site-specific characterization method can provide insights into precipitation characteristics with respect to local microstructure features and the extent to which precipitates may have contributed to the development of the final microstructure due to partial recrystallization or interaction with subsequent phase transformations.

### 2.3.3 The role of cluster and transformation from cluster to precipitates.

It has been reported in an Nb-micro alloyed steel, Nb-rich solute atom clusters (average size ~ 60 atoms at peak hardness) are similar to GP zones in Al–Cu alloys[39]. Compared with conventional Nb (C, N) precipitation strengthening, these clusters are highly potent effective strengthening agents. However, the precise role of cluster and transformation from cluster to precipitation are not completely understood. And the potential for the strengthening of commercial steels by clustering or GP zones has not been widely explored[1].

### 2.3.4 Competition of strain-induced precipitates and (Ti, Nb)(C, N)

In controlled rolling of HSLA steel plate, the strain-induced precipitation of Nb (C, N) at finishing temperatures plays a crucial role in preventing the recrystallization of austenite, thereby promoting ferrite nucleation on cooling and enhancing grain elongation and accumulated strain [41, 54, 62, 63]. Research on the thermodynamics and kinetics of NbC strain-induced precipitation in austenite and its interaction with dislocations and austenite grain boundaries during TMP has been extensive[55-57, 64-66].

However, the absence of strain-induced precipitation of NbC is frequently observed in conventional Nb-Ti micro-alloyed steel[67-70]. Quantitative analysis through transmission electron microscopy and 3D atom probe tomography reveals that the epitaxial growth of NbC on pre-existing TiN particles suppresses strain-induced precipitation of NbC on dislocations [67, 68]. The nucleation of SIP in HSLA is influenced by several parameters. Ma's work [3] found that the inter-spacing of TiN particles is a critical parameter affecting the precipitation behavior of NbC during thermomechanical controlled processing. Additionally, the dislocation density plays a significant role in determining the acceleration degree in precipitation kinetics. The strain applied during TMP affects both the dislocation density and the nucleation rate of SIP. Although several models have been developed for the competition between TiN and NbC [67, 71, 72]the effect of strain on the precipitation behavior in Nb+Ti steel remains unclear and warrants further discussion.

## 2.4 Review of Advanced Characterization Techniques

Advanced characterization methods like High-temperature confocal laser scanning microscopy(HT-CLSM), STEM(EDS and EELS), high-resolution transmission electron microscopy (HR-TEM), in situ TEM, 4D-STEM and synchrotron X-ray, atom probe tomography (APT) could help answer the questions from 2.3[40].

### 2.4.1 High-temperature confocal laser scanning microscopy

High-temperature confocal laser scanning microscopy (HT-CLSM) is a powerful tool for in situ real-time studies of phase transformations during heat treatment.

#### *2.4.1.1 Introduction of HT-CLSM*

**Figure 2-19** shows the design of a modern HT-CLSM microscope. The working principle and details of the operation can be found in the literature[73]. HT-CLSM has an excellent depth (Z) resolution (~0.01 μm), which makes it possible to distinguish flat areas and even shallow grooves or dimples on the surface of the sample. The lateral resolution of CLSM is about 0.15 μm, which is limited by the wavelength of the laser[74].

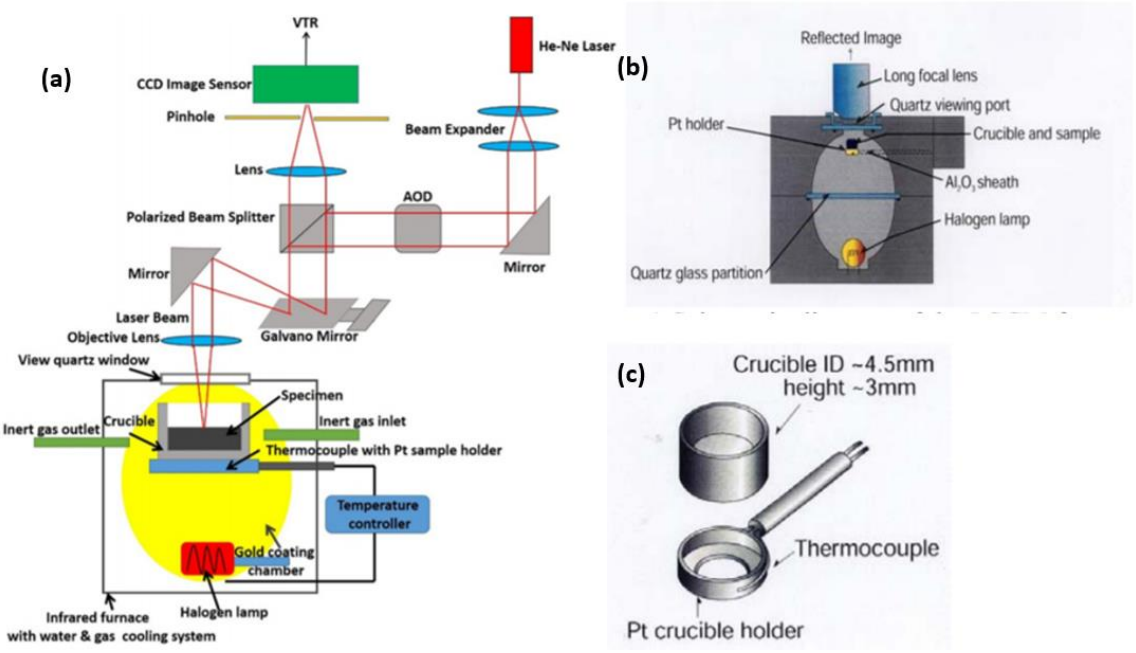


**Figure 2-19. (a) Schematic of HT-CLSM.(b)CLSM furnace;(c) sample holder[73, 74].**

### *2.4.1.2 Applications in steel*

CLSM has been used to study the high-temperature phase transformations (mainly in iron-based alloys) for a long time. The work-related to CLSM mainly focus on (i) ferrite fraction evolution, (ii)grain coarsening, (iii) onset and completion of phase transformations(start and finish temperatures or times), and (iv) intragranular acicular ferrite(IGF growth kinetics[75]. There is much research that analyzes the nucleation and growth of acicular ferrite in steel by CLSM. Wang, Xin, et al studied the relationship between the starting transformation temperature of acicular ferrite and decreasing cooling rate in Ti-Ca-Zr deoxidized low-carbon steel in CLSM [76]. And similar experiments were also conducted

in low-carbon steel (with 13 ppm Mg) by Lin, Chi-Kang, et al[77]. Beyond these, Clark, Samuel, et al also analyzes the Austenite/Ferrite Transformation Kinetics by CLSM[78].

#### *2.4.1.3 Opportunities and Challenges in HT-CLSM*

The unique advantages of HT-CLSM are its ability to observe surfaces in situ at temperatures up to 1800°C and its rapid heating and cooling rates (around 3000°C/min at high temperatures). However, at a lower temperature, the cooling rate decreases significantly, which is related to the study of solid-phase transformation of steel. For example, in many low alloy steels, it is impossible to study low-temperature phase transformations such as martensitic and bainite because of their low hardenability[75].

Today, the use of HT-CLSM in combination with other technologies (X-ray diffraction and fluorescence, time-resolved synchronous X-ray diffraction (TRXRD)) makes it possible to study chemistry and crystallography simultaneously.

### 2.4.2 EBSD

#### *2.4.2.1 introduction of EBSD*

Electron backscatter diffraction (EBSD) is an electron diffraction technique in scanning electron microscopy (SEM) used to obtain information about crystallographic phase, crystal orientation, as well as identify and map phase distributions on the surfaces of bulk polycrystals.

In the last ten years, the utilization of this technique has rapidly gained acceptance in metallurgical, materials, and geophysical laboratories. This can be attributed to the widespread availability of SEMs, the simplicity of sample preparation from bulk materials, the quickness of data acquisition, and the ability to obtain additional information about the microstructure on a submicron scale.

To obtain EBSD patterns a crystalline sample with a planar and artefact-free surface is placed in the scanning electron microscope and typically tilted to 70° as shown in **Figure 2-20**. An EBSD detector, consisting of a phosphor screen observed by a highly light-sensitive camera, is placed close to the sample. When a stationary electron beam is placed on a single crystalline area of the sample surface an EBSD pattern appears on the detector.

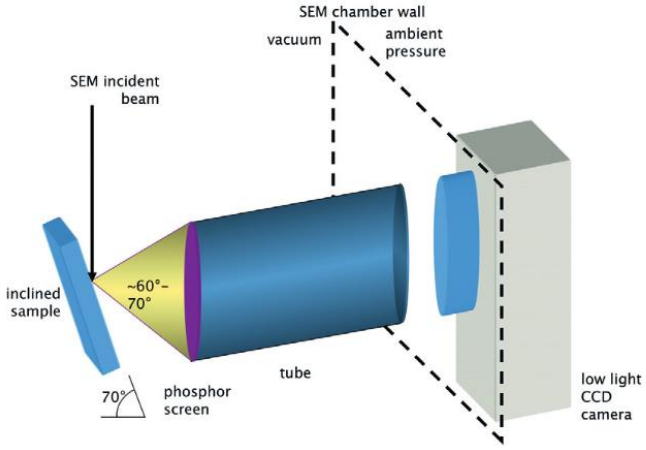


**Figure 2-20. Schematic diagram showing the experimental set-up for EBSD observations[79].**

#### *2.4.2.2 Generation and Interpretation of Electron Backscatter Diffraction Patterns*

An electron beam is targeted at a specific point on a tilted crystalline sample. When the beam hits the sample's surface, it is scattered incoherently and quasi-elastically in all directions by a point-like source within the crystal. The size of this incoherent scattering sets the spatial resolution of the method and is typically measured in the range of 10 nm.

The scattering creates a source of electrons that diverges near the sample's surface, and a few of these electrons strike atomic lattice planes at angles that fulfill the Bragg equation.

$$n\lambda = 2dsin\theta \qquad \text{(Equation 2- 18)}$$

where n is an integer, λ is the wavelength of the electrons, d is the spacing of the diffracting plane and θ the angle of incidence of the electrons on the diffracting plane.

The electrons are diffracted, creating pairs of large-angle cones that correspond to every diffracting plane, such as the green and blue cones in **Figure 2- 21**, which correspond to a single (110) lattice plane (red disc). A phosphor screen is frequently used to convert electrons to light, and the image produced on the EBSD detector contains distinctive Kikuchi bands formed at the intersection of areas with increased electron intensity on the screen. The EBSD detector image is a gnomonic projection of the diffracted cone, resulting in hyperbolic band edges.

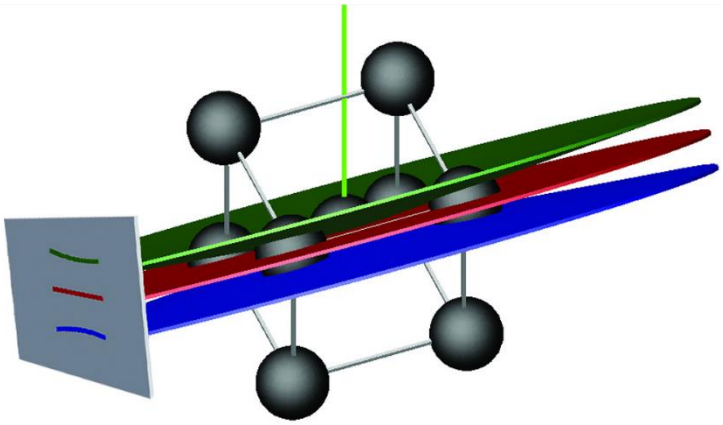

**Figure 2- 21.The formation of a Kikuchi band in an electron-backscattered diffraction pattern (EBSP)[80].**

A typical EBSD pattern is presented in **Figure 2- 22**. The pattern consists of straight, bright bands known as Kikuchi bands, which are directly related to the lattice planes of the diffracting crystal. The centerline of each band corresponds directly to the gnomonic projection of the lattice planes, and the width of the Kikuchi band is approximately proportional to the Bragg angle of electron diffraction on the related lattice plane. The band intensity profile is equivalent to the dynamic electron diffraction intensity achieved in a rocking experiment across the related lattice plane. The crystallographic phase and orientation can be determined from the geometry of the Kikuchi bands in the pattern. Information on local defect densities, especially on dislocation densities, can be obtained in a highly automated manner through computer software, which then displays the results of EBSD-based orientation microscopy.

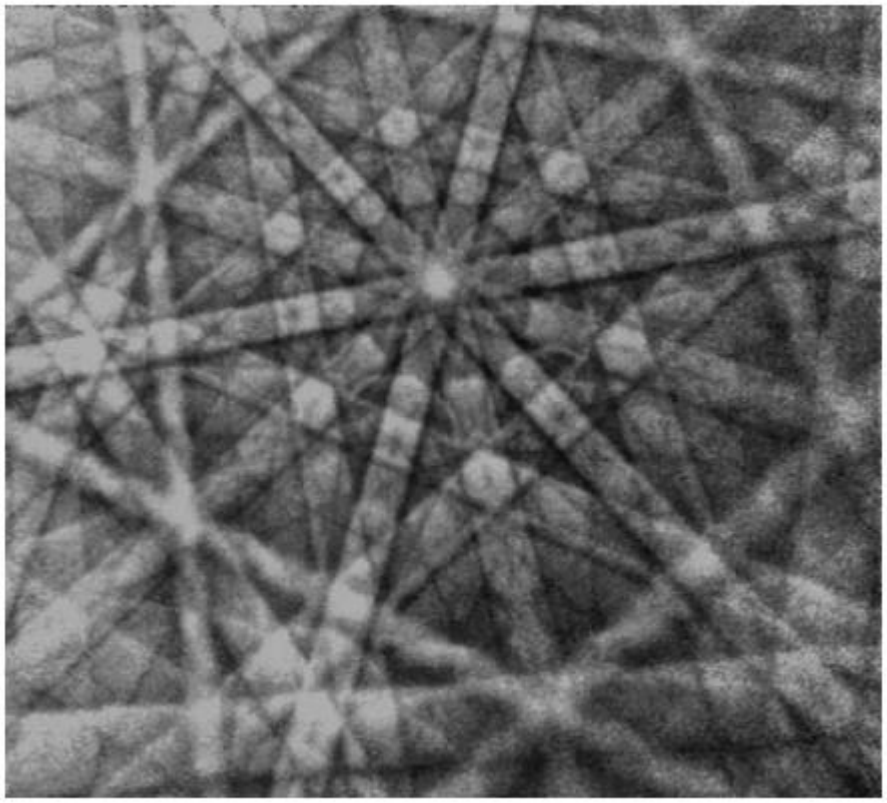

**Figure 2- 22. Backscatter Kikuchi pattern from cadmium at 20 keV, acquired with an analog video camera[80].**

In order to determine the crystal orientation and index patterns, a process is followed where camera images are transferred to a computer, as shown in **Figure 2- 23**. To achieve this, the Hough transform algorithm is utilized to convert the almost linear bands from lines to points, which are easier to locate. By leveraging information about the experimental geometry, the peak positions can be transformed into a chart of interplanar angles and compared with expected angles for the phases present in the sample, using look-up tables. Modern pattern capture and indexing systems can perform this task very quickly, with hundreds of patterns being analyzed per second. When coupled with accurate scanning of

the electron beam, a detailed mapping of the sample's crystallography can be generated, including crystal type, crystal orientation, and pattern quality. These maps provide valuable measurements of the sample's microstructure.

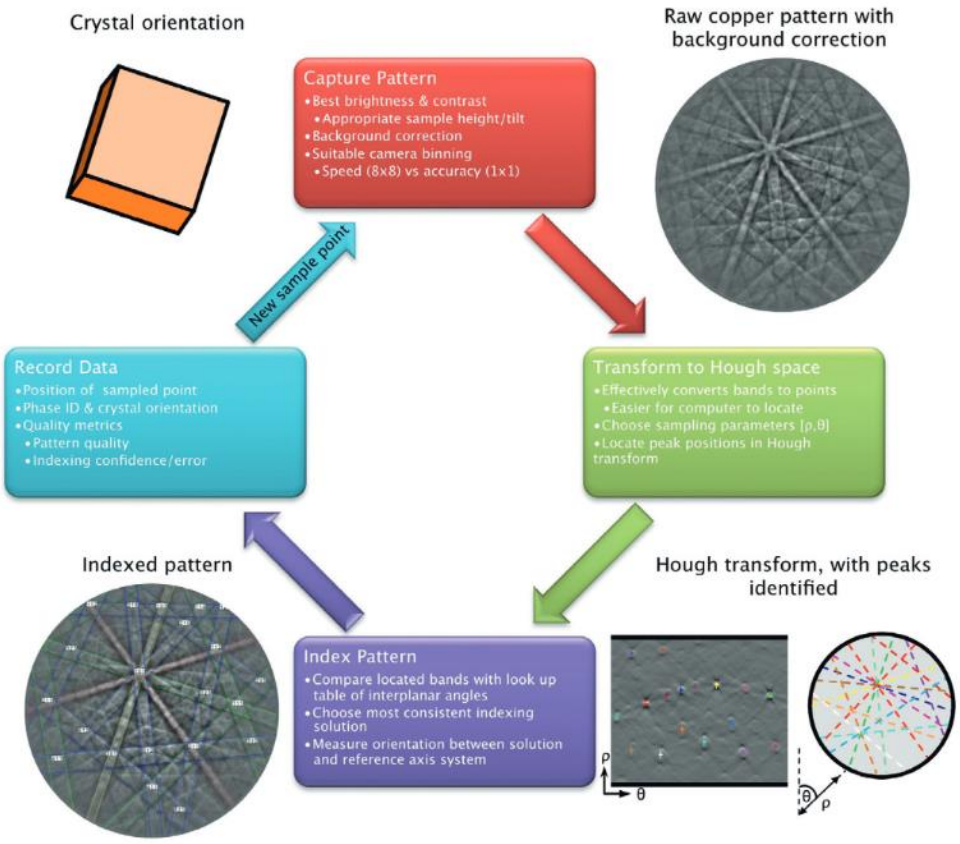


**Figure 2- 23. Overview of EBSD indexing procedure showing pattern capture through to determination of crystal orientation[79].**

### *2.4.2.3 Application areas*

EBSD has become a versatile tool for characterizing various aspects of materials. But the biggest area of EBSD application is in materials science and, more specifically, in the study

of metals and alloys. It can be used to identify different types of grain boundaries, characterize texture and its evolution during the deformation and annealing of metal alloys, examine the connection between grain size and texture components during deformation and annealing, etc. The main application of EBSD in this project is to obtain a kernel average misorientation (KAM) map. The KAM map is constructed based on the average misorientation angle of a given point with respect to all of its neighbors [81, 82] in EBSD. It can be used to estimate the density of geometrically necessary dislocations (GND) and assess the local transformation strain developed in the steel. GND is the geometrically necessary dislocations that represent an extra storage of dislocations required to accommodate the lattice curvature that arises whenever there is a non-uniform plastic deformation[83]. It is reported that low-temperature transformation microstructures such as acicular ferrite(AF), and bainitic ferrite(BF) contain a higher density of GNDs compared to reconstructive transformation products such as polygonal ferrite (PF)[81]. Thus, the low KAM areas could be identified as PF that formed at high temperatures (~700 ºC), while the high KAM areas are BF that formed at lower temperatures during cooling or isothermal holding [59, 60, 84].

### 2.4.3 Analytical TEM

Transmission electron microscopy (TEM) is a powerful microscopy technique in which a beam of electrons is transmitted through a specimen to form an image (bright field and dark field image) and diffraction pattern (selected area electron diffraction, nano-beam diffraction, and convergent beam electron diffraction). TEM is usually used to examine the

structure(like dislocation and precipitates), orientation (DP), composition(EDS/ EELS), and chemical/electronic properties of specimens(EELS) in submicron detail[85].

TEM has a significant impact on the analysis of precipitation in steel. In nearly all cases, TEM samples are best when very thin (usually <100nm for imaging, 10nm maximum for interpretable HRTEM image, 100 - 500 Å for good EELS). Twinjet electropolishing, Carbon replica, and FIB are the main sample preparation methods for precipitation analysis in TEM.

#### *2.4.2.1 Electron diffraction mode*

Selected area electron diffraction (SAED), nano-beam diffraction (NBD), and convergent beam electron diffraction (CBED) are all electron diffraction techniques.

***Selected Area Electron Diffraction（SAED）***

Parallel beams (plane waves traveling in one direction) interact with the sample in SAED. In diffraction mode, we will remove the objective aperture and insert the SAD aperture for selected area electron diffraction (SAED), it is in the plane of the first intermediate image that defines the region of which the diffraction is obtained.

SAED is usually used for phase identification, determination of lattice parameters, atomic positions, symmetry, determination of growth directions, etc.

***Convergent Beam Electron Diffraction (CBED)***

CBED uses a focused nanometer-sized probe which gives rise to diffraction patterns with discs, which contain information from higher-order Laue zones (HOLZ). The limitation of analyzing SAED for analyzing only areas around 500 nm in size with small areas is overcome by using a convergence beam. In CBED, however, the area studied is limited by beam size and beam interaction volume (~10 nm). CBED can be used to analyze specimen thickness, unit-cell parameters (accuracy of approx. 0.01%), crystal system, and 3D crystal symmetry (point group and space group). The difference between SAED and CBED patterns is shown in **Figure 2-24**.

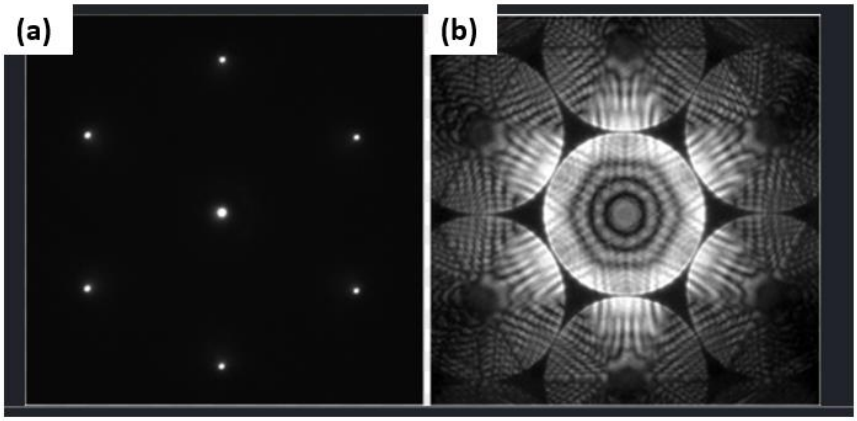


**Figure 2-24. SAED pattern; (b) CBED pattern[85]**

***Nano beam diffraction（NBD）***

Compared to the parallel beam in SAED, NBD uses a slightly convergent beam (diameter around 15-25 nm) with a convergence angle of in the order of 1.5–3.5 mrad, which makes the diffraction point disc-like. NBD can be used to measure the strain from the separations of the diffraction spots[85].

Conventional TEM is good for the analysis of the composition and crystal structure of large precipitates, and carbon replicas are better for the observation of precipitation.

#### *2.4.2.2 STEM*

STEM is similar to TEM. While STEM uses a focused beam instead of parallel electron beams. The focused beam in STEM scanned over the sample in a raster. When the transmitted signal is rasterized on the sample, it is collected as a function of the beam position. The detectors in STEM imaging include Bright-field (BF), Annular dark-field (ADF), and High-angle annular dark-field (HAADF) detectors.

***EDX and EELS***

The rastering of the beam on the sample makes STEM suitable for techniques such as Z-contrast ADF imaging and energy dispersive X-ray (EDX) spectroscopy or electron energy loss spectroscopy (EELS). Atomic-scale element maps can be obtained by using EDX or EELS in the STEM. EELS is best for low atomic number (Z) elements, EDS is best for high atomic number elements.

***High-angle annular dark-field imaging (HAADF-STEM)***

Annular dark-field imaging-STEM is a powerful tool to map local atomic structures and it has been successfully applied to the imaging of various material interfaces.

***HRTEM***

Since traditional TEM imaging is often difficult to reveal ultrafine precipitates, more complex imaging techniques, such as high-resolution transmission electron microscopy (HRTEM), are often used to study nanoscale precipitates.

HRTEM is an imaging mode of TEM that is phase-contrast imaging, in which transmitted electrons and scattered electrons combine to produce an image. In order to take advantage of the scattered electrons, HRTEM imaging requires a larger objective aperture than traditional TEM imaging.

### 2.4.4 APT

Atom probe tomography (APT) is a technique for 3D compositional imaging and analysis of materials at the atomic scale with high sensitivity and the highest spatial resolution. The generic name of this instrument is 3D atom probe (3DAP)[86].

#### *2.4.4.1 How the atom probe works.*

**Figure 2-25** is the schematic diagram of the atom-probe operation. As shown in **Figure 2-25**a, the sample analysis room must reach ultra-high vacuums (UHV) in$10^{-9}$ Pa range. In order to reduce thermal vibration, the sample should be cooled to a low temperature (20-80k, depending on the nature of the sample). The sample is connected to 1-15k positive high pressure as an anode, which makes the sample tip atoms in the pending ionization state. After a pulse voltage or pulse laser is superimposed on the tip of the sample, the atoms

on its surface ionize and evaporate. The mass charge ratio (m/n) of vaporized ions was measured by the time-of-flight (TOF) mass spectrometer, and the mass spectrum peak of the ions was obtained to determine the element type, as shown in **Figure 2-25**b. The two-dimensional coordinates (x and y) of the flying ions on the surface of the sample tip were recorded with the position-sensitive detector (PSD). The vertical coordinates(z)of the ions were determined through the accumulation of ions layer by layer in the longitudinal direction, and then the three-dimensional(3D) images of different atoms were given, as shown in **Figure 2-25**c[86-90].

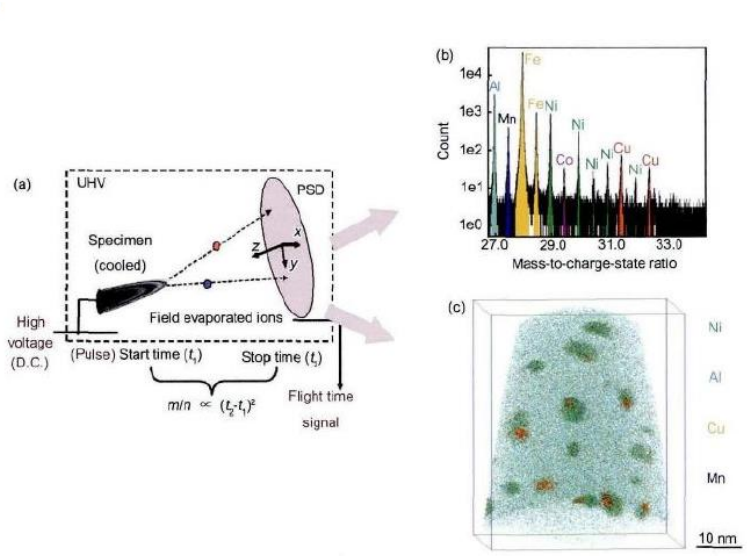


**Figure 2-25. Schematic diagram of atom-probe operation. (a)Data acquisition(m/n-mass to charge ration, PSD-Position sensitive detector )(b)Mass spectrum(c)3D image[90].**

### *2.4.4.2 Applications*

Instrumental advances have facilitated the application of APT from conductive metal materials to semiconductor materials and brittle materials, as well as new applications in

the battery, catalyst, geological and biological materials[91]. APT has played a key role in the quantitative analysis of the atomic position and local concentration of the alloying elements in steel materials. It can be used to assess solute segregation to dislocations, early stages of precipitation, dopant distributions, and so on. There are many studies that investigated the microstructure in steel materials by APT and other correlative microscopy[76, 92-95] It is reported that the determination of clusters and nano precipitates is according to their chemical composition, clusters are defined as nanoparticles with a high content of Fe.

#### *2.4.4.3 Challenges*

APT is not perfect, there are some challenges when using APT to analyze precipitation and clustering. First, it is not easy to prepare a good sample for TEM and distinguish clusters and nano precipitations. Secondly, although APT has become an indispensable microanalytical technique for materials research. there are still some limitations of APT[96-98]:

a) the high mechanical stresses in the specimen near the apex,

b) the finite analyzed volume.

c) the limited Specimen yields.

d) Data-reconstruction fidelity.

## 2.5 References

[1] S. Mukherjee, I. Timokhina, C. Zhu, S.P. Ringer, P.D. Hodgson, Clustering and precipitation processes in a ferritic titanium-molybdenum microalloyed steel, Journal of Alloys and Compounds 690 (2017) 621-632.

[2] V.M.H. KONSTRUKCIJSKA, High-strength low-alloy (HSLA) steels, Materiali in tehnologije 45(4) (2011) 295-301.

[3] B. Ma, A study of processing, microstructure and mechanical properties of ultra-high strength microalloyed steel hot band coils for automotive applications, University of Pittsburgh, 2017.

[4] T. Baker, Microalloyed steels, Ironmaking & Steelmaking 43(4) (2016) 264-307.

[5] S. Vervynckt, K. Verbeken, B. Lopez, J. Jonas, Modern HSLA steels and role of non-recrystallisation temperature, International Materials Reviews 57(4) (2012) 187-207.

[6] J.M. Reichert, Structure and properties of complex transformation products in Nb/Mo-microalloyed steels, University of British Columbia, 2016.

[7] c.H. Young, H. Bhadeshia, Strength of mixtures of bainite and martensite, Materials Science and Technology 10(3) (1994) 209-214.

[8] A. Iza-Mendia, I. Gutiérrez, Generalization of the existing relations between microstructure and yield stress from ferrite–pearlite to high strength steels, Materials Science and Engineering: A 561 (2013) 40-51.

[9] I. Gutiérrez, M. Altuna, Work-hardening of ferrite and microstructure-based modelling of its mechanical behaviour under tension, Acta Materialia 56(17) (2008) 4682-4690.

[10] L. García-Sesma, B. López, B. Pereda, Effect of coiling conditions on the strengthening mechanisms of Nb microalloyed steels with high Ti addition levels, Materials Science and Engineering: A 748 (2019) 386-395.

[11] L. Sanz, B. Pereda, B. López, Effect of thermomechanical treatment and coiling temperature on the strengthening mechanisms of low carbon steels microalloyed with Nb, Materials Science and Engineering: A 685 (2017) 377-390.

[12] J. Adamczyk, Development of the microalloyed constructional steels, Journal of Achievements in Materials and Manufacturing Engineering 14(1-2) (2006) 9-20.

[13] J.W. Martin, Precipitation hardening: theory and applications, Butterworth-Heinemann2012.

[14] Z. Xiong, I. Timokhina, E. Pereloma, Clustering, nano-scale precipitation and strengthening of steels, Progress in Materials Science 118 (2021) 100764.

[15] Z. Jiao, J. Luan, M.K. Miller, C. Yu, C. Liu, Effects of Mn partitioning on nanoscale precipitation and mechanical properties of ferritic steels strengthened by NiAl nanoparticles, Acta Materialia 84 (2015) 283-291.

[16] J. Takahashi, K. Kawakami, Y. Kobayashi, Consideration of particle-strengthening mechanism of copper-precipitation-strengthened steels by atom probe tomography analysis, Materials Science and Engineering: A 535 (2012) 144-152.

[17] Z. Jiao, J. Luan, M. Miller, C.T. Liu, Precipitation mechanism and mechanical properties of an ultra-high strength steel hardened by nanoscale NiAl and Cu particles, Acta Materialia 97 (2015) 58-67.

[18] I. Gutiérrez-Urrutia, D. Raabe, High strength and ductile low density austenitic FeMnAlC steels: Simplex and alloys strengthened by nanoscale ordered carbides, Materials Science and Technology 30(9) (2014) 1099-1104.

[19] N. Kamikawa, Y. Abe, G. Miyamoto, Y. Funakawa, T. Furuhara, Tensile behavior of Ti, Mo-added low carbon steels with interphase precipitation, ISIJ international 54(1) (2014) 212-221.

[20] X. Li, Z. Wang, X. Deng, G. Wang, R. Misra, The determining role of finish cooling temperature on the microstructural evolution and precipitation behavior in an Nb-V-Ti microalloyed steel in the context of newly developed ultrafast cooling, Metallurgical and Materials Transactions A 47 (2016) 1929-1938.

[21] T. Gladman, Precipitation hardening in metals, Materials science and technology 15(1) (1999) 30-36.

[22] H. Halfa, Recent trends in producing ultrafine grained steels, Journal of Minerals and Materials Characterization and Engineering 2014 (2014).

[23] S. Shanmugam, M. Tanniru, R. Misra, D. Panda, S. Jansto, Microalloyed V–Nb–Ti and V steels Part 2–Precipitation behaviour during processing of structural beams, Materials science and technology 21(2) (2005) 165-177.

[24] S. Liang, Thermomechanical processing of microalloyed steels: experiments and modelling, 2020.

[25] D. Belato Rosado, W. De Waele, D. Vanderschueren, S. Hertelé, Latest developments in mechanical properties and metallurgical features of high strength line pipe steels, 5th International Conference on Sustainable Construction and Design, Ghent University, Laboratory Soete, 2013.

[26] W.D. Callister, D.G. Rethwisch, Materials science and engineering (Vol. 5), NY: John wiley & sons (2011) 72-82.

[27] G. Krauss, S.W. Thompson, Ferritic microstructures in continuously cooled low-and ultralow-carbon steels, ISIJ international 35(8) (1995) 937-945.

[28] D. Phelan, N. Stanford, R. Dippenaar, In situ observations of Widmanstätten ferrite formation in a low-carbon steel, Materials Science and Engineering: A 407(1-2) (2005) 127-134.

[29] H.K.D.H. Bhadeshia, Bainite in steels: theory and practice, CRC press2019.

[30] H. Bhadeshia, Allotriomorphic Ferrite, Retrieved May 20 (2010) 2012.

[31] Y. Li, T. Baker, Effect of morphology of martensite–austenite phase on fracture of weld heat affected zone in vanadium and niobium microalloyed steels, Materials science and technology 26(9) (2010) 1029-1040.

[32] S. Zajac, Precipitation of microalloy carbo-nitrides prior, during and after γ/α transformation, Materials Science Forum, Trans Tech Publ, 2005, pp. 75-86.

[33] W. Morrison, The Strengthening of Carbon Steels by Small Niobium Additions, Iron &Steel 8 (1964) 390-395.

[34] H.-W. Yen, P.-Y. Chen, C.-Y. Huang, J.-R. Yang, Interphase precipitation of nanometer-sized carbides in a titanium–molybdenum-bearing low-carbon steel, Acta Materialia 59(16) (2011) 6264-6274.

[35] J. Bee, P. Howell, R. Honeycombe, Isothermal transformations in iron-chromium-carbon alloys, Metallurgical Transactions A 10 (1979) 1207-1212.

[36] A. Davenport, R.W.K. Honeycombe, Precipitation of carbides at γ─ α boundaries in alloy steels, Proceedings of the Royal Society of London. A. Mathematical and Physical Sciences 322(1549) (1971) 191-205.

[37] T. Gladman, The physical metallurgy of microalloyed steels, Maney Pub1997.

[38] Y. Shen, C.M. Wang, X. Sun, A micro-alloyed ferritic steel strengthened by nanoscale precipitates, Materials Science and Engineering: A 528(28) (2011) 8150-8156.

[39] K.Y. Xie, T. Zheng, J.M. Cairney, H. Kaul, J.G. Williams, F.J. Barbaro, C.R. Killmore, S.P. Ringer, Strengthening from Nb-rich clusters in a Nb-microalloyed steel, Scripta Materialia 66(9) (2012) 710-713.

[40] H.J. Kong, C.T. Liu, A review on nano-scale precipitation in steels, Technologies 6(1) (2018) 36.

[41] H. Zurob, Effects of precipitation, recovery and recrystallization on the microstructural evolution of microalloyed austenite, 2003.

[42] C.M. Tamarelli, The evolving use of advanced high-strength steels for automotive applications, Steel Market Development Institute, Michigan (2011).

[43] S. Park, S. Yue, J. Jonas, Continuous-cooling-precipitation kinetics of Nb (CN) in high-strength low-alloy steels, Metallurgical Transactions A 23 (1992) 1641-1651.

[44] S.F. Medina, Determination of precipitation–time–temperature (PTT) diagrams for Nb, Ti or V micro-alloyed steels, Journal of materials science 32 (1997) 1487-1492.

[45] C. Klinkenberg, K. Hulka, W. Bleck, Niobium carbide precipitation in microalloyed steel, steel research international 75(11) (2004) 744-752.

[46] Z. Jia, R. Misra, R. O'malley, S. Jansto, Fine-scale precipitation and mechanical properties of thin slab processed titanium–niobium bearing high strength steels, Materials Science and Engineering: A 528(22-23) (2011) 7077-7083.

[47] F. Bu, X. Wang, S. Yang, C. Shang, R. Misra, Contribution of interphase precipitation on yield strength in thermomechanically simulated Ti–Nb and Ti–Nb–Mo microalloyed steels, Materials Science and Engineering: A 620 (2015) 22-29.

[48] H.-J. Kestenbach, S. Campos, E. Morales, Role of interphase precipitation in microalloyed hot strip steels, Materials science and technology 22(6) (2006) 615-626.

[49] H. Dong, H. Chen, W. Wang, Y. Zhang, G. Miyamoto, T. Furuhara, C. Zhang, Z. Yang, S. van der Zwaag, Analysis of the interaction between moving α/γ interfaces and interphase precipitated carbides during cyclic phase transformations in a Nb-containing Fe-C-Mn alloy, Acta Materialia 158 (2018) 167-179.

[50] S. Clark, V. Janik, A. Rijkenberg, S. Sridhar, Analysis of the extent of interphase precipitation in V-HSLA steels through in-situ characterization of the γ/α transformation, Materials Characterization 115 (2016) 83-89.

[51] A. Davenport, F. Berry, R. Honeycombe, Interphase precipitation in iron alloys, Metal Science Journal 2(1) (1968) 104-106.

[52] R. Okamoto, A. Borgenstam, J. Ågren, Interphase precipitation in niobium-microalloyed steels, Acta Materialia 58(14) (2010) 4783-4790.

[53] S. Liang, X. Wang, C. Andrei, H.S. Zurob, NbC precipitation during two-pass hot deformation of a nickel-based model alloy at 700° C: Experiments and modelling, Materials Science and Engineering: A 802 (2021) 140447.

[54] S. Liang, X. Wang, H.S. Zurob, NbC precipitation during multi-pass deformation of a nickel-based model alloy: Experiments and modelling, Materials Science and Engineering: A 772 (2020) 138748.

[55] B. Dutta, E.J. Palmiere, C.M. Sellars, Modelling the kinetics of strain induced precipitation in Nb microalloyed steels, Acta materialia 49(5) (2001) 785-794.

[56] P. Gong, E.J. Palmiere, W.M. Rainforth, Characterisation of strain-induced precipitation behaviour in microalloyed steels during thermomechanical controlled processing, Materials Characterization 124 (2017) 83-89.

[57] D. Poddar, P. Cizek, H. Beladi, P.D. Hodgson, Evolution of strain-induced precipitates in a model austenitic Fe–30Ni–Nb steel and their effect on the flow behaviour, Acta materialia 80 (2014) 1-15.

[58] V. Challa, W. Zhou, R. Misra, R. O'Malley, S. Jansto, The effect of coiling temperature on the microstructure and mechanical properties of a niobium–titanium microalloyed steel processed via thin slab casting, Materials Science and Engineering: A 595 (2014) 143-153.

[59] J. Omale, E. Ohaeri, J. Szpunar, M. Arafin, F. Fateh, Microstructure and texture evolution in warm rolled API 5L X70 pipeline steel for sour service application, Materials Characterization 147 (2019) 453-463.

[60] J. Omale, E. Ohaeri, A. Tiamiyu, M. Eskandari, K. Mostafijur, J. Szpunar, Microstructure, texture evolution and mechanical properties of X70 pipeline steel after different thermomechanical treatments, Materials Science and Engineering: A 703 (2017) 477-485.

[61] S.-I. Lee, S.-Y. Lee, S.G. Lee, H.G. Jung, B. Hwang, Effect of strain aging on tensile behavior and properties of API X60, X70, and X80 pipeline steels, Metals and Materials International 24 (2018) 1221-1231.

[62] H. Zurob, Y. Brechet, G. Purdy, A model for the competition of precipitation and recrystallization in deformed austenite, Acta materialia 49(20) (2001) 4183-4190.

[63] H. Zurob, C. Hutchinson, Y. Brechet, G. Purdy, Modeling recrystallization of microalloyed austenite: effect of coupling recovery, precipitation and recrystallization, Acta materialia 50(12) (2002) 3077-3094.

[64] S.F. Medina, A. Quispe, M. Gomez, Model for strain-induced precipitation kinetics in microalloyed steels, Metallurgical and Materials Transactions A 45(3) (2014) 1524-1539.

[65] Z. Wang, X. Mao, Z. Yang, X. Sun, Q. Yong, Z. Li, Y. Weng, Strain-induced precipitation in a Ti micro-alloyed HSLA steel, Materials Science and Engineering: A 529 (2011) 459-467.

[66] S. Hong, K. Kang, C. Park, Strain-induced precipitation of NbC in Nb and Nb–Ti microalloyed HSLA steels, Scripta materialia 46(2) (2002) 163-168.

[67] X. Ma, C. Miao, B. Langelier, S. Subramanian, Suppression of strain-induced precipitation of NbC by epitaxial growth of NbC on pre-existing TiN in Nb-Ti microalloyed steel, Materials & Design 132 (2017) 244-249.

[68] C. Gu, M.J. Gaudet, J. Su, B. Langelier, H. Yuan, N. Bassim, H. Zurob, Advanced Characterization of Precipitation and Microstructure Heterogeneity in X70 Steel, Metallurgical and Materials Transactions A (2022) 1-8.

[69] A. Craven, K. He, L. Garvie, T. Baker, Complex heterogeneous precipitation in titanium–niobium microalloyed Al-killed HSLA steels—I.(Ti, Nb)(C, N) particles, Acta Materialia 48(15) (2000) 3857-3868.

[70] H. Zhang, H. Xiong, First-principles study of NbC heterogeneous nucleation on TiC vs. TiN in microalloy steel, Ironmaking & Steelmaking (2018).

[71] F. Perrard, A. Deschamps, P. Maugis, Modelling the precipitation of NbC on dislocations in α-Fe, Acta Materialia 55(4) (2007) 1255-1266.

[72] A. Deschamps, Y. Brechet, Influence of predeformation and ageing of an Al–Zn–Mg alloy—II. Modeling of precipitation kinetics and yield stress, Acta Materialia 47(1) (1998) 293-305.

[73] D. Phelan, M.H. Reid, R. Dippenaar, High Temperature Laser Scanning Confocal Microscopy for real-time studies of phase transformations, Microscopy and Microanalysis 11(S02) (2005) 670-671.

[74] W. Mu, P. Hedström, H. Shibata, P.G. Jönsson, K. Nakajima, High-temperature confocal laser scanning microscopy studies of ferrite formation in inclusion-engineered steels: a review, Jom 70 (2018) 2283-2295.

[75] B. Tata, B. Raj, Confocal laser scanning microscopy: Applications in material science and technology, Bulletin of Materials Science 21 (1998) 263-278.

[76] X. Wang, C. Wang, J. Kang, G. Yuan, R. Misra, G. Wang, An in-situ microscopy study on nucleation and growth of acicular ferrite in Ti-Ca-Zr deoxidized low-carbon steel, Materials Characterization 165 (2020) 110381.

[77] C.-K. Lin, Y.-C. Pan, W.-S. Hwang, Y.-C. Fang, Y.-H. Su, G.-R. Lin, Y.-F. Wu, In situ observation of growth behaviour of acicular ferrite in low-carbon steel containing 13 ppm magnesium, Ironmaking & Steelmaking 46(2) (2019) 176-183.

[78] S. Clark, Y.J. Lan, V. Janik, A. Rijkenberg, S. Sridhar, In situ characterisation of austenite/ferrite transformation kinetics and modelling of interphase precipitation inter-sheet spacing in V microalloyed HSLA steels, Materials Science Forum, Trans Tech Publ, 2017, pp. 356-362.

[79] A.J. Wilkinson, T.B. Britton, Strains, planes, and EBSD in materials science, Materials today 15(9) (2012) 366-376.

[80] EBSD.

[81] S. Zaefferer, P. Romano, F. Friedel, EBSD as a tool to identify and quantify bainite and ferrite in low-alloyed Al-TRIP steels, Journal of microscopy 230(3) (2008) 499-508.

[82] Y.-W. Chen, Y.-T. Tsai, P.-Y. Tung, S.-P. Tsai, C.-Y. Chen, S.-H. Wang, J.-R. Yang, Phase quantification in low carbon Nb-Mo bearing steel by electron backscatter diffraction technique coupled with kernel average misorientation, Materials Characterization 139 (2018) 49-58.

[83] A.H. Cottrell, The mechanical properties of matter, (1964).

[84] S.-I. Lee, S.-Y. Lee, S.G. Lee, H.G. Jung, B. Hwang, Effect of strain aging on tensile behavior and properties of API X60, X70, and X80 pipeline steels, Metals and Materials International 24(6) (2018) 1221-1231.

[85] D.B. Williams, C.B. Carter, D.B. Williams, C.B. Carter, The transmission electron microscope, Springer1996.

[86] M.K. Miller, Atom probe tomography: analysis at the atomic level, Springer Science & Business Media2012.

[87] B. Gault, M.P. Moody, J.M. Cairney, S.P. Ringer, Atom probe microscopy, Springer Science & Business Media2012.

[88] T.F. Kelly, M.K. Miller, Atom probe tomography, Review of scientific instruments 78(3) (2007) 031101.

[89] D.J. Larson, T. Prosa, R.M. Ulfig, B.P. Geiser, T.F. Kelly, Local electrode atom probe tomography, New York, US: Springer Science 2 (2013).

[90] W. LIU, Q. LIU, J. GU, Development and application of atom probe tomography, Acta Metall Sin 49(9) (2013) 1025-1031.

[91] A. Devaraj, D.E. Perea, J. Liu, L.M. Gordon, T.J. Prosa, P. Parikh, D.R. Diercks, S. Meher, R.P. Kolli, Y.S. Meng, Three-dimensional nanoscale characterisation of materials by atom probe tomography, International Materials Reviews 63(2) (2018) 68-101.

[92] F. Danoix, P. Auger, Atom probe studies of the Fe–Cr system and stainless steels aged at intermediate temperature: a review, Materials characterization 44(1-2) (2000) 177-201.

[93] T. Hamaoka, A. Nomoto, K. Nishida, K. Dohi, N. Soneda, Accurate determination of the number density of G-phase precipitates in thermally aged duplex stainless steel, Philosophical Magazine 92(22) (2012) 2716-2732.

[94] R. Veerababu, R. Balamuralikrishnan, K. Muraleedharan, M. Srinivas, Three-dimensional atom probe investigation of microstructural evolution during tempering of an ultra-high-strength high-toughness steel, Metallurgical and Materials Transactions A 39 (2008) 1486-1495.

[95] J. Takahashi, K. Kawakami, Y. Kobayashi, Application of atom probe tomography to fundamental issues of steel materials, Surface and Interface Analysis 51(1) (2019) 12-16.

[96] D.J. Larson, B. Gault, B.P. Geiser, F. De Geuser, F. Vurpillot, Atom probe tomography spatial reconstruction: Status and directions, Current Opinion in Solid State and Materials Science 17(5) (2013) 236-247.

[97] F. Vurpillot, B. Gault, B.P. Geiser, D. Larson, Reconstructing atom probe data: A review, Ultramicroscopy 132 (2013) 19-30.

[98] T.F. Kelly, D.J. Larson, Atom probe tomography 2012, Annual review of materials research 42 (2012) 1-31.

# Chapter 3 Advanced Characterization of Precipitation and Microstructure Heterogeneity in X70 Steel

This chapter is reproduced from ***Chen Gu***, *Michael J. Gaudet, Jing Su, Brian Langelier, Hui Yuan, Nabil Bassim, and Hatem Zurob. "Advanced Characterization of Precipitation and Microstructure Heterogeneity in X70 Steel." Metallurgical and Materials Transactions A (2022): 1-8. (https://doi.org/10.1007/s11661-022-06930-9*. This chapter also includes some minor updating based on the suggestion from the committee during defence. The author of this thesis is the first author and the main contributor to this publication, including conceiving the initial ideas, development of approach and methodology, carrying out experiments, analysis of data, and preparation of the manuscript.

## 3.1 Abstract

The spatial distribution of precipitates and microstructure heterogeneity in a vacuum induction melted X70 steel rolled at a pilot-scale facility were investigated using advanced characterization techniques. Electron Backscatter Diffraction (EBSD) was used to identify areas with low and high Kernel Average Misorientation (KAM). A newly developed procedure utilizing a Plasma Focused Ion Beam (PFIB) microscope was used to lift out plane view sections of small and large grains within the areas of low and high KAM values. Quantitative analysis by transmission electron microscopy (TEM) revealed a uniformly dispersed set of core-cap structure precipitates varying between 30 and 70 nm in diameter.

The core was enriched in Ti and N, while the shell typically contained Nb and C. Strain-induced precipitation of fine (5-20 nm) NbC particles on dislocations were not observed by TEM and 3D atom probe tomography (APT). The absence of strain-induced precipitation is believed to be due to the depletion of Nb from solid solution as the result of the core-cap structure of NbC on pre-existing TiN particles. The similarity of precipitates in each location suggests that the local features (strain, grain size) in the final microstructure arise from phase transformations during cooling.

## 3.2 Introduction

Microalloyed steels are widely used due to their high strength, low-impact transition temperature, good weldability and low cost. These steels are widely used for oil and gas pipelines and automobile components[1-5]. Precipitates play a prominent role in the design of microalloyed steels through their direct impact on mechanical and fracture properties. Microalloyed precipitates are critical for controlling the final microstructure and grain size during thermo-mechanically controlled processing (TMP). The precipitates formed are usually of the type MX, where M is Ti, Nb and/or V and X is C and/or N[5, 6].

Microalloyed precipitates that form during TMP are commonly classified as strain-induced precipitates(SIP), interphase precipitates, or matrix precipitates[1-7]. SIP nucleate on dislocations during hot deformation in austenite. The precipitation of strain-induced NbC is employed in controlled rolling to suppress recrystallization and obtain “pancaked” austenite with a large surface area to volume ratio in order to promote the formation of fine-

grained ferrite during austenite decomposition[7-12]. Under some processing conditions, interphase precipitates, form on the austenite(γ)/Ferrite(α) interface during the phase transformation. These precipitates are usually aligned in finely spaced rows, leading to an important increase in the strength of the steel[13-18]. Precipitates that form in supersaturated ferrite following the austenite-to-ferrite transformation are commonly referred to as matrix precipitates[7, 19, 20]. Matrix precipitates are extremely fine, leading to a significant precipitation hardening contribution.

Precipitates in micro-alloyed steels have been investigated extensively using TEM. In most of the existing literature, the analysis is carried out either on thin TEM foils prepared by electropolishing or carbon extraction replicas from polished surfaces[7-20]. Due to the limitations of these sample preparation methods, the samples analyzed in most of the literature are not site-specific. Thus, precipitates in different regions within the microstructure have not been investigated and discussed in detail. A site-specific characterization method brings insights into precipitation characteristics with respect to the local microstructure features. Because steels have complex microstructure, including variations of dislocation density, grain size, and austenite decomposition products (such as polygonal ferrite-PF, acicular ferrite-AF, granular bainite-GB, bainitic ferrite-BF.) [21-23]. For example, hot-rolled line pipe steels often contain PF, AF, and GB/BF. It is difficult, using conventional, random sampling methods, to determine whether interphase precipitation has taken place during the formation of PF, or the extent of micro alloyed precipitation within PF, AF, and BF. It is also difficult to determine the extent to which SIP

may have contributed to the development of the final microstructure (e.g. due to partial recrystallization or interaction with subsequent phase transformations).

In order to investigate the precipitates in different regions within the microstructure, a detailed investigation of precipitation in an X70 steel was carried out with special emphasis on studying precipitation in areas of small/large grain size and low/high KAM in this work. To achieve this, a rarely used sample preparation method that allows plane view lift-out of TEM foils was used[24, 25]. To start, EBSD mapping is used to identify the various regions of interest within the microstructure of the bulk sample. PFIB milling is then used to lift out a plane view thin foil from these areas of interest. Then, Energy Dispersive Spectroscopy (EDS), Electron Energy Loss Spectroscopy (EELS) in the TEM, and 3D APT were used to conduct a detailed analysis of the precipitates in these different areas. Using this site-specific data, one is able to comment on precipitation within different features of the microstructure.

## 3.3 Material and methods

### 3.3.1 Material

The material used in the present study is an X70 line pipe steel that was vacuum induction melt cast and rolled by CanmetMATERIALS(Hamilton, Canada). The chemical composition of the steel is given in **Table 3- 1**.

**Table 3- 1.Chemical composition of X70 sample(wt%)**

| **C** | **Mn** | **Si** | **Cr** | N |
|---|---|---|---|---|
| 0.042 | 1.32 | 0.27 | 0.24 | 0.006 |
| **Nb** | **Mo** | **Al** | **Ti** | |
| 0.087 | 0.24 | 0.036 | 0.017 | |

The experimental steel was cast and hot-rolled at the pilot mill facilities of CanmentMATERIALS (Hamilton, Canada). The steel was vacuum induction melted and poured into 190 mm x 230 mm x 240 mm ingots. Then the ingot was reheated to 1190 °C and soaked for 4 hours, followed by roughing between 1080 and 1030°C (70% total reduction) and finishing between 920 and 820°C (75% total reduction). The plate was then cooled on the run-out table using laminar water flow (~30°C /s) and placed in a furnace at 510°C to simulate coiling. The solubility temperatures of TiN and NbC in the studied material are around 1499°C and 1150°C respectively. Some pre-existing TiN may be present in the studied material because the reheating temperature is lower than the dissolving temperature of TiN. For this reason, the distribution of the TiN cores is essentially the same as TiN distribution in the reheated sample. The Ae3(para equilibrium) of the studied material is calculated to be around 837°C by Thermocalc. The austenite non-recrystallization temperature (Tnr) was calculated to be 1033°C. The finishing rolling temperature is below the Tnr and above Ae3(supercooling is needed for the phase transformation). Thermomechanical processing details of the as-received steel are shown in **Table 3-2**.

**Table 3-2 Thermomechanical processing of X70. (Tnr: non-recrystallization temperature, $T_{(TiN)}$: solubility temperatures of TiN, $T_{(NbC)}$: solubility temperatures of NbC).**

| Reheat temp. | Roughing (70% reduction) | Finishing (75% reduction) | Cooling rate | Coiled Simulation at |
|---|---|---|---|---|
| 1190°C | 1080-1030°C | 920-820°C | 30°C /s | 510°C |
| **Ae3(para)** | **Tnr** | **$T_{(TiN)}$** | **$T_{(NbC)}$** | |
| 837°C | 1033°C | 1499°C | 1150°C | |

### 3.3.2 Methods

The as-received steel plate was characterized at the quarter thickness (TD-RD plane) using EBSD. To find the same area in EBSD and PFIB microscope, the sample was prepared by mechanical polishing and etched with 2% nital for approximately 30s to provide some topography for easy matching. All EBSD analyses were performed using a JEOL JSM-7000F SEM equipped with a Nordlys II EBSD Camera. The EBSD data was then processed in HKL Channel 5 EBSD post-processing software. In addition, cylindrical samples with a diameter of 4 mm and a length of 10 mm were machined from the as-received material by Electrical Discharge Machining (EDM) for the austenitizing experiments in a BAHR DIL 805 dilatometer and the dilatation was recorded to understand the phase transformation of the material. The sample is heated to 900 °C at 10 °C/s heating rate. After holding at 900 °C for 10min, the sample is cooled to 510 °C at 30 °C/s cooling rate and held for 30 min at 510 °C before cooling to room temperature at 30 °C/s cooling rate.

Following the EBSD analysis, four different positions (P1-Small grain with small strain; P2-Small grain with large strain; P3-large grain with small strain; P4-large grain with large

strain) were chosen for FIB lift-out as shown in **Figure 3- 1**. These areas (the sample size was around ~10 15um2)were extracted by the plane view[24, 25] lift-out method in a Thermo Fisher Scientific Helios G4 UXe Dual-Beam PFIB microscope. Then these samples were imaged in a Thermo Fisher Scientific Talos 200X TEM equipped with four in-column silicon drift EDX (SDD) Super-X detectors in Scanning TEM (STEM) mode. The composition, morphology, and distribution of the particles were measured by EDS in the whole TEM samples with different magnifications. The thickness of the TEM sample was measured by EELS [26] on a FEI Titan 80-300 HB in STEM mode. These instruments were operated at 200 keV.

Selected 3D APT samples were prepared using the PFIB by mounting to Si microtips using a standard lift-out method[27]. A Cameca local electrode atom probe (LEAP) 4000X HR was used for APT experiments at a base temperature of 59.7 K in laser pulsing mode ($\lambda$ = 355 nm), with a pulse rate of 250 kHz, a pulse energy in the range of 50–60 pJ and a targeted detection rate of 0.01 ions/pulse (1 %). Reconstruction and analysis of APT data were performed using IVAS 3.6.8 software and established reconstruction protocols[28, 29]. Reconstructions were spatially calibrated using the known spacing of crystal planes.

## 3.4 Results

### 3.4.1 Heterogeneous microstructure

**Figure 3- 1** shows EBSD data of the X70 steel at the quarter thickness. It exhibits a heterogeneous microstructure consisting of bainitic ferrite and quasi-polygonal ferrite.

**Figure 3- 1**b is the Local Misorientation/KAM map, which is the average misorientation angle of a given point with respect to all of its neighbors[30, 31]. The strain contour map is colored from blue to red according to this misorientation value. It can be used to measure the geometrically necessary dislocation (GND) density and assess the local plastic strain developed in the steel during the process of rolling. It is reported that low-temperature transformation microstructures such as AF, GB, and BF have higher degree of deformation and strain concentration compared to PF. This suggests that the low KAM areas (shown in blue in **Figure 3- 1**b) consist of PF that formed at high temperature, while the high KAM areas (shown in green in **Figure 3- 1**b) are BF or GB which formed at lower temperatures during cooling or coiling[23]. **Figure 3- 1**c is the inverse pole figure in the ND direction. It shows that the orientation of this region is relatively random and there is no strong texture.

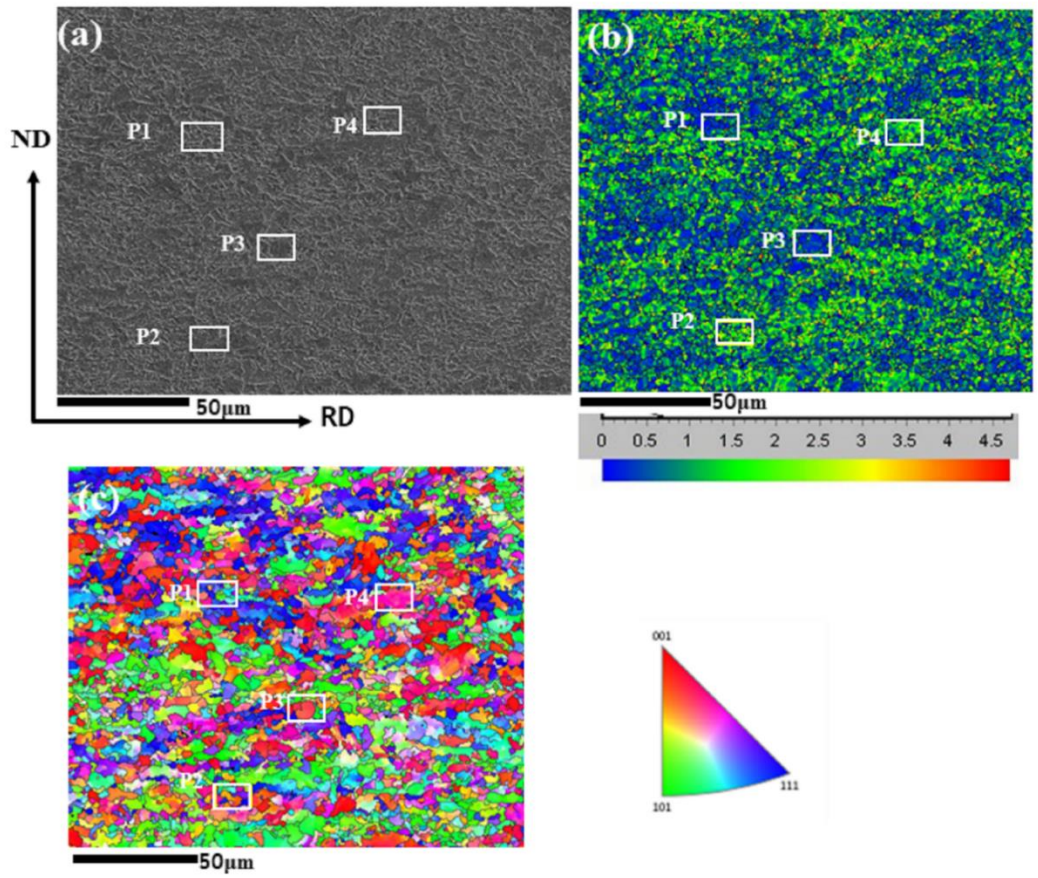


**Figure 3- 1. EBSD data of X70 at quarter thickness (Rolling direction: RD; Normal direction: ND): a) SEM image. b) Local Misorientation/Kernel Average Misorientation map. c) inverse pole figure (IPF-Z) map (P1-Small grain with small strain; P2-Small grain with large strain; P3-large grain with small strain; P4-large grain with large strain.)**

In order to better understand the initial microstructure of the material, samples were heat-treated using the BAHR DIL 805 dilatometer and the result was shown in **Figure 3-2**. The dilatation curve indicates that PF is formed below ~720 ˚C. There is evidence of bainite formation at lower temperatures and during the isothermal holding at 510 ˚C in **Figure 3-2**[32].

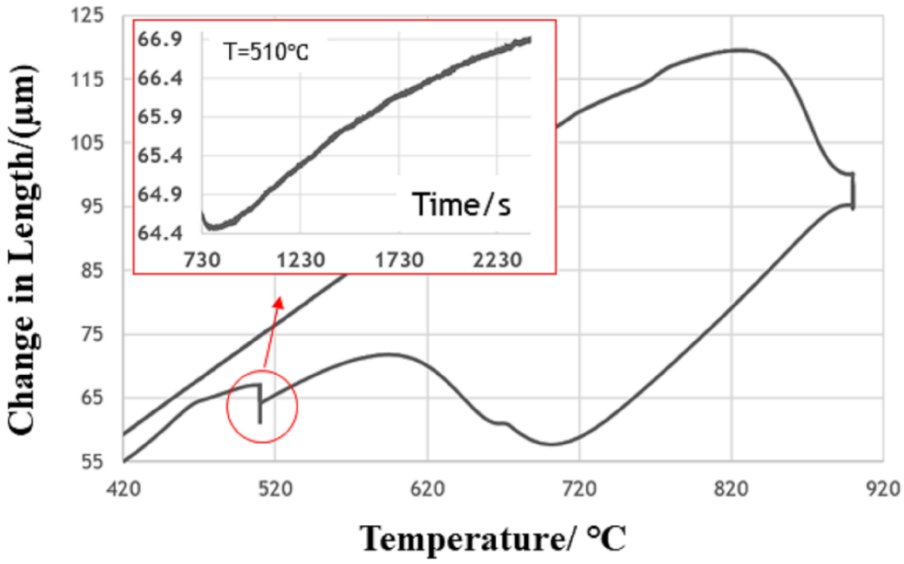


**Figure 3-2. Thermal dilatometric curve of X70 steel, inset shows dilatometric-time curve at isothermal hold of 510°C.**

The dilatometer experiment suggests that phase transformation is occurring over a range of temperatures, some of which is likely to occur at the coiling temperature. Inspection of the nital-etched sample reveals bainitic ferrite and quasi-polygonal ferrite. While the dilatometer experiment provides some insight into how a complex microstructure can develop at the cooling rate and coiling temperature of interest, the relationship between the local precipitation and local microstructure is not clear. Site-specific sampling allows for the correlation of the precipitate analysis to specific regions within the microstructure. Four different areas are chosen based on the KAM map and IPF-Z map in **Figure 3- 1**. Position P1 is an area with small grain size and relatively small strain, position P2 is an area with

small grain size and relatively large strain. In contrast, positions P3 and P4 come from large grains with small strain and large strain, respectively.

### 3.4.2 Precipitate Distribution

Figure 3 shows the characterization result of P1 (small grain size and small strain). The corresponding area can be found in **Figure 3- 1**. In this region, the grain size is around 2.5 μm, and the KAM value of the whole area is relatively smaller compared to P2 and P4, as shown in **Figure 3-3**b. A TEM sample is lifted out by the plan view method in PFIB. The primary analysis area is shown by the yellow rectangular in **Figure 3-3**a and 3b. EDS was used to carry out a detailed analysis of precipitates in this sample.

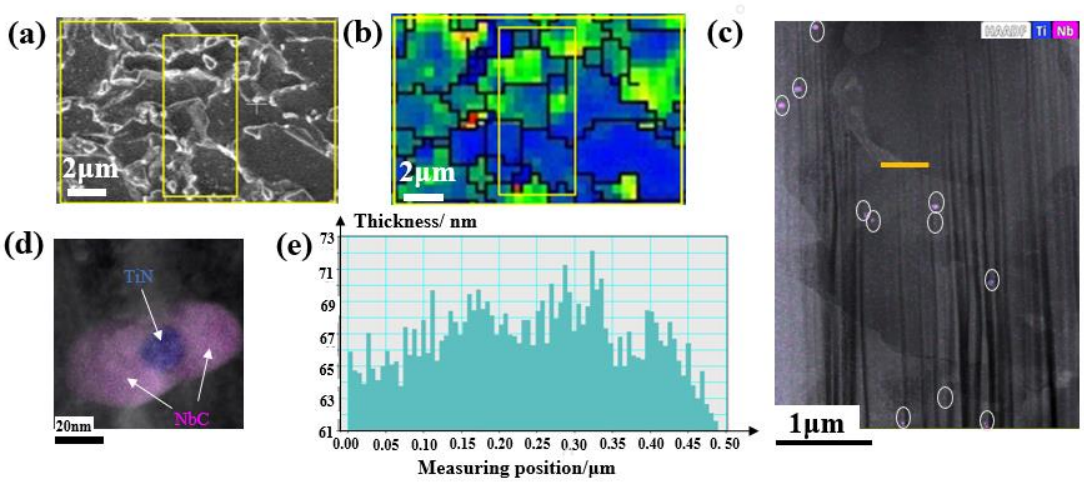


**Figure 3-3. EBSD and TEM images of P1 (small grain with small strain): a) SEM image. b) Local Misorientation/Kernel Average Misorientation map. c) precipitates distribution in EDS map(yellow line is where the thickness measurement carried out). d) typical precipitates in p1(EDS map); e) thickness map from EELS.**

**Figure 3-3**c shows some of the precipitates that were identified using EDS analysis. It is worth pointing out that **Figure 3-3**c is just one of the analysed areas in the yellow rectangular of **Figure 3-3**(a-b). The precipitates in P1 have a core-cap structure, as shown in **Figure 3-3**d. The core was rich in Ti and N, while the cap typically contained Nb and C (more examples of the core-cap structure / epitaxial growth precipitates can be found in the electronic supplementary **Figure 3-7**.). Most precipitates were in the 40 to 60 nm size range. Fine nano precipitates (< 10 nm) were not found in P1 in spite detailed EDS mapping in the whole TEM samples with different magnifications. In total 11 precipitates were observed in an area of 16 $um^2$. The thickness of the foil was measured to be ~70 nm using EELS (**Figure 3-3**e). The thickness of the sample is uneven because of the curtaining and holes introduced during sample preparation in PFIB. In this way, a precipitate number density of $1x10^{19}$ $m^{-3}$ was calculated.

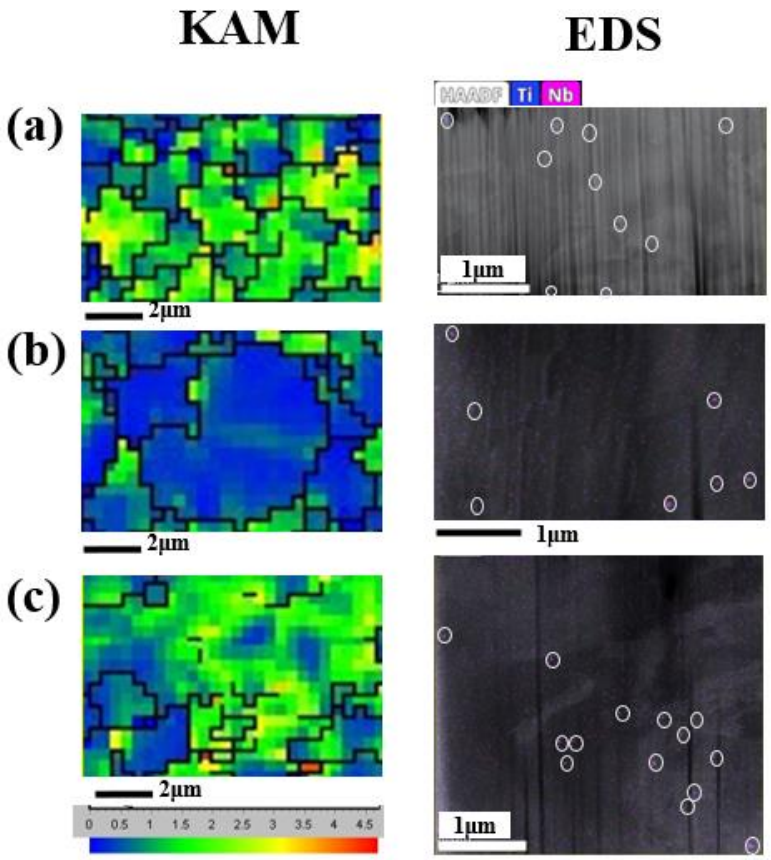


**Figure 3-4. KAM map, precipitates distribution in STEM-EDS map at different positions: a) P2 (small grain and large strain. b) P3 (large grain and small strain). c) P4(large grain and large strain).**

The same analysis was carried out on samples from the other three locations. The corresponding KAM map, EDS map are shown in **Figure 3-4**(the EDS mapping area for each sample is just one of the analysis areas in the KAM map). As mentioned before, P2 is the area with small grain size (around 2.5 μm) and large KAM value, as shown in **Figure 3- 1** and **Figure 3-4**a. The precipitates in P2 are similar to the precipitates in P1, in that they mainly contain Ti and Nb, and have a size of ~60 nm. Fine NbC precipitates (<10 nm)

were not found in P2 either. The number density of precipitates in this area was around $1x10^{19}$ $m^{-3}$ with thickness around 85 μm.

A larger grain size (around 6 μm) is observed in areas P3(thickness around 50 μm) and P4(thickness around 35μm). Area P3 had small strain as measured by KAM (**Figure 3-4**b), while area P4 had a larger strain (**Figure 3-4**c). The size of the precipitates in P3 and P4 was in the range of 40-60 nm. Fine nanoparticles (<10 nm) which contains Nb were not observed in either specimen. The calculated precipitate number densities were $2x10^{19}$ $m^{-3}$ in P3 and $2.5x10^{19}$ $m^{-3}$ in P4, respectively.

Fine NbC precipitates (<10nm) are not evident by TEM analysis in the current steel. Such precipitates would be the result of SIP, interphase precipitation and/or matrix precipitation during thermomechanical processing. This is particularly surprising because the finishing temperature was sufficiently low to allow the formation of fine strain-induced niobium carbon nitrides. A more detailed examination to try and observe these fine precipitates was made using APT. Two additional samples (one in a high KAM region and the other in a low KAM region in **Figure 3- 1**) were used. It is worth mentioning that the volume of the material covered by APT characterization is adequate to observe some SIP of NbC provided these are present in a number density of at least $10^{20}$ $m^{-3}$. It is also important to point out that no Ti is detected in the matrix for both samples as most of the Ti is consumed by the large (Ti, Nb)(C, N) precipitates, resulting in a matrix Ti content that is depleted to below detection limits.

The APT reconstruction Nb and C atomic map are presented in **Figure 3-5**. APT data from the low strain area (**Figure 3-5**a) shows Nb and C distributed uniformly in the matrix; there is no evidence for the existence of fine NbC precipitates, which agrees with TEM observations. Similarly, fine (<10 nm) NbC precipitates were not present in the high strain APT tips (**Figure 3-5**b). The sample, however, showed evidence of Nb and C segregation/redistribution to an interface feature in the bottom corner (ROI-1) of **Figure 3-5**b, with a measured C concentration of around 3.14 at.%. This C content would suggest that the interface is between retained austenite and bainitic ferrite. Interestingly Nb also appears to segregate to this interface. Nb segregation is also present at the top of the tip (ROI-2). This region also shows carbon segregation and may correspond to a dislocation line. The 1D line profile of Nb at ROI-1 and ROI-2 in **Figure 3-5**c shows that Nb is segregated in these areas. Similar segregation was also observed by TEM in high strain area P4, as shown in **Figure 3-5**d.

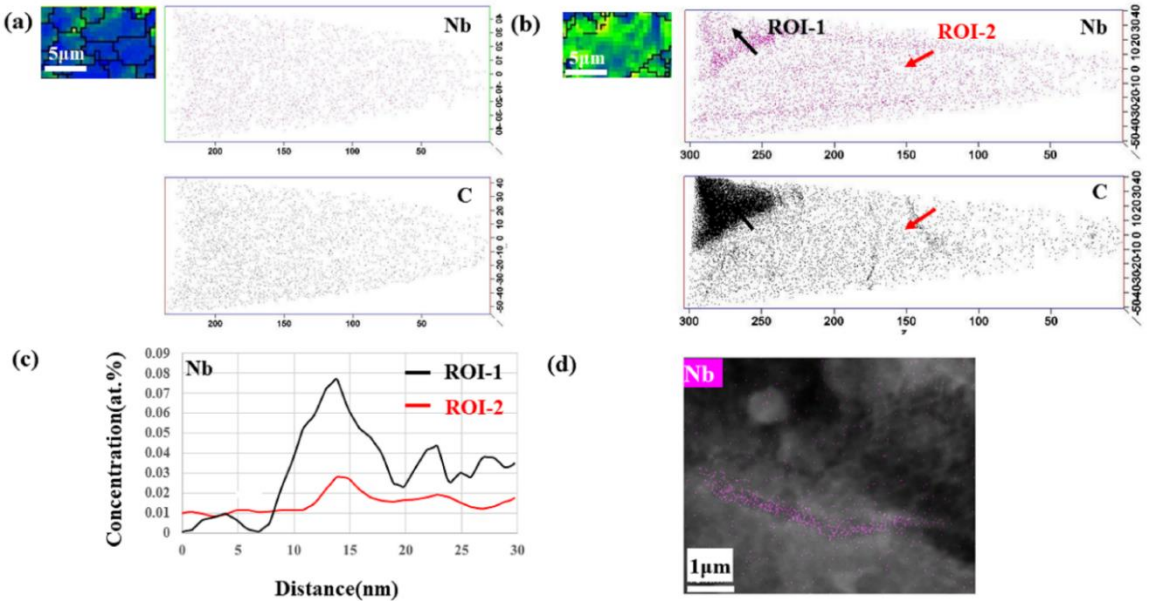


**Figure 3-5. 3D atom probe tomography reconstruction Nb and C atomic map for (a)sample with small strain and (b)sample with large strain; (c) 1D line profile of Nb at ROI-1 and ROI-2; (d) EDS map of Nb segregation in P4**

## 3.5 Discussion

### 3.5.1 Absence of strain-induced precipitation in X70

Typical precipitates that form during the TMP are reviewed in **Figure 3- 6**[33]. Coarse TiN often form during the late stages of solidification and as a result have a large size(>30nm). Subsequently, during the finishing process(900-750℃), strain-induced NbC precipitates (~2-10nm) are usually formed on discoations in austenite. Relevant studies have shown that such precipitates are more likely to form on dislocations because of the lower nucleation energy barrier[7-12]. During the subsequent cooling process, there is a possibility for the

formation of interphase precipitates at the ferrite/austenite interface. Fine precipitates (< 10 nm) may also form within ferrite during coiling.

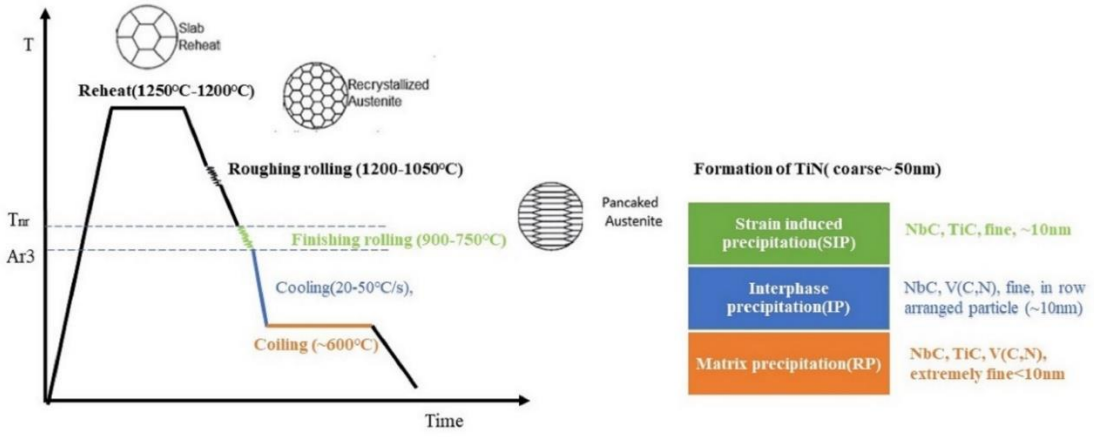


**Figure 3- 6. Typical precipitates during thermo-mechanically controlled process.**

In the present investigation, fine NbC precipitates were not observed, suggesting that SIP, interphase precipitation and matrix precipitation did not take place. The absence of matrix precipitation is not surprising given the low coiling temperature (510 °C) employed in this work. The kinetics of matrix precipitation become too sluggish below 600 °C. The absence of interphase precipitation is not surprising as well, as special conditions[13-18] are generally needed to promote interphase precipitation and there are not many reported observations of interphase precipitation in X70 steel. The most surprising result is the absence of SIP , in spite of the fact that finishing was carried out well below the NbC dissolution temperature. According to Thermo-Calc, NbC is a stable below 1150 °C. As a result, a large supersaturation is present at the finishing temperature.

The absence of SIP may be related to competition between the nucleation of NbC on dislcoations and the core-cap structure of NbC on pre-existing TiN particles [34-39]. As the temperature drops, below the dissolution temperature of NbC, a thermodynamic driving force for the precipitation of NbC will develop. A large supersaturation is needed to overcome the activation barrier for nucleation. Consequently, SIP is usually observed once the undercooling is at least 100 to 150 ˚C. The core-cap structure of NbC on pre-existing TiN particles does not require a large undercooling. As a result, shells/caps of NbC can easily form on pre-existing TiN particles at high temperatures as shown in **Figure 3-3** and **Figure 3-4**. This has the potential to deplete Nb from solid solution, making it more difficult for SIP to take place during finishing. To quantify this argument, simple calculations can be carried out to estimate the amount of NbC which precipitated epitaxially on pre-existing TiN particles. Using the TCFE12 database of thermocalc, the equlibrium (maximum) volume fraction of TiN at 900˚C is 0.000295. In comparison, the volume fraction of the large precipitates can be estimated as:

$$F_v = \frac{4}{3}\pi r^3 N \qquad \text{(Equation 3- 1)}$$

where r is the radius of the precipitates and N is the number density of the precipitates. Based on TEM observations, the average radius of the particles is 20-30 nm and the average number density is $2\times 10^{19}$ $m^{-3}$. The volume fraction of the large (Ti,Nb)(C,N) particles is therefore 0.00067 when the average radius of the particles is around 20 nm . This far exceeds the maximum possible volume fraction of TiN. If the difference in volume fractions is attributed to the formation of NbC shells/caps on the pre-existing TiN, then a

simple mass balance would lead one to conclude that only, 0.0525wt% Nb and 0.0375 wt% C remain in solid solution. This is just over half of the bulk Nb content of the alloy. It greatly reduces the driving force for strain induced precipitation during finishing. An estimate of the number density of strain-induced precipitates using the model of Zurob[40] leads to around $10^{18}$ $m^{-3}$. This very low number density is consistent with the absence of fine precipitates in the present work. Based on this analysis, it can be concluded that SIP precipitates are suppressed in the studied steel. Similar conclusions can also be obtained based on the value estimated for 3DAP data(0.012-0.033wt% Nb).

### 3.5.2 Microstructure heterogeneity and precipitates

**Table 3-3** summarizes the size and number density of (Ti,Nb)(C,N) particles in all four areas. It is evident that these precipitates are uniformly distributed within the microstructure (the difference of the particle size is acceptable since it is relatively small). This is not surprising given that TiN and NbC precipitation occur at high temperatures prior to austenite decomposition. As such, these particles should be uniformly distributed within the steel. Thus, it can be concluded the precipitates in the X70 were not responsible for the microstructure inhomogeneity shown in **Figure 3- 1**.

**Table 3-3. Comparison of the precipitates in different positions**

| | P1 | P2 | P3 | P4 |
|---|---|---|---|---|
| Precipitates number density/ $m^{-3}$ | $1x10^{19}$ | $1x10^{19}$ | $2x10^{19}$ | $2.5x10^{19}$ |

| | | | | |
|---|---|---|---|---|
| Precipitates average diameter size /nm | 50 ±21 | 60±30 | 57±33 | 40 ±21 |

Consequently, the dilatometry work as discussed in section 3.1 (**Figure 3-2**) indicates that the heterogeneity of the microstructure is related to austenite decomposition into PF ~ 700 °C and bainite below 550 °C. The structure observed had ferritic areas of low KAM and bainitic areas with higher KAM that is expected according to literature [23, 30, 31]. What is more, Nb segregation at dislocations is observed in the TEM and APT result (**Figure 3-5**). The segregation of Nb to dislocations is believed to retard static recovery and increase the strength of the steel [41, 42]. In the absence of fine NbC precipitates, solute Nb provide the main mechanism for limiting recovery and grain growth under the present processing conditions. Thus, the Nb segregation may also play a factor to the microstructure heterogeneity.

## 3.6 Conclusion

The spatial distribution of precipitates and microstructure heterogeneity in X70 steel were investigated using advanced characterization techniques in this paper. Firstly, core-cap structure precipitates (30-70 nm in diameter) were observed by TEM in the studied steel. The core was rich in Ti and N, while the cap typically contained Nb and C. SIP of fine (2-10 nm) NbC particles on dislocations was not observed. The absence of SIP is believed to be due to the depletion of Nb from solid solution because of the core-cap structure of NbC on pre-existing TiN particles. Secondly, (Ti, Nb) (C, N) is distributed uniformly in the

studied steel because of the homogeneous distribution of TiN prior to hot rolling. The precipitate number density in the different regions is all about $10^{19}$ $m^{-3}$. This indicates that variations of grain size and KAM within the microstructure were not correlated with variations in the distribution of microalloyed precipitates. Lastly, this study also provides a relatively new workflow to investigate the precipitates within the steel, especially in site-specific areas. It was demonstrated that the precipitate distribution was not responsible for the heterogeneity of the microstructure in this steel.

## 3.7 Acknowledgements

The authors would like to acknowledge the sponsorships from EVRAZ North America steel corporations through an NSERC CRD Grant. The authors are grateful to Dr. Fateh Fazeli and CanmetMATERIALS (Hamilton, Canada) for casting and hot rolling the material. The characterization work was carried out at the Canadian Centre for Electron Microscopy, a national facility supported by the Canada Foundation for Innovation under the Major Science Initiative program, NSERC and McMaster University.

## 3.8 Supplementary Data

Examples of core-cap structure/ epitaxial growth precipitates are shown in Figure 3-7(a-c). The core was rich in Ti and N, while the cap typically contained Nb and C. The C is almost everywhere due to the limitation of EDS detection and contamination of the samples.

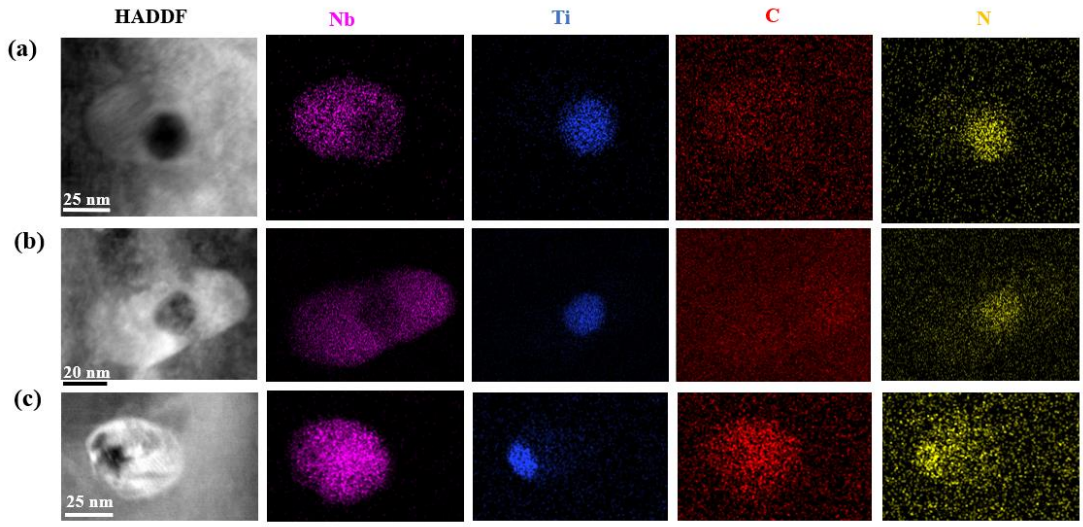


**Figure 3-7: STEM-HADDF and EDS (distribution of Nb, Ti, C and N) images of TiN-NbC composite precipitates observed in X70, showing core-cap structure of NbC on pre-existing TiN.**

## 3.9 References

[1] T. Gladman, The physical metallurgy of microalloyed steels, Maney Pub1997.

[2] A. Davenport, L. Brossard, R. Miner, Precipitation in microalloyed high-strength low-alloy steels, JOM 27(6) (1975) 21-27.

[3] M. Charleux, W. Poole, M. Militzer, A. Deschamps, Precipitation behavior and its effect on strengthening of an HSLA-Nb/Ti steel, Metallurgical and Materials Transactions A 32 (2001) 1635-1647.

[4] D. Belato Rosado, W. De Waele, D. Vanderschueren, S. Hertelé, Latest developments in mechanical properties and metallurgical features of high strength line pipe steels, 5th International Conference on Sustainable Construction and Design, Ghent University, Laboratory Soete, 2013.

[5] V.M.H. KONSTRUKCIJSKA, High-strength low-alloy (HSLA) steels, Materiali in tehnologije 45(4) (2011) 295-301.

[6] H.J. Kong, C.T. Liu, A review on nano-scale precipitation in steels, Technologies 6(1) (2018) 36.

[7] C. Klinkenberg, K. Hulka, W. Bleck, Niobium carbide precipitation in microalloyed steel, steel research international 75(11) (2004) 744-752.

[8] S. Liang, X. Wang, H.S. Zurob, NbC precipitation during multi-pass deformation of a nickel-based model alloy: Experiments and modelling, Materials Science and Engineering: A 772 (2020) 138748.

[9] S. Liang, X. Wang, C. Andrei, H.S. Zurob, NbC precipitation during two-pass hot deformation of a nickel-based model alloy at 700° C: Experiments and modelling, Materials Science and Engineering: A 802 (2021) 140447.

[10] B. Dutta, E.J. Palmiere, C.M. Sellars, Modelling the kinetics of strain induced precipitation in Nb microalloyed steels, Acta materialia 49(5) (2001) 785-794.

[11] P. Gong, E.J. Palmiere, W.M. Rainforth, Characterisation of strain-induced precipitation behaviour in microalloyed steels during thermomechanical controlled processing, Materials Characterization 124 (2017) 83-89.

[12] D. Poddar, P. Cizek, H. Beladi, P.D. Hodgson, Evolution of strain-induced precipitates in a model austenitic Fe–30Ni–Nb steel and their effect on the flow behaviour, Acta materialia 80 (2014) 1-15.

[13] H. Dong, H. Chen, W. Wang, Y. Zhang, G. Miyamoto, T. Furuhara, C. Zhang, Z. Yang, S. van der Zwaag, Analysis of the interaction between moving α/γ interfaces and interphase precipitated carbides during cyclic phase transformations in a Nb-containing Fe-C-Mn alloy, Acta Materialia 158 (2018) 167-179.

[14] S. Clark, V. Janik, A. Rijkenberg, S. Sridhar, Analysis of the extent of interphase precipitation in V-HSLA steels through in-situ characterization of the γ/α transformation, Materials Characterization 115 (2016) 83-89.

[15] A. Davenport, F. Berry, R. Honeycombe, Interphase precipitation in iron alloys, Metal Science Journal 2(1) (1968) 104-106.

[16] R. Okamoto, A. Borgenstam, J. Ågren, Interphase precipitation in niobium-microalloyed steels, Acta Materialia 58(14) (2010) 4783-4790.

[17] H.-J. Kestenbach, S. Campos, E. Morales, Role of interphase precipitation in microalloyed hot strip steels, Materials science and technology 22(6) (2006) 615-626.

[18] F. Bu, X. Wang, S. Yang, C. Shang, R. Misra, Contribution of interphase precipitation on yield strength in thermomechanically simulated Ti–Nb and Ti–Nb–Mo microalloyed steels, Materials Science and Engineering: A 620 (2015) 22-29.

[19] V. Challa, W. Zhou, R. Misra, R. O'Malley, S. Jansto, The effect of coiling temperature on the microstructure and mechanical properties of a niobium–titanium microalloyed steel processed via thin slab casting, Materials Science and Engineering: A 595 (2014) 143-153.

[20] Z. Jia, R. Misra, R. O'malley, S. Jansto, Fine-scale precipitation and mechanical properties of thin slab processed titanium–niobium bearing high strength steels, Materials Science and Engineering: A 528(22-23) (2011) 7077-7083.

[21] J. Omale, E. Ohaeri, J. Szpunar, M. Arafin, F. Fateh, Microstructure and texture evolution in warm rolled API 5L X70 pipeline steel for sour service application, Materials Characterization 147 (2019) 453-463.

[22] J. Omale, E. Ohaeri, A. Tiamiyu, M. Eskandari, K. Mostafijur, J. Szpunar, Microstructure, texture evolution and mechanical properties of X70 pipeline steel after different thermomechanical treatments, Materials Science and Engineering: A 703 (2017) 477-485.

[23] S.-I. Lee, S.-Y. Lee, S.G. Lee, H.G. Jung, B. Hwang, Effect of strain aging on tensile behavior and properties of API X60, X70, and X80 pipeline steels, Metals and Materials International 24 (2018) 1221-1231.

[24] L.-H. Lee, C.-H. Yu, C.-Y. Wei, P.-C. Lee, J.-S. Huang, C.-Y. Wen, Plan-view transmission electron microscopy specimen preparation for atomic layer materials using a focused ion beam approach, Ultramicroscopy 197 (2019) 95-99.

[25] C. Li, G. Habler, L.C. Baldwin, R. Abart, An improved FIB sample preparation technique for site-specific plan-view specimens: A new cutting geometry, Ultramicroscopy 184 (2018) 310-317.

[26] T. Malis, S. Cheng, R. Egerton, EELS log-ratio technique for specimen-thickness measurement in the TEM, Journal of electron microscopy technique 8(2) (1988) 193-200.

[27] K. Thompson, D. Lawrence, D. Larson, J. Olson, T. Kelly, B. Gorman, In situ site-specific specimen preparation for atom probe tomography, Ultramicroscopy 107(2-3) (2007) 131-139.

[28] M.K. Miller, Atom probe tomography: analysis at the atomic level, Springer Science & Business Media2012.

[29] B. Gault, M.P. Moody, J.M. Cairney, S.P. Ringer, Atom probe microscopy, Springer Science & Business Media2012.

[30] S. Zaefferer, P. Romano, F. Friedel, EBSD as a tool to identify and quantify bainite and ferrite in low-alloyed Al-TRIP steels, Journal of microscopy 230(3) (2008) 499-508.

[31] Y.-W. Chen, Y.-T. Tsai, P.-Y. Tung, S.-P. Tsai, C.-Y. Chen, S.-H. Wang, J.-R. Yang, Phase quantification in low carbon Nb-Mo bearing steel by electron backscatter diffraction technique coupled with kernel average misorientation, Materials Characterization 139 (2018) 49-58.

[32] H. Hu, H.S. Zurob, G. Xu, D. Embury, G.R. Purdy, New insights to the effects of ausforming on the bainitic transformation, Materials Science and Engineering: A 626 (2015) 34-40.

[33] W. Bleck, E. Ratte, Fundamentals of Cold Formable HSLA Steels, International Symposium on Niobium Microalloyed Sheet Steel for Automotive Application, S. Hashimoto, S. Jansto, H. Mohrbacher, F. Siciliano, Eds. TMS (The Minerals, Metals & Materials Society), 2006, pp. 551-564.

[34] X. Ma, C. Miao, B. Langelier, S. Subramanian, Suppression of strain-induced precipitation of NbC by epitaxial growth of NbC on pre-existing TiN in Nb-Ti microalloyed steel, Materials & Design 132 (2017) 244-249.

[35] A. Craven, K. He, L. Garvie, T. Baker, Complex heterogeneous precipitation in titanium–niobium microalloyed Al-killed HSLA steels—I.(Ti, Nb)(C, N) particles, Acta Materialia 48(15) (2000) 3857-3868.

[36] S. Hong, K. Kang, C. Park, Strain-induced precipitation of NbC in Nb and Nb–Ti microalloyed HSLA steels, Scripta materialia 46(2) (2002) 163-168.

[37] M. Leap, E. Brown, Crystallography of duplex AlN–Nb (C, N) precipitates in 0.2% C steel, Scripta materialia 47(12) (2002) 793-797.

[38] Z. Chen, M. Loretto, R. Cochrane, Nature of large precipitates in titanium-containing HSLA steels, Materials Science and Technology 3(10) (1987) 836-844.

[39] M. Grujicic, I. Wang, W. Owen, On the formation of duplex precipitate phases in an ultra-low carbon microalloyed steel, Calphad 12(3) (1988) 261-275.

[40] H. Zurob, C. Hutchinson, Y. Brechet, G. Purdy, Modeling recrystallization of microalloyed austenite: effect of coupling recovery, precipitation and recrystallization, Acta materialia 50(12) (2002) 3077-3094.

[41] X. Li, P. Wu, R. Yang, S. Zhao, S. Zhang, S. Chen, X. Cao, X. Wang, Nb segregation at prior austenite grain boundaries and defects in high strength low alloy steel during cooling, Materials & Design 115 (2017) 165-169.

[42] Q. Yu, Z. Wang, X. Liu, G. Wang, Effect of microcontent Nb in solution on the strength of low carbon steels, Materials Science and Engineering: A 379(1-2) (2004) 384-390.

# Chapter 4 Evolution of the Microstructure and Mechanical Properties of a V-Containing Microalloyed Steel During Coiling

This chapter is reproduced from accepted journal publications: *Gu, Chen, Colin Scott, Fateh Fazeli, Michael J. Gaudet, Jing Su, Xiang Wang, Nabil Bassim, and Hatem Zurob. "Evolution of the microstructure and mechanical properties of a V-containing microalloyed steel during coiling." Materials Science and Engineering: A (2023): 145332.".* This chapter also includes some minor updating based on the suggestion from the committee during defence. The author of this thesis is the first author and the main contributor of this publication, including conceiving the initial ideas, development of approach and methodology, carrying out experiments, analysis of data, and preparation of the manuscript.

## 4.1 Abstract

The microstructural evolution during coiling and its effects on the mechanical properties of a vanadium microalloyed steel were investigated. Samples were held at 500 ºC for 80 s (S1), 600 s (S2), 3600 s (S3), and 18000 s (S4) to capture the various stages of microstructure evolution. Experimental results demonstrated that nano precipitates (<10

nm) nucleated during holding at 500 ºC were heterogeneously distributed. These precipitates mainly contained V and N and were more commonly found in areas with a high value of the Kernel Average Misorientation (KAM) because these areas have a larger number of dislocations that act as nucleation sites for the precipitates. The tensile flow curves of the samples show extended elastoplastic regions that are related to the heterogeneity of the microstructure as well as the presence of microscopic residual stresses. The precipitation strengthening effect is not very large and is offset by softening which is caused by the aging of bainite and the associated recovery of dislocations.

**Keywords: HSLA, coiling, precipitate, site-specific, mechanical properties.**

## 4.2 Introduction

Due to their high strength, low ductile-to-brittle transition temperature, good weldability and low cost, microalloyed HSLA steels are utilized in a wide range of components in the oil, gas and automobile industries[1-5]. Microalloyed steels are strengthened by a combination of grain refinement, solid solution hardening, dislocation hardening and precipitation hardening. Fine/nanoscale carbonitrides of microalloying elements such as Nb, Ti and V play a significant role in the strengthening of these steels [6, 7].

Microalloyed precipitates in HSLA are commonly classified as strain-induced precipitates (SIP), interphase precipitates (IP) and matrix precipitates [1-8] Strain-induced precipitates nucleate on dislocations during finish rolling within the temperature range of 1000-750 ºC. The particle size of these precipitates is usually around 10 nm [9-13]. Interphase

Precipitates form on the austenite (γ) / ferrite (α) interface during the phase transformation when the cooling rate is in the range of 20-50 ºC /s. These precipitates are usually aligned in finely spaced rows. The particle size of these precipitates is usually 5-10 nm [14-17]. Precipitates that form in ferrite or bainitic ferrite during the coiling process are commonly referred to as matrix precipitates. Matrix precipitates are usually extremely fine, leading to a significant precipitation hardening contribution [18-21].

In addition to the above precipitates, many researchers have reported the presence of solute "clusters" within the microstructure][7, 20, 22]. These clusters could be described as regions of the matrix which contain a high concentration of solute atoms. In contrast to precipitates, clusters do not have a crystal structure which is distinct from that of the matrix, and they are not separated from the matrix by a sharp interface. Clusters are usually observed at short holding times, while precipitates dominate at longer times. Some researchers have suggested that the clusters aid the nucleation of precipitates, but detailed evidence is lacking. It is also reported that solute clusters are highly potent strengthening agents [6, 7, 20, 21] and consequently many studies have been carried out to understand their evolution in aluminum alloys and precipitation hardenable steels [22-25]. In contrast, there are very few studies on cluster formation during the coiling of microalloyed steels. The studies that exist, are not site-specific, meaning that measurements of clusters/precipitates could not be tracked within individual features of the microstructure (e.g. clusters within allotriomorphic ferrite vs. bainitic ferrite). In addition, the effect of

clusters and fine precipitates on the evolution of mechanical properties during coiling has not been discussed in detail.

In this work, the evolution of microstructure and mechanical properties was studied in a vanadium-containing steel as a function of the coiling time. Samples were held at 500 ºC for 80 s (S1), 600 s (S2), 3600 s (S3) and 18000 s (S4). The evolution of precipitation in areas with high and low values of Kernel Average Misorientation (KAM) was analyzed in detail using advanced characterization techniques. Samples for Transmission Electron Microscopy (TEM) were prepared by the plane view lift-out method in a Plasma Focused Ion Beam (PFIB) to select the specific area chosen based on Electron Backscatter Diffraction (EBSD) maps. Then, Energy Dispersive Spectroscopy (EDS), Electron Energy Loss Spectroscopy (EELS) in the TEM and 3D atom probe tomography (APT) were used to conduct a detailed analysis of the precipitates in these different areas. The corresponding mechanical properties were measured in order to elucidate the structure-properties relationships in this steel.

## 4.3 Materials and methods

The material used in the present study is a V-microalloyed steel (0.056C-0.28Si-2.00Mn-0.044Al-0.0009Ti-0.11V-0.0039N wt%), which is supplied by CanmetMATERIALS in the form of 1 mm cold-rolled sheet. A simplified heat-treatment was designed to follow precipitation kinetics at low coiling temperatures. The studied material was solutionized

for 5 minutes at 1050 ºC (above the dissolution temperature of V (C, N), which is around 806 ºC) and then cooled to 500 ºC (above the Ms temperature to avoid martensite formation) at a cooling rate of 30 ºC /s (the highest cooling rate in CLSM). The steel was held at 500 ºC for different times to simulate the coiling process. Heat treatment of the studied material was carried out using the hot stage of a high-temperature confocal laser scanning microscope (CLSM, LasertecVL2000DX) which also allowed in-situ observation of the transformation and direct determination of the prior austenite grain size. The specimens used for this part of the study had dimensions of 4mm × 3.6mm ×1mm (RD×TD×ND). A vacuum around -$10^{-5}$ Pa was maintained during the isothermal treatment. Ar gas was used for quenching. S1 was held for 80 s, S2 was held for 600 s, S3 was held for 3600 s, and S4 was held for 18000 s, as shown in **Figure 4- 1**.

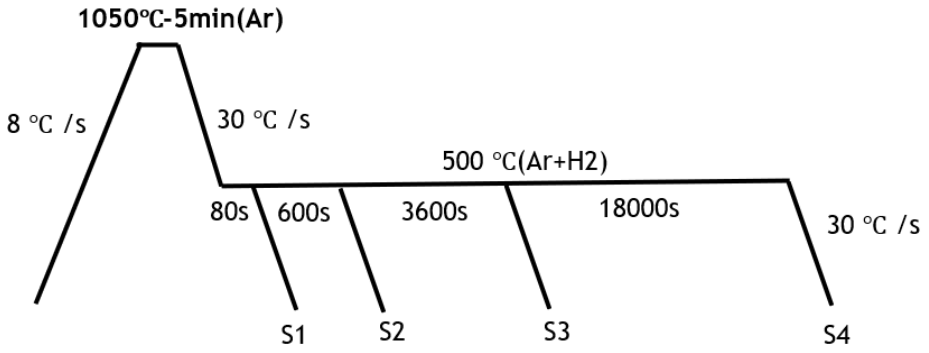


**Figure 4- 1. Experiment design for V-containing microalloyed steel. (S1: sample held at 500 ºC for 80 s. S2: sample held at 500 ºC for 600 s. S3: sample held at 500 ºC for 3600 s. S4: sample held at 500 ºC for 18000 s.)**

After the heat treatment, the 4 samples were analyzed by EBSD. KAM maps were used to identify the desired areas for site-specific precipitate/cluster analysis. The workflow of the site-specific analysis in this study is shown in **Figure 4- 2**. All EBSD analyses were performed using a JEOL JSM-7000F SEM equipped with a Nordlys II EBSD Camera. The EBSD data was then processed using the HKL Channel 5 software.

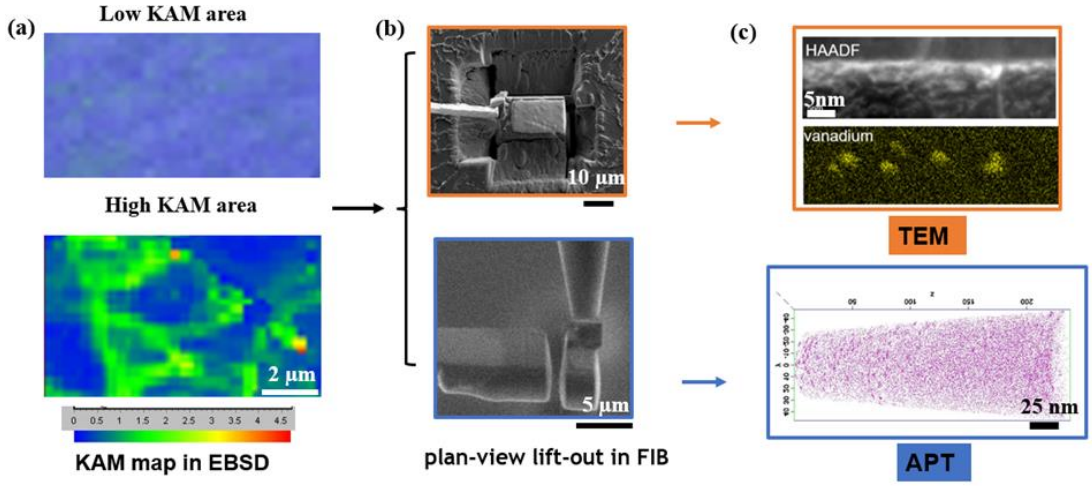


**Figure 4- 2. Site-specific analysis workflow:(a) area selecting in EBSD according to KAM maps;(b) sample preparation in FIB; (c) characterization in TEM and APT.**

After EBSD analysis, TEM samples from low KAM and high KAM areas were extracted using site-specific FIB milling, as shown in **Figure 4- 2**b. The regions of interest were extracted by the plane view lift-out method [26, 27] in a Thermo Fisher Scientific Helios G4 UXe Dual-Beam PFIB microscope. The samples were then imaged in a Thermo Fisher Scientific Talos 200X TEM equipped with four in-column silicon drift EDX (SDD) Super-

X detectors in Scanning TEM (STEM) mode. The composition, morphology, and distribution of the particles were measured using EDS and EELS.

APT tips from the low KAM and high KAM areas were lifted out of the S3 sample using the PFIB using the standard procedure described in [28]. A Cameca local electrode atom probe (LEAP) 4000X HR was used for APT experiments at a base temperature of 59.7 K in laser pulsing mode ($\lambda$ = 355 nm), with a pulse rate of 250 kHz, a pulse energy in the range of 50–60 pJ and a targeted detection rate of 0.01 ions/pulse (1 %). Reconstruction and analysis of the APT data were performed using the IVAS 3.6.8 software and established reconstruction protocols [29, 30]. Reconstructions were spatially calibrated using known spacings of crystal planes.

In addition, rectangular samples with dimensions of 4 mm×10 mm×1 mm (RD×TD×ND) were machined from the as-received material by Electrical Discharge Machining (EDM) for further study of the phase transformations using a BAHR DIL 805 dilatometer. The heat treatment in the dilatometer is the same as the heat treatment of S2 in **Figure 4- 1**.

The evolution of the mechanical properties was measured using ASTM E8/E8M sub-size tensile samples. The solution treatment was carried out in a tube furnace under Ar gas (1050ºC-5min) and the aging step was carried out in a salt bath (500ºC). The samples were tested on an MTS 370 Landmark 100 kN frame with an Instron 2620-604 25 mm extensometer. The strain rate was $2x10^{-3}$/s.

## 4.4 Results

### 4.4.1 Microstructure characterization

#### *4.4.1.1 Phases transformation*

The microstructure and dilatometric curve of the samples held at 500 ºC for 80 s (S1) and 3600 s (S3) are shown in **Figure 4- 3** (a) and (b), respectively. The optical microscope (OM) image of S1 shows that it mainly consists of bainite and ferrite (**Figure 4- 3**a). The thermal dilatometric curve of S3 shows that the bulk of the phase transformations took place during cooling below 700 ºC, before the isothermal section. Some transformation continued to take place during isothermal holding at 500 ºC, but as shown in the insert, the transformation was largely complete after ~10 s of holding at 500 ºC.

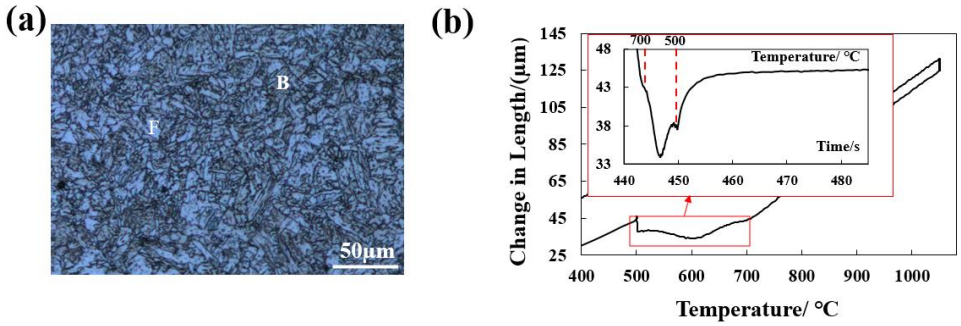


**Figure 4- 3. (a) Optical micrograph of S1 (B-bainite, F-ferrite). (b) The thermal dilatometric curve of S3, inset shows a dilatometric-time curve at the isothermal hold of 500 °C.**

Optical metallography (supplementary material) and EBSD maps (**Figure 4- 4**) show that the microstructure does not significantly change during the first 600 seconds of isothermal holding. After 18000 s of holding at 500 °C, however, the microstructure appears to become coarser, and the fine bainitic ferrite laths begin to disappear in many regions. Similar observations have been reported in other bainitic steels. Siame et al. [31, 32] referred to this change as the "granularization" of bainite. It refers to the replacement of lath bainitic structures with more granular aggregates of ferrite and cementite.

**Figure 4- 4** shows the EBSD grain boundary maps and corresponding KAM maps (inserted) for the areas from which the samples were extracted. The yellow frame shows the high KAM region, while the blue frame shows the low KAM region. The KAM map is constructed based on the average misorientation angle of a given point with respect to all of its neighbors [33, 34]. It can be used to estimate the density of geometrically necessary dislocations (GND) and assess the local transformation strain developed in the steel. In the present study, the samples did not undergo any deformation and the measured misorientations are attributed solely to the phase transformations taking place during austenite decomposition. It is reported that low-temperature transformation microstructures such as acicular ferrite(AF), and bainitic ferrite(BF) contain a higher density of GNDs compared to reconstructive transformation products such as polygonal ferrite (PF)[33]. Thus, the low KAM areas could be identified as PF that formed at high temperatures (~700

ºC), while the high KAM areas are BF that formed at lower temperatures during cooling or isothermal holding [35-37].

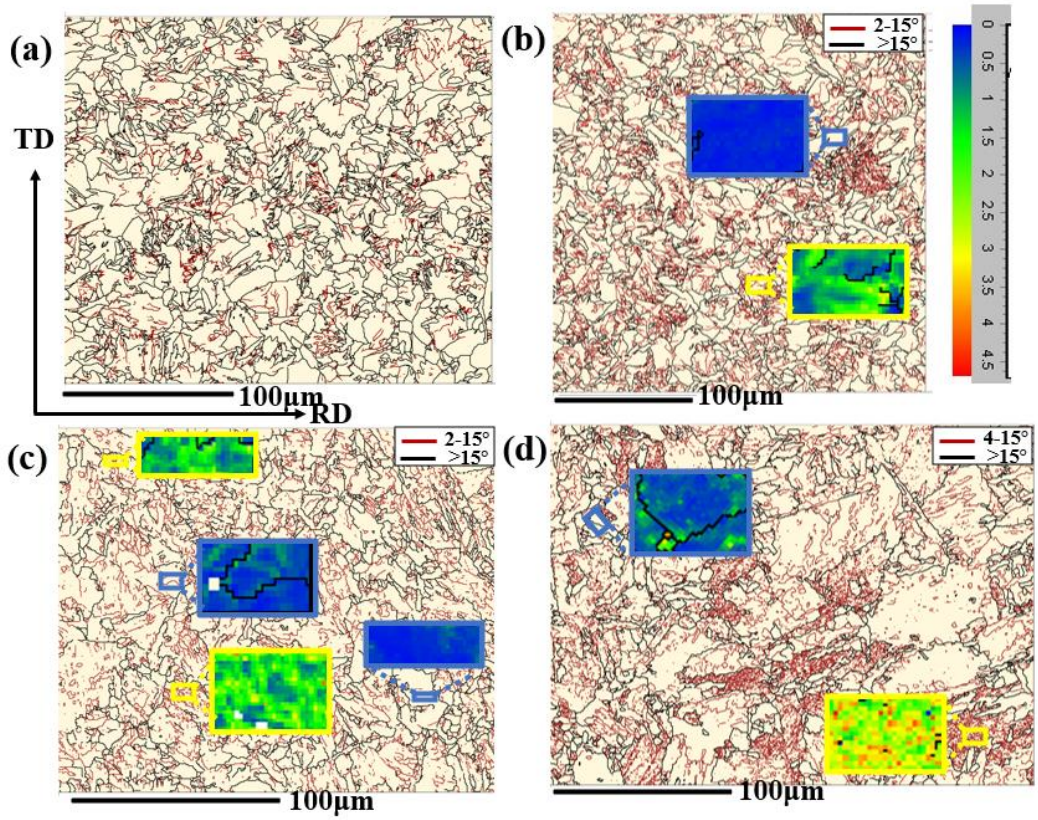


**Figure 4- 4. EBSD grain boundary maps and corresponding KAM maps (inserted) in the selected area of (a) S1; (b) S2;(c) S3;(d) S4 (4-15º grain boundary is selected for S4 to avoid the artifact introduced by sample preparation, like scratches). (Yellow frame and blue frame in the figures are the high KAM and low KAM areas chosen for subsequent TEM and APT analysis)**

#### *4.4.1.2 Precipitate characterization*

***(1) TEM***

Large precipitates (>20nm)

TEM samples lifted from low KAM and high KAM areas by PFIB were used to further characterize precipitation after different holding times. Precipitates larger than 20 nm are found in all the samples and are distributed homogenously in all areas. **Figure 4- 5** shows a typical large precipitate. The structure of these particles is complex. At the core, there is an AlN particle with Mn and S segregation at the particle/matrix interface. Two smaller Ti (C, N) caps appear to have formed on the AlN particle. The Ti(C, N) caps also contain V, but it is not clear if the Ti and V are mixed or if a VN shell has formed on top of the Ti(C, N) cap. It is worth mentioning that, at equilibrium, some AlN and MnS would remain undissolved at 1050 ºC, according to ThermoCalc calculations. Thus, the AlN and MnS observed in the samples could be precipitates formed at high temperatures and not redissolved during the solution heat treatment used in this work.

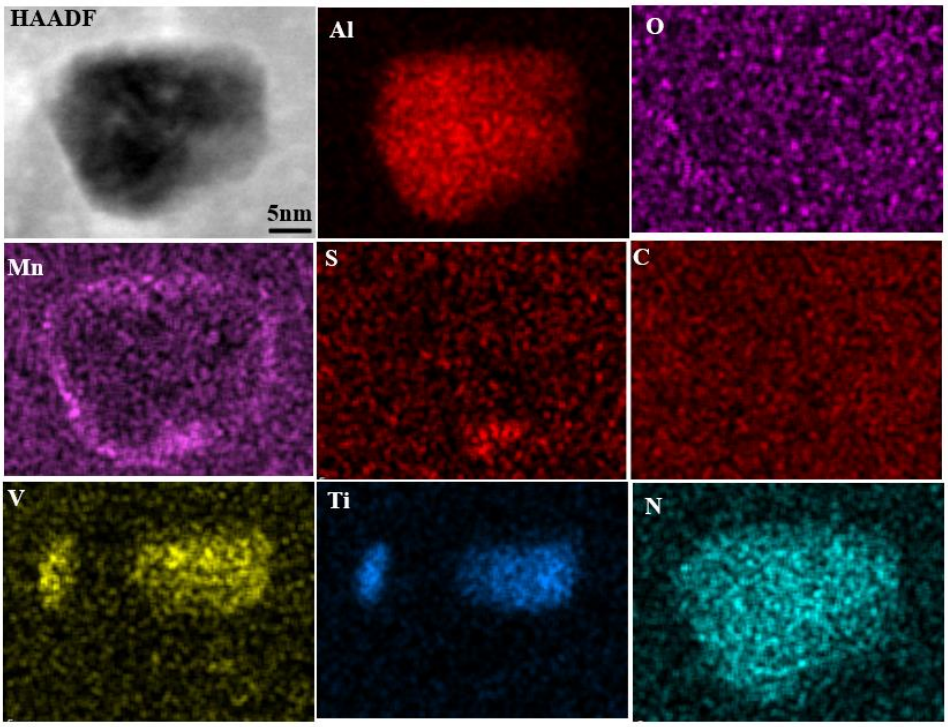


**Figure 4- 5. EDS mapping of the homogenous distributed large precipitates present for all conditions.**

### Nano-precipitates(<10nm)

Fine nanoscale precipitates (<10 nm) were not found in the low KAM area of sample S1, after holding at 500 ºC for 80 s. In contrast, a small number of nano precipitates which mainly contain V and N (as shown by the arrows in the V and N EELS maps of **Figure 4-6**) were found in the high KAM area for the same holding time. The particle size of these precipitates was around 2-3 nm. One of the observation areas with nano precipitates is shown in **Figure 4- 6**. The VN precipitates are distributed around the boundary of a region that shows the segregation of Mn and C. The boundary could be inter-lath retained austenite.

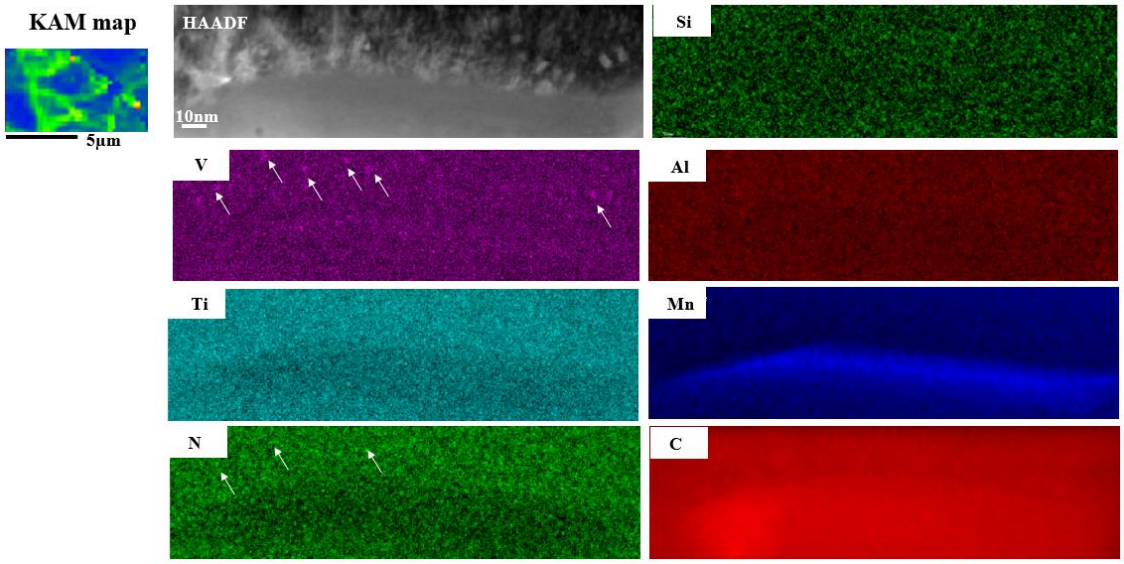


**Figure 4- 6. EELS mapping of the nano precipitates in the high KAM area of S1.**

Similarly, nano-precipitates were not found in the low KAM area in S2 (600 s). More nano precipitates with particle sizes around 3-4 nm were observed in the high KAM area after 600 s of holding. Again, most of these precipitates contain V and N. As shown in region 1 of **Figure 4- 7**, some of the precipitates may also contain Mn, which can substitute for V in VN, as shown in region 2 of **Figure 4- 7**. The precipitates appear near a region with high Mn and C content, as shown in region 1 of **Figure 4- 7**. This region is Si-depleted, suggesting that this region could be a cementite particle.

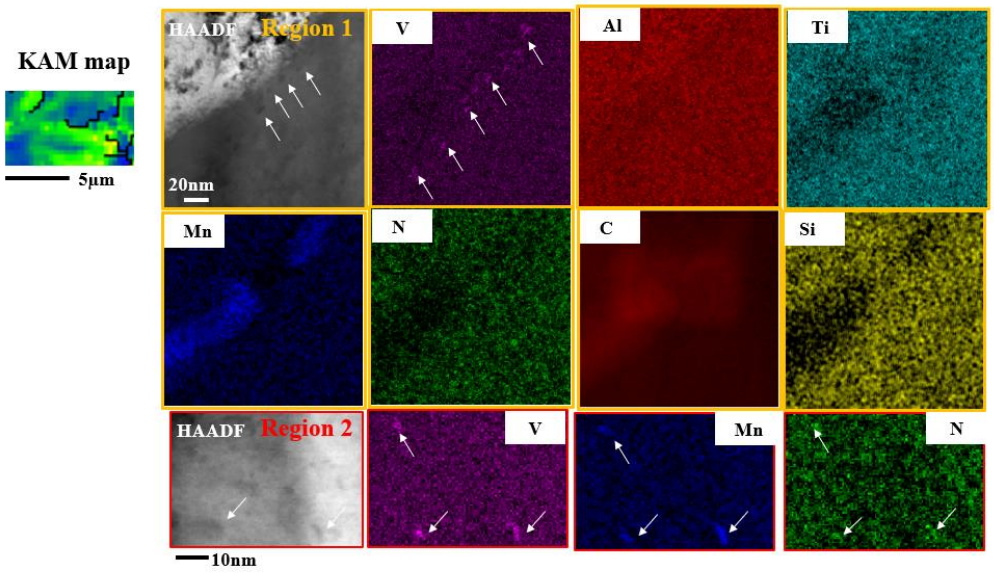


**Figure 4- 7. EELS mapping of the nano precipitates in the large KAM area of S2.**

When the holding time was increased to 3600 s, more nano precipitates with a mean particle size of 4-5 nm were found within the high KAM area. **Figure 4- 8** shows the precipitates in one of the high KAM areas in sample S3. These precipitates contain primarily V and N. Some Al and Mn could also be present within the precipitates or at the precipitate/matrix interface. In the low KAM area, the segregation/clustering of V (as shown by the circle in the V map in **Figure 4- 9**) is also observed.

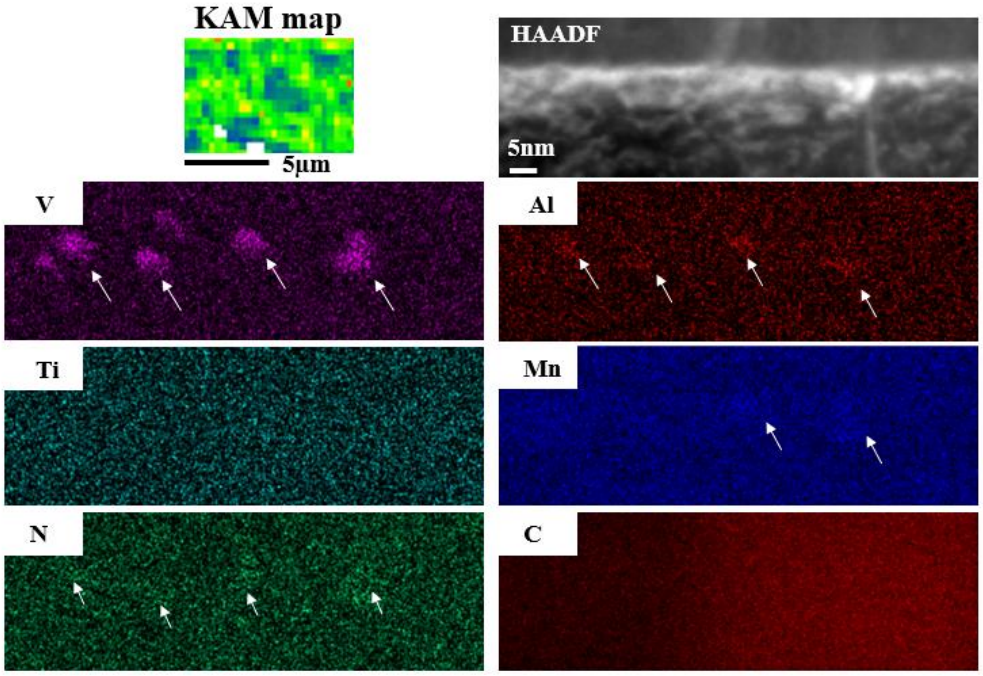


**Figure 4- 8. EDS mapping of the nano precipitates in the high KAM area of S3**

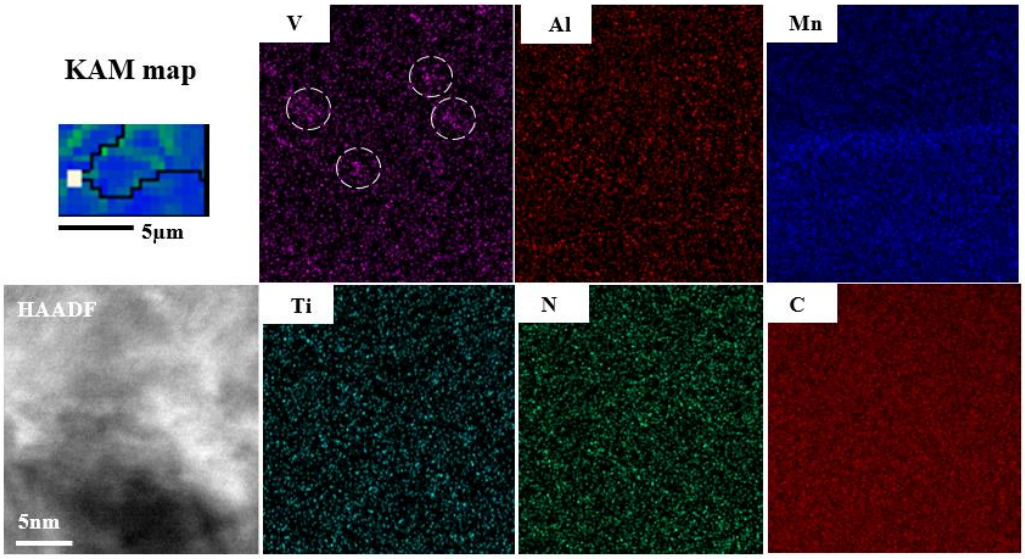


**Figure 4- 9. EDS mapping of the clusters in the low KAM area of S3**

After isothermal holding for 18000 s, TEM characterization revealed that there is no significant difference in terms of the precipitate distribution between low KAM and high KAM areas. V-containing precipitates (5-7 nm) are present in both high KAM (**Figure 4-10**) and low KAM areas (**Figure 4- 11**). Most of the precipitates contain V, N, and Al, and some of them may also contain Mn.

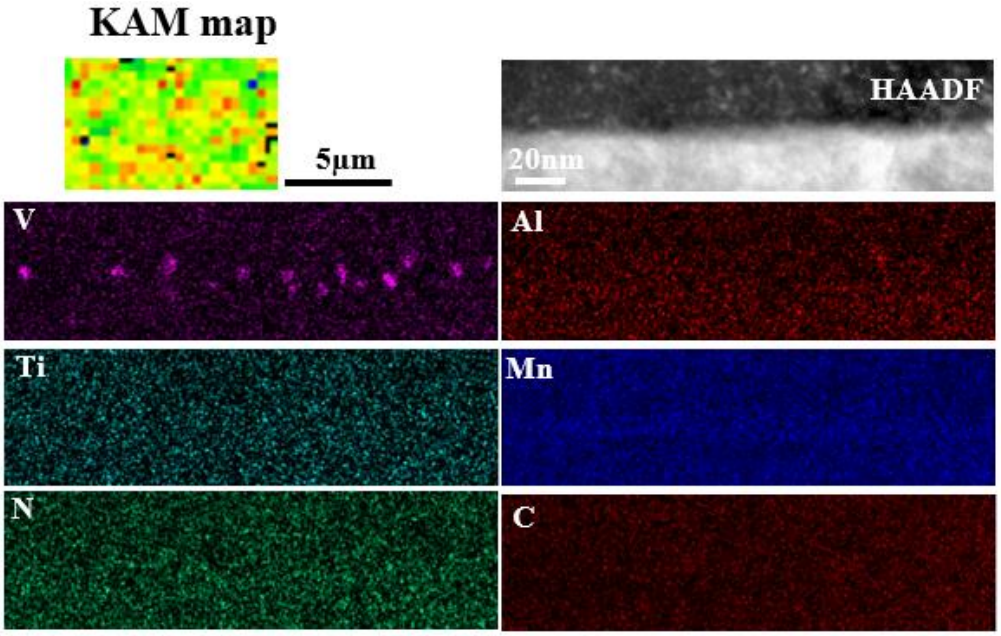


**Figure 4- 10. EDS mapping of the nano precipitates in the high KAM area of S4.**

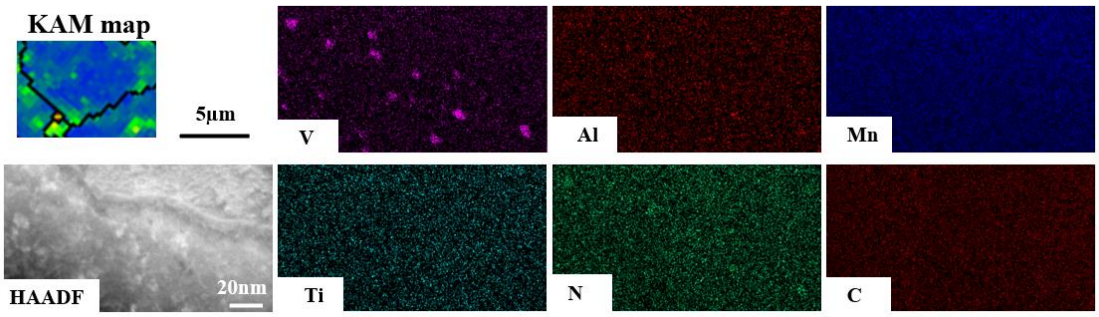


**Figure 4- 11. EDS mapping of the nano precipitates in the low KAM area of S4.**

***(2) APT***

In order to investigate the possible presence of solute clusters, APT tips were prepared from both the low and high KAM areas of sample S3. 3D atomic maps of V+VN ions in S3 are shown in **Figure 4- 12**(a) for the high KAM area and **Figure 4- 12**(b) for the low KAM area. The APT data confirms earlier TEM observations. The high KAM area (**Figure 4-12**. a) contains 3-5 nm regions which are rich in V and VN ions and could be identified as the VN precipitates observed in the TEM. In contrast, the low KAM area shows a large number of small regions that are enriched in V and N, as shown in ROI-2 of **Figure 4- 12**. (b) . These volumes still contain fewer V ions and have a very irregular shape. They may best be described as clusters of V and N within the matrix.

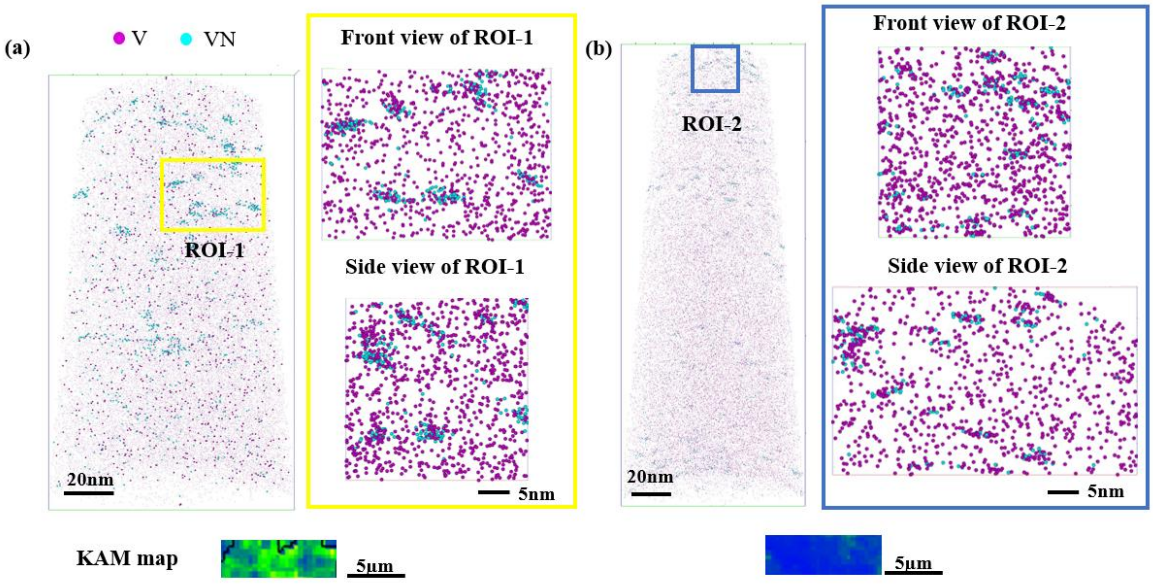


**Figure 4- 12. APT reconstructions from sample S3: 3D atomic map of V+VN ions in (a) high KAM area, (b) low KAM area.**

### 4.4.2 Mechanical properties

The engineering stress-strain curves for all 4 conditions are plotted in **Figure 4- 13** and key mechanical properties are summarized in **Table 4- 1**. The tensile results show a gradual change in the yielding behavior as a function of aging time. For the sample held at 500 ºC for 80 s, an extended elastoplastic transition is observed. With increasing aging time, the elastoplastic transition takes place over a narrower strain range. Using the 0.1% offset yield stress, an increase of the yield stress is observed with increasing aging time. Interestingly, however, the UTS appears to decrease with increasing aging time. Sample S1 (80 s) has

the highest UTS value of ~ 654 MPa while S4 (18,000 s) has the lowest UTS value of ~618 MPa.

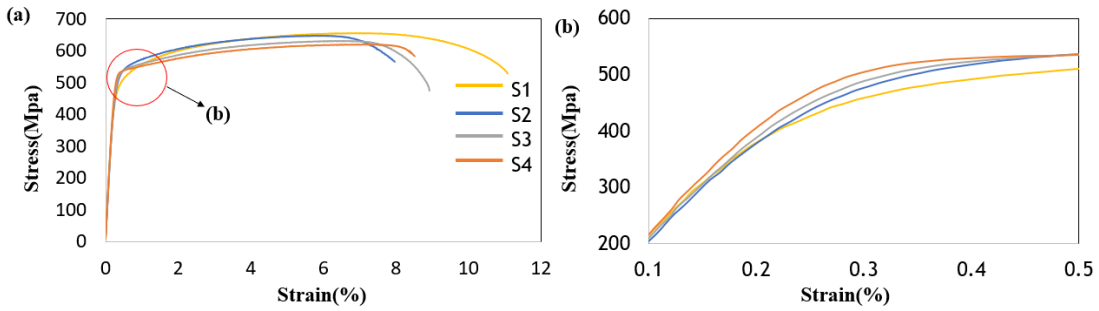


**Figure 4- 13. Engineering stress-strain cure of S1, S2, S3 and S4. (a) Strain changes from 0-12%; (b) Strain changes from 0.1-0.5%. (Only one sample was tested for each condition and therefore error bars were not added).**

**Table 4- 1. Summary of mechanical properties of S1, S2, S3 and S4.**

| Sample | YS (0.1% offset) | UTS |
|---|---|---|
| **S1** | 474 | 654 |
| **S2** | 502 | 645 |
| **S3** | 513 | 629 |
| **S4** | 525 | 618 |

## 4.5 Discussion

### 4.2.1 Microstructure evolution during coiling

Based on the dilatometry data, most of the phase transformation occurred during cooling from 700ºC to 500ºC. The transformation appears to be complete after the first 10 s of isothermal holding at 500 ºC. The volume fraction of ferrite and bainite should, therefore, be similar for all four holding times. TEM observation made it possible to follow precipitate evolution within ferrite (low KAM areas) and bainitic ferrite (high KAM areas) as a function of time.

As mentioned before, microalloyed precipitates in HSLA steel are commonly classified as strain-induced precipitates (SIP), interphase precipitates or matrix precipitates [1-8]. In this work, some large AlN precipitates (> 20 nm) were observed. Ti and V-rich caps were observed on most of these precipitates. The precipitates were distributed homogenously within both the low and high KAM areas, which suggests that these precipitates formed at high temperatures. The ThermoCalc calculations suggest that AlN and MnS are not completely dissolved at the solution temperature (1050 ºC) used in this study. Thus, the AlN and MnS observed in the samples could be undissolved precipitates formed within austenite (i.e. prior to the phase transformation) during prior thermomechanical processing. These high-temperature AlN/MnS precipitates serve as nucleation sites for Ti(C, N)/VN. Overall, the AlN and MnS observed in these samples existed/formed prior to phase transformation, and they are distributed homogenously in all the samples. In contrast, the

fine precipitates (< 10 nm) observed in the 4 samples formed heterogeneously during isothermal holding at 500 ºC. These precipitates are a kind of matrix precipitates.

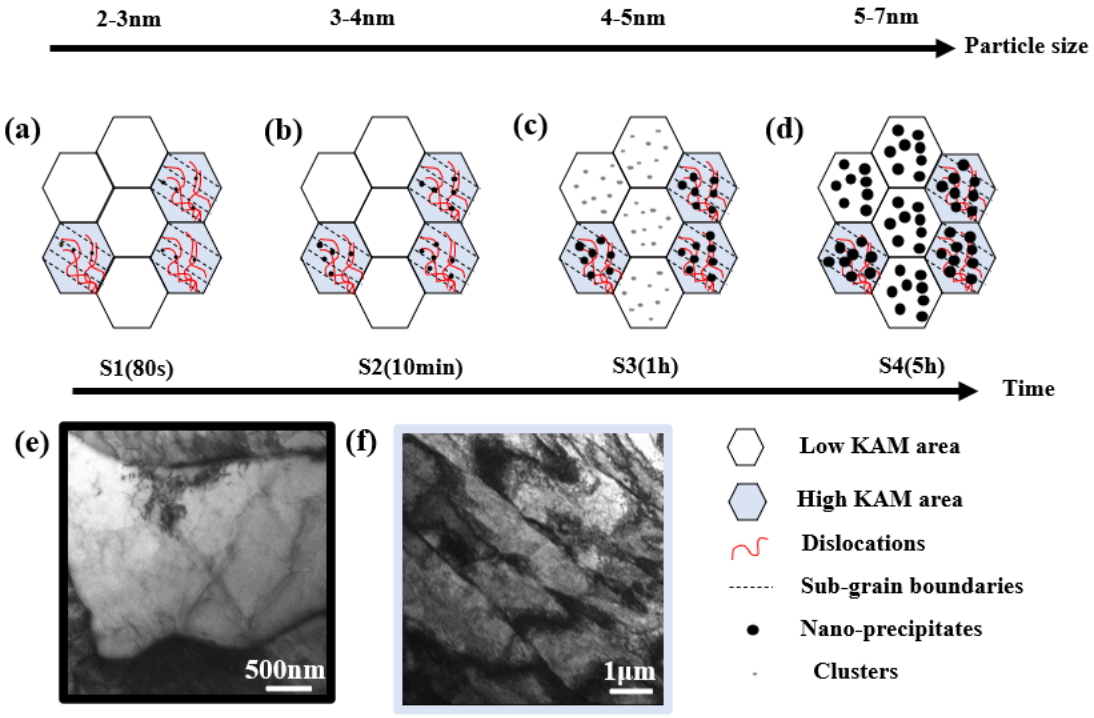


**Figure 4- 14. (a-b) Schematic of the nano-precipitates evolution in low KAM area and high KAM area during coiling for S1, S2, S3 and S4, respectively. (e-f) TEM images of ferrite and bainite in S3, respectively.**

The PF and BF which are formed during fast cooling will be supersaturated in V. BF contains more carbon than PF. However, limited C is detected around the nano precipitates by TEM and APT. The carbon in BF could precipitate as cementite then there will be limited carbon supersaturation to help V (C, N) nucleate. As a result, a large driving force

exists for the formation of VN precipitates. The evolution of the fine nano precipitates during isothermal holding at 500 ºC is summarized in the schematic diagram shown in **Figure 4- 14**. Starting with the high KAM regions, the precipitates appear to nucleate very quickly on the substructure/dislocations within these regions. The precipitates primarily contain V and N. The presence of some Mn within the precipitates cannot be ruled out, especially at longer times. The size of the precipitates gradually increased with increasing holding time. In contrast to rapid precipitation within the high KAM regions, no precipitates were observed in the low KAM even after 80, 600, and 3600 s. Precipitates were observed in the low KAM regions after 18,000 s of holding at 500 ºC. This suggests that dislocations and/or interfaces within the high KAM regions are effective nucleation sites for VN leading to a short incubation time. The low number of defects within PF (low KAM regions) leads to an extended incubation time and precipitates are only observed after 18,000s of holding. Solute clusters were observed within the low KAM region after 3600 s of holding. It is not clear whether these clusters formed at specific features within the microstructure or if they were randomly distributed. Some of these clusters may develop into the precipitates which were observed at the longest holding time (18,000 s).

### 4.2.2 Mechanical properties evolution

An extended elastoplastic transition is observed in the present steels. This is most evident in the S1(80 s) sample. This gradual yielding behavior has been reported in various bainitic steels [38, 39] and is usually attributed to the heterogeneity of microstructure as well as the presence of microscopic residual stresses. The dual-phase nature of the microstructure

consisting of PF and BF can also promote continuous yielding, similar to DP steels [40]. As the aging time increased, the elastoplastic transition occurred over a narrower range of strains. This could be attributed to the recovery of the microstructure which reduces heterogeneity and results in the decay of residual stresses. Additional microstructure changes which are expected to take place during aging include the clustering and/or precipitation of microalloyed carbides, as reported in section 3 as well as the redistribution of carbon to lower energy sites. In particular, carbon segregation to dislocations is expected at longer aging times. This will contribute to a higher apparent yield strength and a shorter elastoplastic region. These two changes contribute to an increase in the yield stress as a result of precipitates strengthening and dislocation locking, respectively.

Interestingly, the ultimate tensile strength was highest for the shortest aging time and decreased for longer aging times. The decrease is not very large, but it suggests that the contribution of precipitation strengthening is not very large and that it is offset by softening which is caused by the aging of bainite and associated recovery of dislocations. To explore this further, the contributions of the various strengthening mechanisms were estimated. A simple rule of mixtures (iso-strain) was employed to capture the contributions of polygonal ferrite and bainite:

$$YS = V_F * YS_F + V_B * YS_B \qquad \text{(Equation 4- 1)}$$

where $V_F$ and $V_B$ are the volume fractions of ferrite and bainite, while $YS_F$ and $YS_B$ represent the yield stresses of ferrite and bainite. Within each microconstituent, the various contributions were added linearly to obtain a first-order approximation of the yield stress:

$$YS = \sigma_0 + \sigma_{ss} + \sigma_{iss} + \sigma_g + \sigma_d + \sigma_p \quad \text{(Equation 4- 2)}$$

Here $\sigma_0$ is the lattice friction; $\sigma_{ss}$, $\sigma_{iss}$ are the solid solution strengthening contributions of substitutional and interstitial solutes, respectively. Finally, $\sigma_g$, $\sigma_d$ and $\sigma_p$, are the strengthening contributions due to grain refinement, dislocations, and precipitation, respectively. As discussed above, the final microstructure of the 4 samples consisted of ferrite and bainite. Keeping in mind that austenite decomposition was largely complete after 10 s of holding at 500 ºC, the volume fractions of ferrite ($V_F$) and bainite ($V_B$) will not change significantly with holding time. Using the EBSD data, the ferrite and bainite could be distinguished based on the presence of the substructure. The dilatometer result could also be used to get the volume fraction of ferrite and bainite. Based on the present results, a first-order estimate of the volume fractions of bainite ($V_B$) in the present samples is 0.7.

The contribution of solid solution strengthening to the yield stress of ferrite has been estimated from the literature [41-44]:

$$\sigma_0 + \sigma_{ss} + \sigma_{iss} \text{ [MPa]} = 54+32\text{Mn}+83\text{Si}+678\text{P}+39\text{Cu}+31\text{Cr}+11\text{Mo}+5000(C_{free} + N_{free}) \quad \text{(Equation 4- 3)}$$

where the solute content is expressed in mass%. The amount of free carbon in the low KAM areas was estimated from APT as 0.010 wt.%. The amount of free N is negligible due to the presence of Al and V which ties up the N in the form of AlN and VN particles. Using Eq. (3) the value of $\sigma_0 + \sigma_{SS} + \sigma_{iss}$ for ferrite is 190 MPa and its contribution to the yield stress of the steel (volume fraction-30%) is approximately 57 MPa.

The grain size contribution for ferrite was calculated using the standard Hall-Petch equation:

$$\sigma_{gf} \approx \left(ky \times d^{-\frac{1}{2}}\right) \quad \text{(Equation 4- 4)}$$

where $k_y$ is 0.55 MPa $m^{0.5}$ [45] and d is the ferrite grain size. Based on the EBSD data, the mean equivalent diameter was found to be 6-7 μm for the 4 samples, when only high-angle boundaries with misorientation angles over 15° are considered [41, 43, 44, 46, 47]. Thus, the calculated values of $\sigma_{gf}$ are around 223 MPa, which contributes 67 MPa to the strength of the steel given that the ferrite fraction is 0.3. Given the low dislocation density of polygonal ferrite, the contribution due to dislocation strengthening can be ignored. In addition, based on TEM observations, the only precipitate particles present in polygonal ferrite at the early stage of isothermal holding are the large (~20 nm) AlN particles that were inherited from the austenite. The contribution of these particles to strengthening is small because of their small volume fraction/large spacing. The contribution of ferrite to the yield strength of the steel is therefore expected to be of the order of 124 MPa and is not expected to change significantly during the early stages of aging (< 18000s).

A similar analysis can be performed to estimate the strength of bainite. An estimate of the contributions of intrinsic and solid solution strengthening could be obtained from Eq. (2) with a carbon content of 0.014 wt% as measured by APT. This leads to a contribution of ~211 MPa. Once we take into account the volume fraction of bainite (0.7), the contribution to the yield stress of the steel becomes 148 MPa. Following Young and Bhadeshia, the

strength of bainite is related to the lath thickness according to the following equation [43-45]:

$$\sigma_{gb} \approx (115(\bar{L}_3)^{-1}) \qquad \text{(Equation 4- 5)}$$

where $\bar{L}_3(\mu m)$ is a measure of bainite lath width. The values of the lath thickness were found to be of the order of 1.4 μm in this work based on the observation in Fig.14 (f). This would lead to a contribution of ~ 58 MPa to the yield stress of the steel. This is probably an upper limit as it considers the smallest possible mean-free path for the dislocation. The situation is more complex for the sample that was aged 18000 s (S4). In this sample, the bainite laths are no longer visible in large areas of the microstructure as a result of the granularization of bainite. This phenomenon was reported by other researchers and is attributed to the disappearance of high-angle boundaries (~60°) within the bainitic structure [31, 32]. As a result, part of the grain-size contribution calculated above will be lost for sample S4.

The contribution of dislocations to the strength of bainite is calculated using the Taylor equation [41, 43-45]:

$$\sigma_d = \alpha M \mu b \rho^{0.5} \approx 7.34 \times 10^{-6} \rho_D^{0.5} \qquad \text{(Equation 4- 6)}$$

where α is a constant M the average Taylor factor, and αM is taken as 0.38. Other symbols in equation (7) are μ, the shear modulus ($\mu \approx 8 \cdot 10^4$ MPa) and b, the magnitude of the Burgers vector ($b \approx 2.5 \cdot 10^{-10}$ m). The dislocation density is expected to decrease as a function of

the holding time. Following Young and Bhadeshia, an initial value of the dislocation density in bainitic ferrite can be estimated based on the transformation temperature[45]:

$$\log(\rho_D) = 9.2840 + \frac{6880.73}{T} - \frac{1780360}{T^2} \qquad \text{(Equation 4- 7)}$$

where T is the bainite transformation temperature in kelvin. Based on in-situ observations using the CLSM, T was estimated at 870 K, leading to a dislocation density of, $\rho_D \approx 6.93 \times 10^{14} m^{-2}$, and a strength increment of 193 MPa, which contributes 135 MPa to the yield stress of the steel after accounting for the volume fraction of bainite. Based on the above estimates, the initial contribution of bainite to the strength of the steel is ~340 MPa. This initial value does not include contributions from precipitate strengthening. As the aging time increases, the particle contribution will increase due to the precipitation of fine particles as observed in Section 3.

Based on the above, the initial yield stress of sample S1(which has the smallest precipitate strength contribution) is estimated from Eq. (1) as ~460 MPa, which is in good agreement with the measured value(~470Mpa). As the aging time increases, the dislocation contribution will decrease as a result of the recovery. This will be partly balanced by an increase in the precipitate contribution as a result of the formation of VN particles within the bainitic regions. A quantitative comparison of S2, S3 and S4 was not attempted due to the lack of data on dislocation density and precipitate spacing. Based on the experimental data, the softening and hardening contributions appear to large balance each other over the times investigated.

## 4.6 Conclusion

The following conclusions are drawn based on the results of the present study on the evolution of the microstructure and mechanical properties in V-containing microalloyed steel during coiling:

1. Fine nano precipitates (<10 nm) which contain V and N were formed during isothermal holding at 500ºC. The precipitates were heterogeneously distributed. In samples S1, S2 and S3, VN-containing nano precipitates (< 5 nm) were most often found in the high KAM value areas. The particle size of nano precipitates increased with increasing holding time. The heterogeneous distribution of the nano precipitates at the early stages of isothermal holding is explained by higher dislocation densities in the high KAM value areas. These dislocations act as nucleation sites for the precipitates.
2. An extended elastoplastic transition is observed in the present steels. This is most evident in the 80s sample and is attributed to the heterogeneity of the microstructure as well as the presence of microscopic residual stresses. The YS was lowest for S1 and increased for longer aging times. The limited increase of YS suggests that the contribution of precipitation strengthening is partially offset by the softening associated with the recovery of dislocation and granularization of bainite.

## 4.7 Acknowledgment

The authors would like to acknowledge the support of EVRAZ North America and the Natural Science and Engineering Research Council (Canada). The authors are grateful to CanmetMATERIALS (Hamilton, Canada) for performing the dilatometer experiments and mechanical testing. The characterization work was carried out at the Canadian Centre for Electron Microscopy, a national facility supported by the Canada Foundation for Innovation under the Major Science Initiative program, NSERC and McMaster University.

## 4.8 Supplementary Data

Optical metallography of the 4 samples (Fig. S1) shows that the microstructure does not significantly change during the first 600 s. After 18000 s of holding at 500 °C, however, the microstructure appears to become coarser and fine bainitic ferrite laths begin to disappear in many regions. It suggests the "granularization" of bainite during coiling.

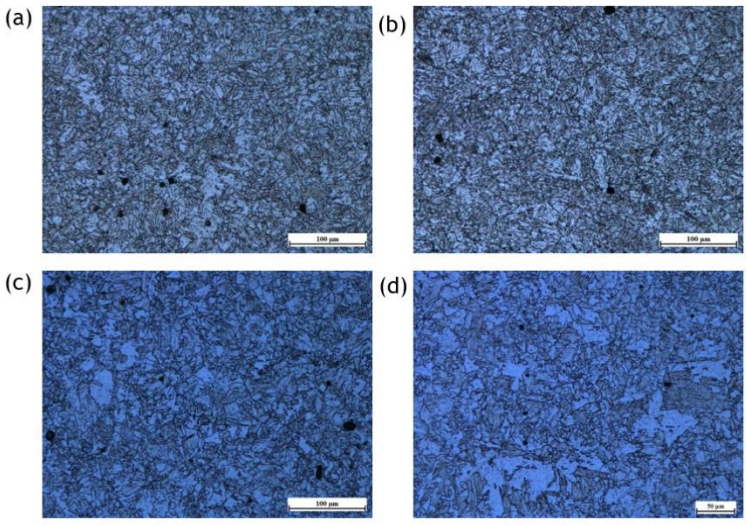


**Figure 4- 15. (a-d): Optical micrograph of S1, S2, S3 and S4, respectively.**

## 4.9 Reference

[1] T. Gladman, The physical metallurgy of microalloyed steels, Maney Pub1997.

[2] A. Davenport, L. Brossard, R. Miner, Precipitation in microalloyed high-strength low-alloy steels, JOM 27(6) (1975) 21-27.

[3] M. Charleux, W. Poole, M. Militzer, A. Deschamps, Precipitation behavior and its effect on strengthening of an HSLA-Nb/Ti steel, Metallurgical and Materials Transactions A 32(7) (2001) 1635-1647.

[4] D. Belato Rosado, W. De Waele, D. Vanderschueren, S. Hertelé, Latest developments in mechanical properties and metallurgical features of high strength line pipe steels, 5th International Conference on Sustainable Construction and Design, Ghent University, Laboratory Soete, 2013.

[5] V.M.H. KONSTRUKCIJSKA, High-strength low-alloy (HSLA) steels, Materiali in tehnologije 45(4) (2011) 295-301.

[6] H.J. Kong, C.T. Liu, A review on nano-scale precipitation in steels, Technologies 6(1) (2018) 36.

[7] Z. Xiong, I. Timokhina, E. Pereloma, Clustering, nano-scale precipitation and strengthening of steels, Progress in Materials Science 118 (2021) 100764.

[8] C. Gu, M.J. Gaudet, J. Su, B. Langelier, H. Yuan, N. Bassim, H. Zurob, Advanced Characterization of Precipitation and Microstructure Heterogeneity in X70 Steel, Metallurgical and Materials Transactions A (2022) 1-8.

[9] S. Liang, X. Wang, C. Andrei, H.S. Zurob, NbC precipitation during two-pass hot deformation of a nickel-based model alloy at 700° C: Experiments and modelling, Materials Science and Engineering: A 802 (2021) 140447.

[10] S. Liang, X. Wang, H.S. Zurob, NbC precipitation during multi-pass deformation of a nickel-based model alloy: Experiments and modelling, Materials Science and Engineering: A 772 (2020) 138748.

[11] B. Dutta, E.J. Palmiere, C.M. Sellars, Modelling the kinetics of strain induced precipitation in Nb microalloyed steels, Acta materialia 49(5) (2001) 785-794.

[12] P. Gong, E.J. Palmiere, W.M. Rainforth, Characterisation of strain-induced precipitation behaviour in microalloyed steels during thermomechanical controlled processing, Materials Characterization 124 (2017) 83-89.

[13] D. Poddar, P. Cizek, H. Beladi, P.D. Hodgson, Evolution of strain-induced precipitates in a model austenitic Fe–30Ni–Nb steel and their effect on the flow behaviour, Acta materialia 80 (2014) 1-15.

[14] A. Davenport, F. Berry, R. Honeycombe, Interphase precipitation in iron alloys, Metal Science Journal 2(1) (1968) 104-106.

[15] R. Okamoto, A. Borgenstam, J. Ågren, Interphase precipitation in niobium-microalloyed steels, Acta Materialia 58(14) (2010) 4783-4790.

[16] H.-J. Kestenbach, S. Campos, E. Morales, Role of interphase precipitation in microalloyed hot strip steels, Materials science and technology 22(6) (2006) 615-626.

[17] F. Bu, X. Wang, S. Yang, C. Shang, R. Misra, Contribution of interphase precipitation on yield strength in thermomechanically simulated Ti–Nb and Ti–Nb–Mo microalloyed steels, Materials Science and Engineering: A 620 (2015) 22-29.

[18] V. Challa, W. Zhou, R. Misra, R. O'Malley, S. Jansto, The effect of coiling temperature on the microstructure and mechanical properties of a niobium–titanium microalloyed steel processed via thin slab casting, Materials Science and Engineering: A 595 (2014) 143-153.

[19] Z. Jia, R. Misra, R. O'malley, S. Jansto, Fine-scale precipitation and mechanical properties of thin slab processed titanium–niobium bearing high strength steels, Materials Science and Engineering: A 528(22-23) (2011) 7077-7083.

[20] K.Y. Xie, T. Zheng, J.M. Cairney, H. Kaul, J.G. Williams, F.J. Barbaro, C.R. Killmore, S.P. Ringer, Strengthening from Nb-rich clusters in a Nb-microalloyed steel, Scripta Materialia 66(9) (2012) 710-713.

[21] Z. Wang, H. Li, Q. Shen, W. Liu, Z. Wang, Nano-precipitates evolution and their effects on mechanical properties of 17-4 precipitation-hardening stainless steel, Acta Materialia 156 (2018) 158-171.

[22] S. Dhara, R. Marceau, K. Wood, T. Dorin, I. Timokhina, P. Hodgson, Precipitation and clustering in a Ti-Mo steel investigated using atom probe tomography and small-angle neutron scattering, Materials Science and Engineering: A 718 (2018) 74-86.

[23] G. Edwards, K. Stiller, G. Dunlop, M. Couper, The precipitation sequence in Al–Mg–Si alloys, Acta materialia 46(11) (1998) 3893-3904.

[24] V. Fallah, B. Langelier, N. Ofori-Opoku, B. Raeisinia, N. Provatas, S. Esmaeili, Cluster evolution mechanisms during aging in Al–Mg–Si alloys, Acta Materialia 103 (2016) 290-300.

[25] M. Niu, G. Zhou, W. Wang, M.B. Shahzad, Y. Shan, K. Yang, Precipitate evolution and strengthening behavior during aging process in a 2.5 GPa grade maraging steel, Acta Materialia 179 (2019) 296-307.

[26] L.-H. Lee, C.-H. Yu, C.-Y. Wei, P.-C. Lee, J.-S. Huang, C.-Y. Wen, Plan-view transmission electron microscopy specimen preparation for atomic layer materials using a focused ion beam approach, Ultramicroscopy 197 (2019) 95-99.

[27] C. Li, G. Habler, L.C. Baldwin, R. Abart, An improved FIB sample preparation technique for site-specific plan-view specimens: A new cutting geometry, Ultramicroscopy 184 (2018) 310-317.

[28] K. Thompson, D. Lawrence, D. Larson, J. Olson, T. Kelly, B. Gorman, In situ site-specific specimen preparation for atom probe tomography, Ultramicroscopy 107(2-3) (2007) 131-139.

[29] M.K. Miller, Atom probe tomography: analysis at the atomic level, Springer Science & Business Media2012.

[30] B. Gault, M.P. Moody, J.M. Cairney, S.P. Ringer, Atom probe microscopy, Springer Science & Business Media2012.

[31] M. Ben Haj Slama, N. Gey, L. Germain, J.C. Hell, K. Zhu, S. Allain, Fast granularization of lath-like bainite in FeNiC alloys during isothermal holding at Ms+ 20 K (+ 20 C), Metallurgical and Materials Transactions A 47 (2016) 15-18.

[32] M. Ben Haj Slama, N. Gey, L. Germain, K. Zhu, S. Allain, Key parameters to promote granularization of lath-like bainite/martensite in FeNiC alloys during isothermal holding, Materials 11(10) (2018) 1808.

[33] S. Zaefferer, P. Romano, F. Friedel, EBSD as a tool to identify and quantify bainite and ferrite in low-alloyed Al-TRIP steels, Journal of microscopy 230(3) (2008) 499-508.

[34] Y.-W. Chen, Y.-T. Tsai, P.-Y. Tung, S.-P. Tsai, C.-Y. Chen, S.-H. Wang, J.-R. Yang, Phase quantification in low carbon Nb-Mo bearing steel by electron backscatter diffraction technique coupled with kernel average misorientation, Materials Characterization 139 (2018) 49-58.

[35] J. Omale, E. Ohaeri, J. Szpunar, M. Arafin, F. Fateh, Microstructure and texture evolution in warm rolled API 5L X70 pipeline steel for sour service application, Materials Characterization 147 (2019) 453-463.

[36] J. Omale, E. Ohaeri, A. Tiamiyu, M. Eskandari, K. Mostafijur, J. Szpunar, Microstructure, texture evolution and mechanical properties of X70 pipeline steel after

different thermomechanical treatments, Materials Science and Engineering: A 703 (2017) 477-485.

[37] S.-I. Lee, S.-Y. Lee, S.G. Lee, H.G. Jung, B. Hwang, Effect of strain aging on tensile behavior and properties of API X60, X70, and X80 pipeline steels, Metals and Materials International 24(6) (2018) 1221-1231.

[38] B. Avishan, C. Garcia-Mateo, L. Morales-Rivas, S. Yazdani, F.G. Caballero, Strengthening and mechanical stability mechanisms in nanostructured bainite, Journal of Materials Science 48 (2013) 6121-6132.

[39] X. Zhang, G. Xu, X. Wang, D. Embury, O. Bouaziz, G.R. Purdy, H.S. Zurob, Mechanical behavior of carbide-free medium carbon bainitic steels, Metallurgical and Materials Transactions A 45 (2014) 1352-1361.

[40] A.A. Sayed, S. Kheirandish, Affect of the tempering temperature on the microstructure and mechanical properties of dual phase steels, Materials Science and Engineering: A 532 (2012) 21-25.

[41] A. Iza-Mendia, I. Gutiérrez, Generalization of the existing relations between microstructure and yield stress from ferrite–pearlite to high strength steels, Materials Science and Engineering: A 561 (2013) 40-51.

[42] I. Gutiérrez, M. Altuna, Work-hardening of ferrite and microstructure-based modelling of its mechanical behaviour under tension, Acta Materialia 56(17) (2008) 4682-4690.

[43] L. García-Sesma, B. López, B. Pereda, Effect of coiling conditions on the strengthening mechanisms of Nb microalloyed steels with high Ti addition levels, Materials Science and Engineering: A 748 (2019) 386-395.

[44] L. Sanz, B. Pereda, B. López, Effect of thermomechanical treatment and coiling temperature on the strengthening mechanisms of low carbon steels microalloyed with Nb, Materials Science and Engineering: A 685 (2017) 377-390.

[45] c.H. Young, H. Bhadeshia, Strength of mixtures of bainite and martensite, Materials Science and Technology 10(3) (1994) 209-214.

[46] Z. Wang, W. Hui, Z. Chen, Y. Zhang, X. Zhao, Effect of vanadium on microstructure and mechanical properties of bainitic forging steel, Materials Science and Engineering: A 771 (2020) 138653.

[47] L. Rancel, M. Gómez, S.F. Medina, I. Gutierrez, Measurement of bainite packet size and its influence on cleavage fracture in a medium carbon bainitic steel, Materials Science and Engineering: A 530 (2011) 21-27.

# Chapter 5 Site-specific Analysis of Precipitates During the Coiling of an HSLA Steel Containing V and Nb.

This chapter is reproduced from the work: *Gu, Chen, Colin Scott, Fateh Fazeli, Xiang Wang, Nabil Bassim, and Hatem Zurob. " Site-specific Analysis of Precipitates During the Coiling of an HSLA Steel Containing V and Nb.”*, which is under review in the Journal of Materials Research and Technology. The author of this thesis is the first author and the main contributor of this publication, including conceiving the initial ideas, development of approach and methodology, carrying out experiments, analysis of data, and preparation of the manuscript.

## 5.1 Abstract

Precipitation in an HSLA steel containing V and Nb additions during coiling at 500 ºC, was investigated by advanced characterization techniques including EBSD, FIB, TEM, and APT. During coiling, nano precipitates were preferentially formed around dislocations and grain/sub-grain boundaries in the high Kernel Average Misorientation (KAM) areas associated with bainite. Precipitates were frequently observed around cementite in the low KAM areas with cementite which were identified as granular bainite. Interphase clusters were found in the low KAM areas associated with ferrite. The results suggest that variations in the spatial distribution of precipitates are due to variations in the microstructure formed during cooling from the finishing temperature to the coiling temperature. Analysis of the

results indicates that the precipitation of micro-alloy particles close to cementite could lower the precipitation hardening contribution that could be achieved by microalloying.

**Keywords: HSLA, clusters, precipitation, site-specific, mechanical properties.**

## 5.2 Introduction

High-strength low-alloy steels (HSLA) offer an attractive combination of strength, low-impact transition temperature, good weldability, and low cost. These steels have been widely used for oil and gas pipelines, and automobile components [1-4]. Microalloying additions are critical for obtaining the desired microstructures in the HSLA. In particular, the strength of these steels is due, primarily, to the refinement of the ferrite grain size and precipitation of fine micro-alloy carbonitrides. Microalloy precipitates that form in HSLA are commonly classified as strain-induced precipitates (SIP), interphase precipitates, and matrix precipitates [5-10]. The precipitation of carbides or carbonitrides in the form of (MX) (M=Mo, Nb, V, Ti and X=C, N) influences the mechanical properties by impending grain growth and dislocation movement[3, 8].

It is well known that MX particles can contain one or more microalloying elements, thus in addition to simple carbides and nitrides, such as NbC and TiN, it is also possible to form complex carbonitrides such as (Nb, Ti)(C, N)[11-15]. There is a large body of literature on the precipitation of simple microalloyed carbonitrides in model steels[12, 16-18]. The precipitation of complex carbonitrides during hot rolling has also received a lot of

attention[13, 15, 19, 20]. In contrast, the precipitation of these carbonitrides during coiling has received significantly less attention [20-22]. This is partly due to the very small size of these precipitates and/or clusters which makes the analysis much more complicated. The work of Li et al. [20] investigated the formation mechanisms of complex precipitates (Nb, V)C in Nb-V microalloyed steel. The results show that the precipitate nucleus is enriched in V in order to reduce the lattice misfit between the carbide and the matrix [20]. It is also reported that the ratio of V/ Nb increases with the increase of particle size during isothermal holding at 600-700°C in a Nb-V-bearing low-carbon steel [21]. However, the ratio of C and N in the different particles was not discussed.

When investigating the precipitation of microalloying elements during coiling, it is necessary to use site-specific analysis to correlate the precipitation kinetics with the microstructure constituent in which the precipitates form. Our recent work on V (C, N) precipitation during the coiling of V-containing steel, clearly illustrated this point. The results showed that precipitation kinetics are faster in the high Kernel Average Misorientation (KAM) map areas due to the presence of dislocations and sub-boundaries. In this work, a V-Nb steel was used to study more complex (Nb, V) (C, N) precipitates in high and low KAM areas and the relationship between the microstructure and mechanical properties. Three different areas (lath bainite, granular bainite and allotriomorphic ferrite) were examined using FIB lift out, followed by TEM and APT analysis.

## 5.3 Material and methods

The material used in the present study was supplied by CanmetMATERIALS in the form of a 1 mm cold-rolled sheet. The steel contained 0.068C-0.25Si-1.91Mn-0.044Al-0.0009Ti-0.104V-0.03Nb-0.0058N-0.0034S (all in mass %). The solution temperature of (Nb, V) (C, N) in the steel is around 1119°C based on a calculation using the Thermo-Calc TCFE9 database. Heat treatment of the studied material was carried out using a high-temperature confocal laser scanning microscope (CLSM, LasertecVL2000DX) which allowed in-situ observation of the transformation. The polished specimens (4×3.6×1, RD×TD×ND, mm) were reheated to 1200ºC and held for 5 min, before being cooled to 500 ºC at a cooling rate of 30 ºC /s. The samples were kept at 500 ºC for 1h, followed by Ar quenching (30 ºC /s) to room temperature. In addition, rectangular samples with dimensions of 4 mm×10 mm×1 mm (RD×TD×ND) were machined from the as-received material by Electrical Discharge Machining (EDM) for further study of the phase transformations using a BAHR DIL 805 dilatometer. The heat treatment in the dilatometer is the same as the one in CLSM.

After the heat retreatment in CLSM, the sample was analyzed by EBSD. KAM maps were used to select specific areas for precipitate analysis. The workflow of the site-specific analysis in this study can be found in our previous work [13]. All EBSD analyses were performed using a JEOL JSM-7000F SEM equipped with a Nordlys II EBSD Camera. The EBSD data was then processed in HKL Channel 5 EBSD postprocessing software.

TEM samples from low KAM and high KAM areas were extracted by the plan view lift-out method [23, 24] in a Thermo Fisher Scientific Helios G4 UXe Dual-Beam PFIB microscope. The samples were then imaged in a Thermo Fisher Scientific Talos 200X TEM equipped with four in-column silicon drift EDX (SDD) Super-X detectors in Scanning TEM (STEM) mode. The composition, morphology, and distribution of the particles were measured by EDS and EELS.

Atom Probe Tomography (APT) tips from the low and high KAM areas were lifted out using PFIB by mounting to Si microchips using a standard lift-out method [25]. A Cameca local electrode atom probe (LEAP) 4000X HR was used for APT experiments at a base temperature of 59.7 K in laser pulsing mode ($\lambda$ = 355 nm), with a pulse rate of 250 kHz, a pulse energy in the range of 50–60 pJ and a targeted detection rate of 0.01 ions/pulse (1 %). Reconstruction and analysis of APT data were performed using the IVAS 3.6.8 software and established reconstruction protocols. Reconstructions were spatially calibrated using the known spacing of crystal planes. A more detailed discussion of the employed APT data analysis methods can be found in [26, 27]. In the reconstructed APT data, the identification and characterization of clusters/precipitates were undertaken using the maximum separation method [28, 29]. The parameters chosen to define the maximum separation were $d_{max}$ = 1.2 nm and $N_{min}$ = 15 atoms. The Guinier radius ($r_g$) of the clusters and precipitates was estimated to be. 1.67 times the radius of gyration ($l_g$) [29].

The mechanical properties of the studied material were measured using ASTM E8/E8M sub-size tensile samples. The samples were tested using an MTS 370 Landmark 100 kN frame with an Instron 2620-604 25 mm extensometer. The strain rate was $2x10^{-3}$/s.

Additional specimens were heat-treated, and thin foils were prepared for TEM observation. These observations investigated larger areas than what is possible from site-specific FIB lift-outs. The samples were thinned down to about 0.8 mm in thickness by mechanical grinding and 3 mm diameter discs were punched out of the sheet. The final electro-polishing was carried out using 10% perchloric acid and methanol at -40C and 16 V. The thin foils were examined in a Talos L120C electron microscope operating at 120KV.

## 5.4 Results

The thermal dilatometric curve of the V + Nb steel is presented in **Figure 5- 1**a. It indicates that the decomposition of austenite starts around 650 ºC and stops after holding at 500 ºC for around 10s. The final microstructure mainly consists of bainite and ferrite, as marked in **Figure 5- 1**b. Earlier work on similar steel [chapter 4] showed that as the isothermal transformation time increases, some of the high-angle boundaries within bainite disappear and the lath bainite morphology is replaced by a "granular" morphology that some authors refer to as granular bainite. These micro constituents could be better identified based on KAM and the presence of cementite, as shown in **Figure 5- 1**c and **Figure 5- 1**d. The KAM map provides the average misorientation angle of a given point with respect to all of its neighbors [30, 31]. High KAM areas could be lath bainite which has more dislocations and

substructure, low KAM areas could be the ferrite or granular bainite as both have fewer dislocations and boundaries than lath bainite [32-34]. In general, allotriomorphic ferrite does not contain a lot of cementite, thus the three microconstituents could be identified based on KAM and the presence of cementite, as marked in **Figure 5- 1**c and d.

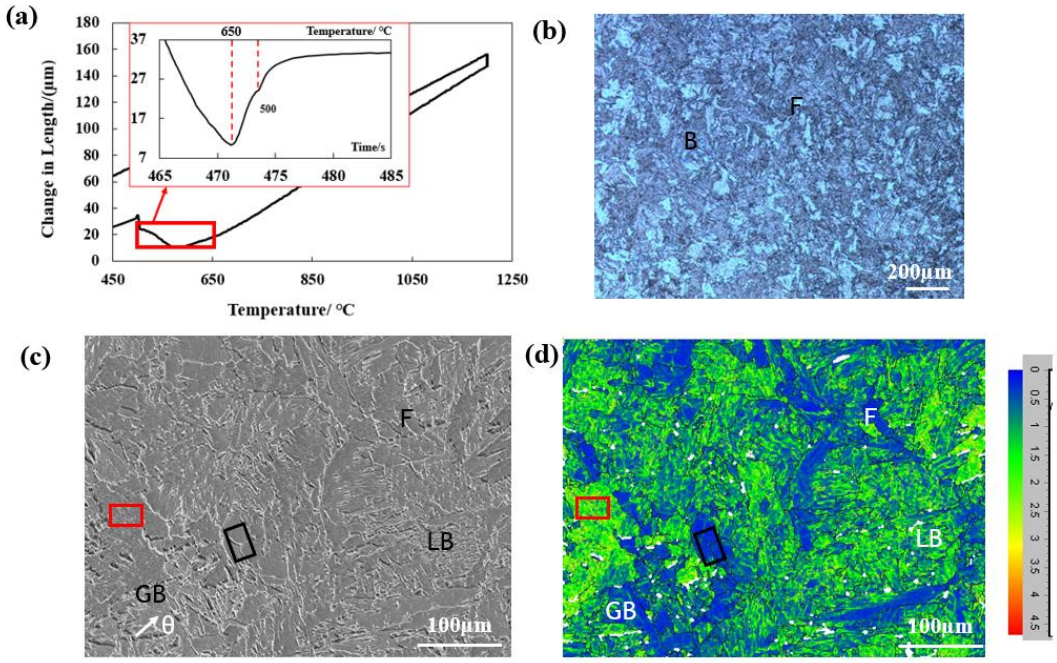


**Figure 5- 1. (a) Thermal dilatometric curve of V + Nb steel, inset (metric-time curve at the isothermal hold of 500°C. (b) Optical image (OM) of the final microstructure using nital 2% etching. (c) Scanning electron microscopy (SEM) images of the final microstructure and corresponding (d) KAM map. (F-ferrite, B-bainite, LB-lath bainite, GB-granular bainite, θ-cementite).**

TEM observations (**Figure 5- 2**) confirm the presence of ferrite, granular bainite, and lath bainite. The area with limited dislocation density and without cementite is ferrite. Granular bainite is identified by the presence of cementite particles and low dislocation density. As shown in **Figure 5- 2**b and c, cementite particles with sizes (in length) from 0.4-2 μm are

observed frequently in granular bainite. Finally, lath bainite is clearly identified by its high dislocation density and the presence of lath boundaries as shown in **Figure 5- 2**(a).

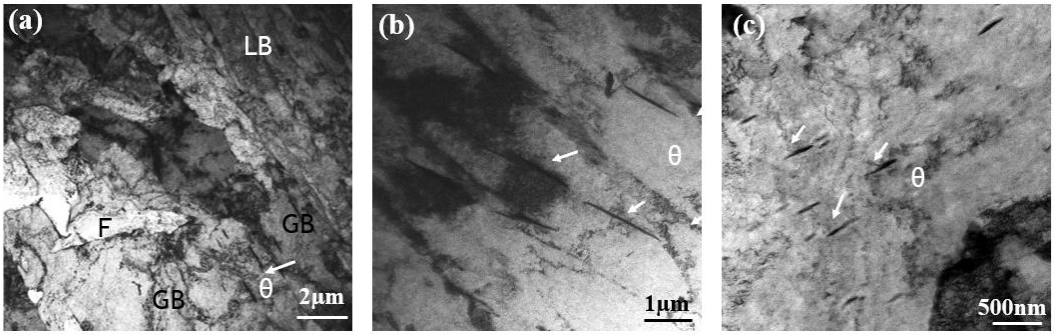


**Figure 5- 2. (a) TEM bright field (BF) image of the final microstructure in the studied material. (F-ferrite, LB-lath bainite, GB-granular bainite, θ-cementite). (b-c) TEM bright field (BF) image of the cementite in the studied material.**

The precipitates inside these microstructures are investigated in detail in this work. A high KAM area (red frame) which contains lath bainite and a low KAM area (black frame) which contains both ferrite and granular bainite are lifted by FIB for precipitate analysis, as shown in **Figure 5- 1**c and **Figure 5- 1**d. In the high KAM area, precipitates are frequently observed around dislocations and grain/sub-grain boundaries. **Figure 5- 3** clearly shows the presence of V particles around a dislocation node. Limited Nb and N are detected around these particles, but it is hard to tell whether C is also present within these particles. The diameter of the precipitates formed on dislocations ranges from 2 to 6 nm. More examples of the precipitates around dislocations and corresponding selected area diffraction patterns can be found in **Figure 5- 13** in the supplementary material.

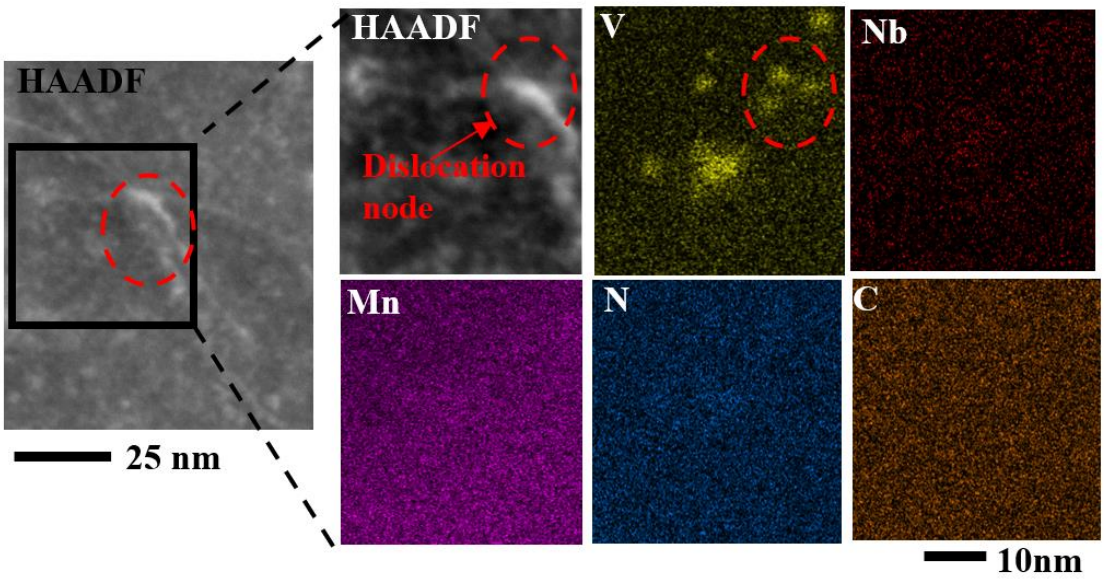


**Figure 5- 3. EDS mapping of the nano precipitates around a dislocation node**

Fewer precipitates are observed around grain/sub-grain boundaries, Usually, these boundaries have some dislocations around them. **Figure 5- 4** shows the presence of V-rich particles at a boundary running near the middle of the image. The presence of Nb and N at these particles is hard to distinguish at this magnification. Observation at high magnification confirms the presence of N and limited Nb. The diameter of the precipitates at the boundary also ranges from 2 to 6 nm.

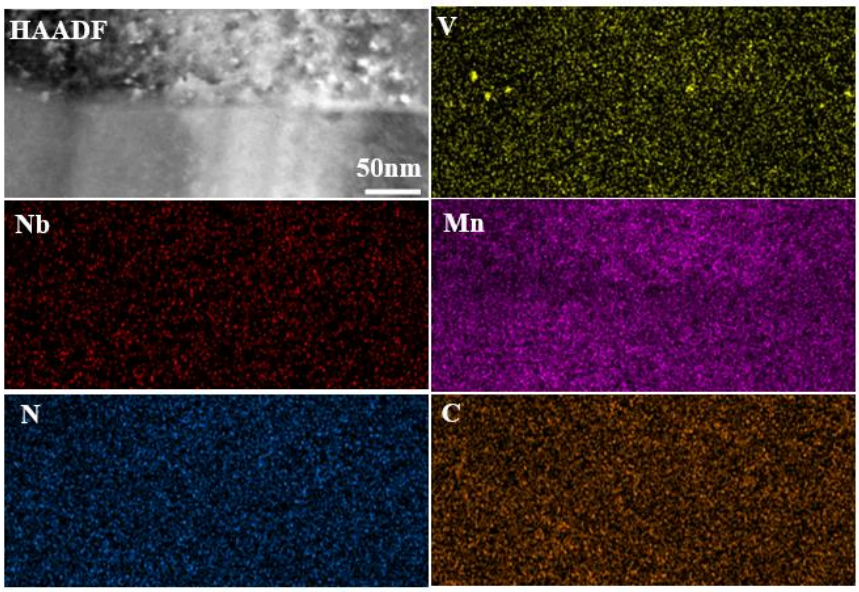


**Figure 5- 4. EDS mapping of the nano precipitates around the boundary.**

Interestingly, nano precipitates of V, Nb, and N are more frequently found on or near the cementite/matrix interface. An example is shown in **Figure 5- 5**. The diameter of the precipitates around cementite ranges from 2.5 to 7 nm. Interestingly, the precipitates on the cementite are usually larger than those found on dislocations and at boundaries.

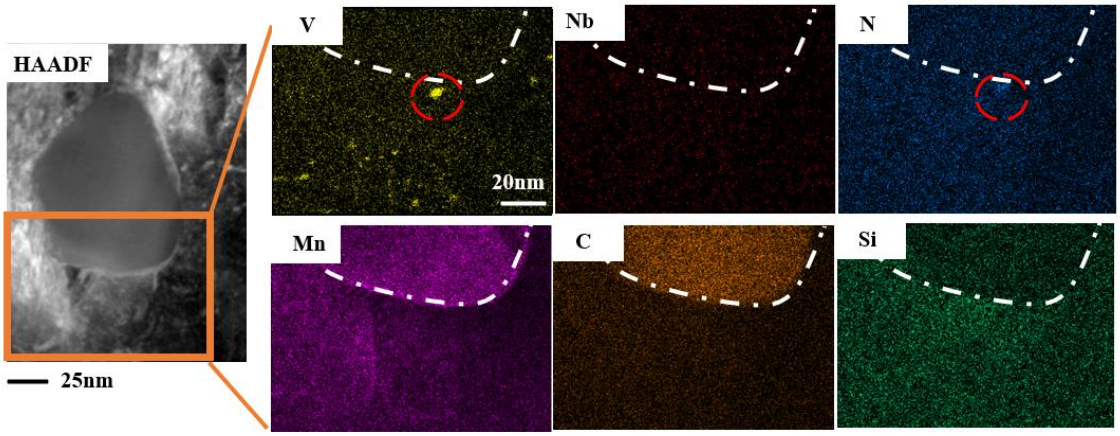


**Figure 5- 5. EDS mapping of the nano precipitates around cementite**

In order to further investigate the composition of the precipitates in different areas, APT analyses were conducted in specific areas chosen based on the KAM maps and microstructure observations in the SEM. **Figure 5- 6**a presents the EBSD grain boundary maps and corresponding KAM maps (inserted) used to identify regions for APT lift-out. P1 is selected from the high KAM area, which could be identified as lath bainite with a lot of dislocations and sub-boundaries. P2 is an area selected from the low KAM area with cementite. This area was identified as granular bainite. The other area, P3, is also selected from a low KAM area without cementite. This area is identified as ferrite. For each region, 2-3 tips were analyzed.

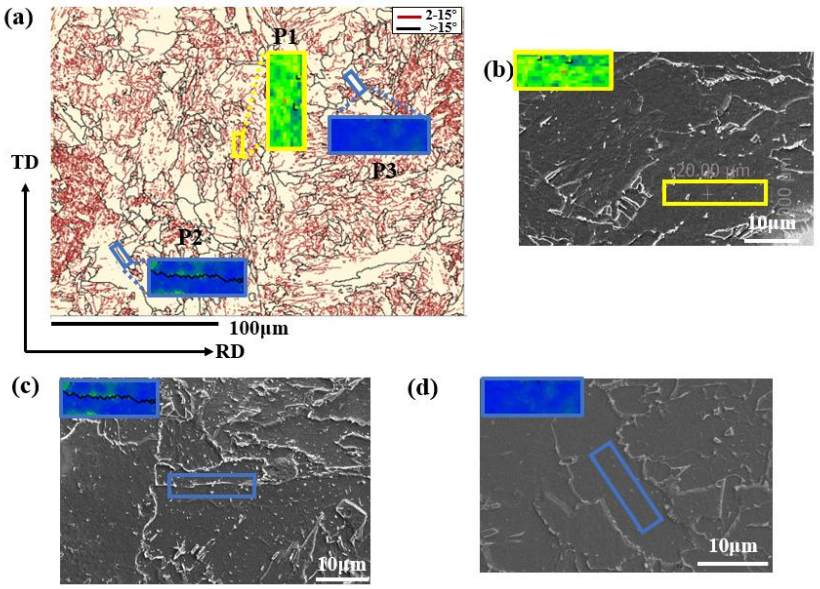


**Figure 5- 6. (a) EBSD grain boundary maps and corresponding KAM maps(inserted) in the selected area of V + Nb steel for later APT analysis. (b-d) is the corresponding microstructure in SEM of the selected area P1, P2 and p3 respectively.**

The APT dataset obtained from the high KAM area (P1) is shown in **Figure 5- 7**. The C atomic map in **Figure 5- 7**a shows that there are some dislocations and sub-grain boundaries in the analyzed tips. This is in agreement with TEM observations. The lath bainite in the studied material has more dislocations and many sub-boundaries. The segregation of V, VN, Nb, and NbN around the dislocation can be observed in **Figure 5-7**(a). The detailed information of the selected areas (red frame) in the V, VN, Nb, and NbN atomic map is presented in **Figure 5- 7**b. The segregation of these species is in the shape of an ellipse with a size of around 5 nm. Since these areas have regular shapes and a large number of solute atoms (>15), they are identified as nano precipitates in this work. The

precipitates mainly contain V, Nb, and N. The concentration map of C suggests that C is not an important element for the formation of these precipitates, as shown in **Figure 5- 14** in the supplementary material. However, a lot of N is detected in the precipitates, in agreement with earlier TEM observations (**Figure 5- 3**).

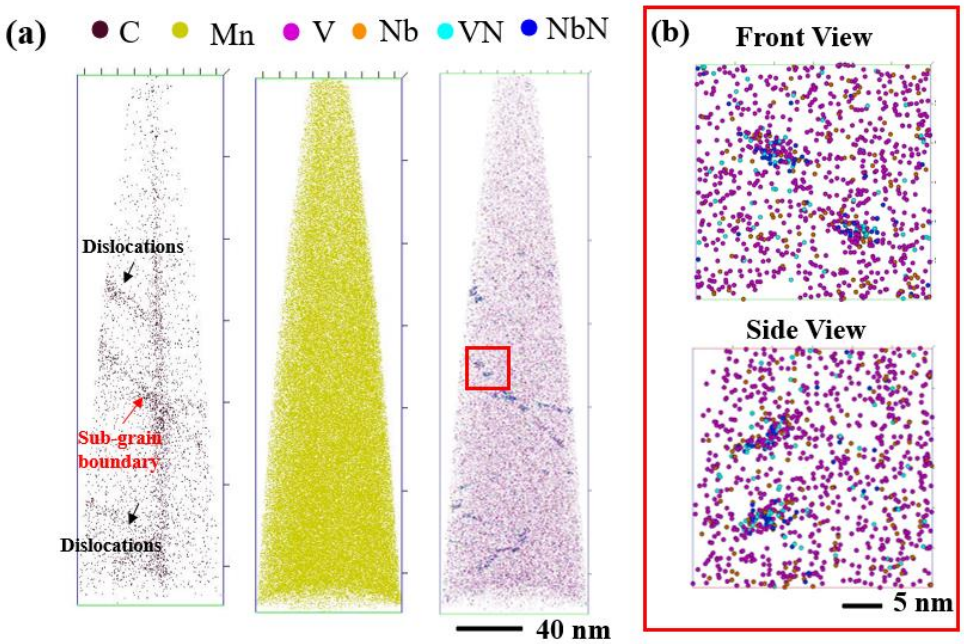


**Figure 5- 7. APT result of V + Nb steel in the high KAM area (P1): 3D atomic map of C, Mn, and V, VN, Nb, and NbN, respectively (the axial segregation of C is an artifact). (b) atomic map in the selected area of (a).**

Different kinds of precipitates are observed in P2, which is an area of granular bainite. **Figure 5- 8**a shows 3D atomic maps of C, Mn, and Si. A clear feature is observed in the lower right corner of the tip. Within this region, C and Mn are present in high concentration but Si is absent. This solute distribution pattern suggests that this feature is a cementite plate. The concentration profiles of C, Mn, and Si in ROI-1 are shown is presented in Fig.

8(b). The observed C (~20 at%) and Mn (2-5 at%) enrichment within cementite is consistent with the values measured by EDS analysis in the TEM foils.

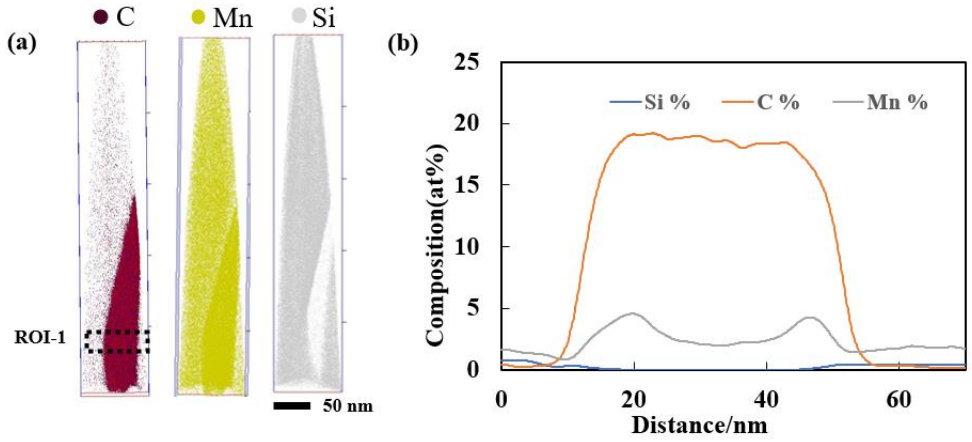


**Figure 5- 8. (a) 3D atomic map of C, Mn, Si in V+Nb steel in low KAM area(P2) with cementite, respectively. (b) Concentration profile of C, Mn, and Si in ROI-1.**

It is worth mentioning that 3 tips were analyzed in area P2, and many V-containing precipitates were observed on cementite particles. In contrast, only poorly defined clusters are observed in the matrix away from the cementite, as shown in **Figure 5- 15** in the supplementary material. This indicates that the V-containing particles prefer to nucleate on or near cementite. The 3D atomic map of V, VN, Nb, and NbN in the same tip discussed in **Figure 5- 8** is presented in Fig 9(a). Areas with high V concentration can be observed clearly in **Figure 5- 9**a. The size of these solute-rich areas varies depending on their distance from the cementite particle. The areas away from the cementite such as ROI-2 are smaller than the ones near cementite (ROI-3), as shown in **Figure 5- 9**b and **Figure 5- 9**c respectively. The results show that V is more strongly enriched in these particles. It is believed clusters and precipitates co-existed in this tip based on the size distribution and

composition variation. The V-rich areas on the cementite are mostly likely precipitates, while the V-rich areas away from the cementite could be best described as solute-rich clusters.

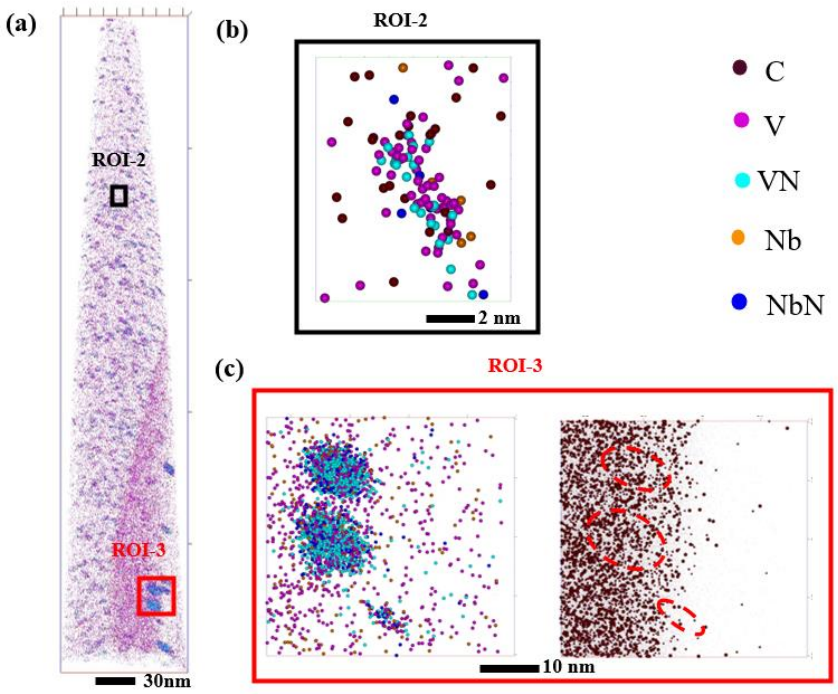


**Figure 5- 9. (a) 3D atomic map of V+VN +Nb + NbN in the same Tip of Fig 8. (b) Atomic map of V, VN, Nb, NbN, C in the ROI-2 (c) Atomic map of V, VN, Nb, NbN, and C in ROI-3, respectively.**

For the APT tip extracted from ferrite (P3), C and Mn segregation were not observed as shown in **Figure 5- 10**a. This suggests the absence of dislocations, substructure, and cementite within the analyzed tips. This is consistent with the characteristic of allotriomorphic ferrite. Well-defined precipitates were not observed in the analyzed area. Instead, a large number of solute clusters were present. Some of these clusters appeared to

be distributed in rows, as shown in **Figure 5- 10**b, which shows 0.9 at. % V and 0.38 at. %Nb iso-concentration surfaces. These clusters are distributed in the plane with a spacing of around 25 nm. The distribution of V, VN, Nb, and NbN in the selected area of **Figure 5- 10**b is shown in **Figure 5- 10**c. These clusters do not have a regular shape and contain few atoms. This kind of cluster mainly contains V, Nb C, and N, as plotted in **Figure 5- 10**d.

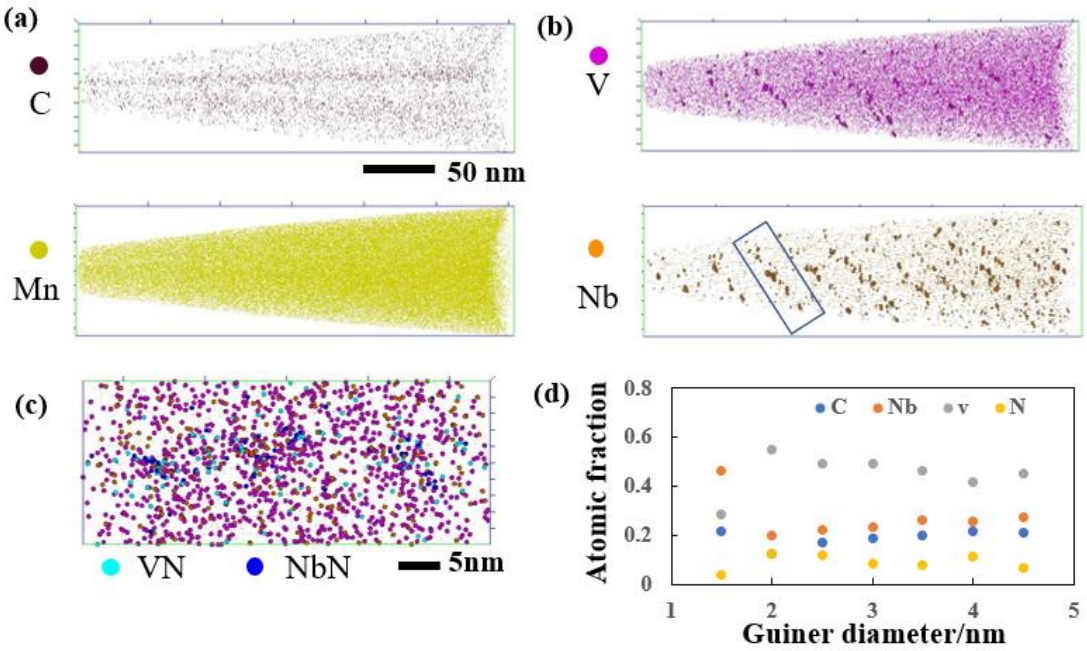


**Figure 5- 10. APT result of V + Nb steel in the low KAM area without cementite(P3). (a)3D atomic map of C, Mn, respectively. (b) 0.9 at. % V and 0.38 at. %Nb concentration iso-surface of the clusters respectively. (c) Atomic map of V, VN, Nb, and NbN in the selected region of (b). (d) Atomic fraction of V, Nb, C, and N (decomposed)variation of cluster/precipitates vs. Guinier diameter of the cluster/precipitates.**

The engineering stress-strain curve of the studied material is plotted in **Figure 5- 11**. The average yield strength (YS at 0.2% offset) is around 450 MPa and the ultimate tensile strength (UTS) is around 630MPa.

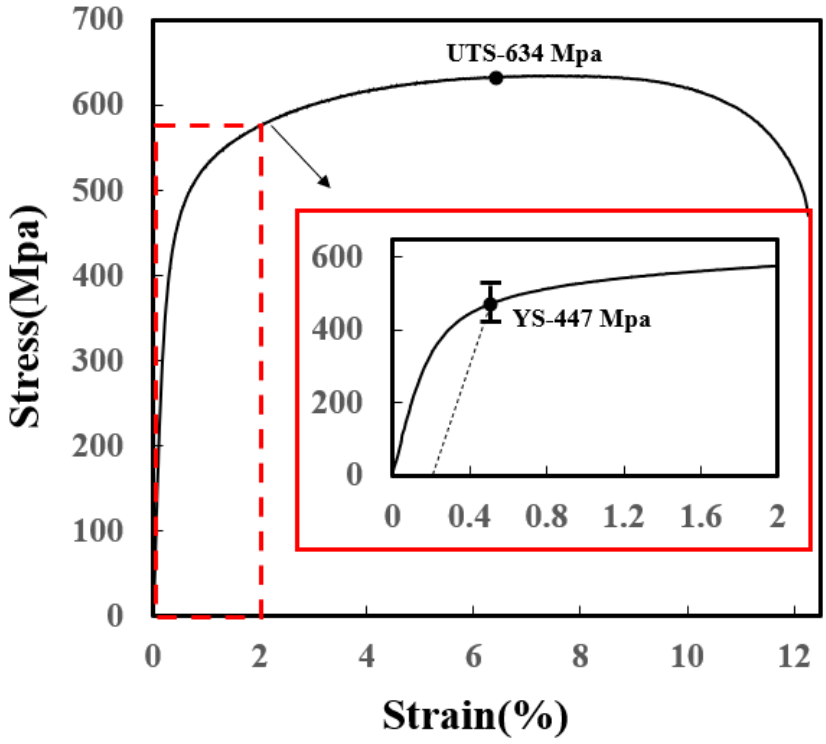


**Figure 5- 11. Engineering stress-strain curve of the studied steel**

## 5.5 Discussion

### 5.4.1 Microstructure

Based on the in-situ observations in the CLSM and the dilatometry curve, most of the phase transformation happened during cooling from 650 ºC to 500ºC. The transformation appears to have stopped after 10 seconds of holding at 500ºC. The final microstructure in the V+Nb

steel consists of ferrite, lath bainite, and granular bainite. TEM observations indicated many needle-shaped cementite particles with sizes (in length) in the range of 0.4-2 μm. These were observed primarily in the bainitic regions. Based on equilibrium thermodynamic calculations (TCFE9 database of Thermo-Calc) cementite precipitation is possible below 665ºC. The cementite is more frequently observed in the granular bainite compared to lath bainite. This kind of phenomenon has also been reported by other researchers [35, 36].

Nano precipitates containing V and Nb were observed at grain/sub-grain boundaries, dislocations, and cementite particles, as depicted in **Figure 5- 12**. It is worth mentioning that of all the precipitates observed by APT, the precipitates in P1 (lath bainite) contain a lot of N (40%-50%). Less N (20%-30%) is detected in the particles from P2. However, more C is detected in the precipitates in P2 compared to the one in P1. In the high KAM area (P1), the precipitates are distributed around the dislocations/grain boundaries because these defects provide favorable heterogeneous nucleation sites for the precipitates.

A more complex picture emerges in the low KAM area. In the area with cementite (P2), more particles are observed compared to P1. This is a new observation that requires further analysis in the future. One possibility is that micro-alloy precipitates nucleate in proximity to the cementite interface due to the negligible solid solubility of N in the cementite, leading to local enrichment of N in the vicinity of cementite particles. APT appears to offer some support to this argument as N was enriched in the matrix adjacent to the cementite (as shown in Fig S-2 c in the supplementary material). The build-up of N ahead of the

cementite/matrix interface would result in an increase in the driving force for the precipitation of V particles around cementite[37]. Unfortunately, it is not possible to confirm this mechanism based on the small number of observations available in this work and future study is needed to understand the presence of microalloyed precipitates in the vicinity of cementite particles. Farther away from the cementite particles, only V solute clusters were observed.

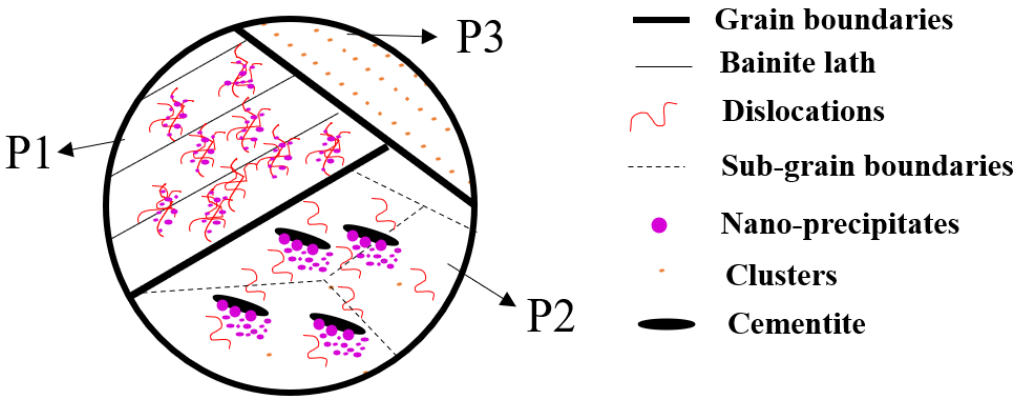


**Figure 5- 12. Schematic of the distribution of nanoparticles in the V-Nb steel.**

In the low KAM area, which is identified as ferrite, precipitates were not observed. This area showed solute clusters that appear to be arranged into sheets/planes. Similar clusters were observed in Timokhina's work [38] and referred to as interphase clusters. Interphase precipitation occurs at the migrating ferrite/austenite interface. Factors changing the ferrite/austenite interphase boundary characters (ferrite/austenite orientation relationship-OR, migration rate, or interfacial concentration) will affect the precipitation behavior [39]. It is also reported that interphase precipitation only occurs at an intermediate transformation

temperature [40]. At higher temperatures, the supersaturation of alloy elements is insufficient to cause interphase precipitation, while at lower temperatures, the growth of ferrite is too rapid without enough time for interphase precipitation to take place. It is speculated that due to the low coiling temperature, the conditions at the interface did not allow these clusters to develop into precipitates in this case.

In summary, precipitates containing V and Nb are distributed heterogeneously in the studied material. Precipitates nucleated on the dislocations and grain/sub-grain boundary at the lath bainite (from High KAM area) and close to the cementite particles in granular bainite (from low KAM area) because these areas provide favorable heterogeneous nucleation sites for the precipitates. Clusters are found in the ferrite area and some of the areas away from the cementite.

### 5.4.2 Mechanical properties

An extended elastoplastic transition is observed in the present steels. This gradual yielding behavior has been reported in various bainitic steels [41, 42] and is usually attributed to the heterogeneity of microstructure as well as the presence of microscopic residual stresses. The dual-phase nature of the microstructure consisting of ferrite and bainite can also promote continuous yielding, similar to DP steels [43].

The YS obtained in this material is lower than the one in the V steel in our previous work [chapter 4]. In order to understand the difference and create high-strength steels by

combining Nb and V in the future, the contributions of the various strengthening mechanisms were estimated. A simple rule of mixtures (iso-strain) was employed to capture the contribution of ferrite and bainite:

$$YS = V_F * YS_F + V_B * YS_B \quad \text{(Equation 5- 1)}$$

where $V_F$ and $V_B$ are the volume fractions of ferrite and bainite, while $YS_F$ and $YS_B$ represent the yield stresses of ferrite and bainite. To explore this further, the contributions of the various strengthening mechanisms were estimated, and added to obtain a first-order approximation of the yield stress of each constituent [8]:

$$YS = \sigma_0 + \sigma_{ss} + \sigma_{iss} + \sigma_g + \sqrt{({\sigma_d}^2 + {\sigma_p}^2)} \quad \text{(Equation 5- 2 )}$$

Here $\sigma_0$ is the lattice friction; $\sigma_{ss}$, $\sigma_{iss}$ are the solid solution strengthening contributions of substitutional and interstitial solutes, respectively. Finally, $\sigma_g$ , $\sigma_d$ and $\sigma_p$ , are the strengthening contributions due to grain refinement, dislocations, and precipitation, respectively. As discussed above, the final microstructure of the sample consisted of ferrite and bainite. Using the EBSD data, the ferrite and bainite could be distinguished based on the presence of the substructure. The volume fraction of these microstructures could be also estimated by the dilatometer result. Based on the present results, a first-order estimate of the volume fractions of bainite ($V_B$) in these samples is around 0.8. In this sample, the bainite laths are no longer visible in some of the large areas of the microstructure as a result of the granularization of bainite. This phenomenon was reported by other researchers and is attributed to the disappearance of high-angle boundaries (~60°) within the bainitic

structure [35, 36]. The lath bainite fraction is estimated to be 0.5 and the granular bainite is around 0.3 based on both the EBSD and SEM results.

The contribution of solid solution strengthening to the yield stress of ferrite has been estimated from the literature [44-47]:

$$\sigma_0 + \sigma_{ss} + \sigma_{iss}\ \text{[MPa]} = 54+32\text{Mn}+83\text{Si}+678\text{P}+39\text{Cu}-31\text{Cr}+11\text{Mo}+5000(C_{free} + N_{free}) \quad \text{(Equation 5- 3)}$$

where the solute content is expressed in mass%. The contribution of V, Nb, etc are considered in the precipitate strengthening. The amount of free carbon in the ferrite was estimated from APT (P3) as ~0.0038 wt.%. The amount of free N is negligible due to the presence of V which ties up the N in the form of VN particles. Using Eq. (5-4), the value of $\sigma_0 + \sigma_{SS} + \sigma_{iss}$ for ferrite obtained in Eq. (5-4) is approximately 155 MPa. Thus, the solid solution contribution from ferrite is around 31 MPa. It is worth mentioning that different equations may be used for the calculation of solution strengthening in steel[44-49]. But it will not influence the result because the value calculated from these equations has no big difference (151-157Mpa for ferrite in this work).

The grain size contribution for ferrite was calculated using the standard Hall-Petch equation:

$$\sigma_{gf} \approx k_y \times d^{-\frac{1}{2}} \quad \text{(Equation 5- 4)}$$

where $k_y$ is 0.55 MPa $m^{0.5}$ for HSLA steels [50] and d is the ferrite grain size. Based on the EBSD data, the mean equivalent diameter was found to be ~9.1 μm when only high-

angle boundaries with misorientation angles over 15° are considered [44, 46, 47, 51, 52]. Thus, the calculated value of $\sigma_{gf}$ is around 182 MPa. It will contribute ~ 36 MPa to the total strength of the studied steel. Given the low dislocation density of ferrite, the contribution due to dislocation strengthening can be ignored. Similarly, precipitate particles were not observed in ferrite and the precipitate hardening contribution is therefore ignored. Thus, the yield strength of ferrite is therefore expected to be of the order of 337 MPa and it would contribute 67 MPa to the total strength of the steel given the ferrite volume fraction is 0.2 in the studied material.

A similar analysis can be performed to estimate the strength of bainite. An estimate of the contributions of intrinsic and solid solution strengthening could be obtained from Eq. (3) with a carbon content of 0.0057 wt% from lath bainite and granular bainite as measured by APT. This leads to a value ~164 MPa. Thus, the solid solution contribution from lath bainite and granular bainite are all around 66 MPa. The grain size contribution of bainite has been the subject of much discussion in the literature[3]. In the following, the strength of bainite is correlated with the lath thickness [46, 47, 50]:

$$\sigma_{gb} \approx 115(\bar{L}_3)^{-1} \qquad \text{(Equation 5- 5)}$$

where $\bar{L}_3(\mu m)$ is a measure of bainite lath width. The values of the lath thickness were found to be of the order of 1 μm in this work (**Figure 5- 2**a), leading to a value of 115 MPa. The lath bainite fraction is 0.5. Thus, the grain-size contribution from lath bainite is around 58 MPa. For the strengthening contribution of granular bainite, it could be estimated using

Eq (5-4) with a grain size around 17 um (distinguished and calculated based on the EBSD and SEM result), leading to a value of around 133 MPa. Thus, the grain-size contribution from granular bainite is around 40 MPa.

The contribution of dislocations to the strength of bainite is calculated using the Taylor equation [44, 46, 47, 50]:

$$\sigma_d = \alpha M \mu b \rho^{0.5} \approx 7.34 \times 10^{-6} \rho_D^{0.5} \qquad \text{(Equation 5- 6)}$$

where α is a constant, M is the average Taylor factor, and αM = 0.38. The shear modulus, μ, is approximated as $8\times10^4$ MPa and b is the magnitude of the Burgers vector ($b\approx2.5\times10^{-10}$ m). The dislocation density is expected to decrease as a function of the holding time. Following Young and Bhadeshia [50], an initial value of the dislocation density in bainitic ferrite can be estimated based on the transformation temperature [50]:

$$\log(\rho_D) = 9.2840 + \frac{6880.73}{T} - \frac{1780360}{T^2} \qquad \text{(Equation 5- 7)}$$

where T is the bainite transformation temperature in kelvin. Based on in-situ observations using the CLSM, T was around 895K, leading to a dislocation density of, $\rho_D \approx 5.6 \times 10^{14} m^{-2}$. It is worth mentioning that the dislocation contribution will decrease with increasing holding time at 500 ºC as a result of the recovery. The granulation of bainite will also reduce the dislocation density. As mentioned before, it is estimated that granular bainite is 50% of the total bainite present based on the TEM observations. It is assumed that half of the dislocations disappear in granular bainite during holding. Thus, the

dislocation density in granular bainite will be around $2.8\times 10^{14} m^{-2}$. Then, the strength increment of dislocations from lath bainite and granular bainite is around 87 MPa and 37 MPa, respectively.

The precipitation hardening contribution to yield strength was estimated by Ashby–Orowan [22, 53] as:

$$\sigma_p = 10.8\frac{\sqrt{f}}{d}\ln(1630d) \qquad \text{(Equation 5- 8)}$$

where $\sigma_p$ represents the precipitation strengthening increment in MPa, f is the volume fraction of the precipitates, and d is the diameter(μm) of the precipitates. Based on the result from APT, when $N_{min} > 15$, the particle number density in lath bainite is around $2.4\times10^{22}$ /m$^3$ with particle size (diameter) around 4.8 nm. While the number density in granular bainite is around $5.6\times10^{22}$ /m$^3$ with particle size(diameter) around 4.1 nm. Thus, the volume fraction of the nanoparticles in lath bainite and granular bainite is around 0.0014 and 0.0020 respectively. Then the nanoparticles in lath bainite and granular bainite would have contributed ~87 MPa and 68 MPa to the yield stress respectively.

A summary of the various contributions to the strength of ferrite and bainite is shown in **Table 5- 1**. Using these values, the YS value of the present Nb-V steel would be around ~495 MPa based on Eq (5-3). This is in relatively good agreement with the measured value (~447 MPa) obtained in **Figure 5- 2**. Interestingly, if the nanoparticles on/close to cementite are ignored, then the calculated YS will be estimated to be around 448 MPa,

which is very close to the experimentally measured YS (~447 MPa). This may be coincidental given the many approximations made when estimating the various strengthening contributions. Nonetheless, the contribution of micro-alloy precipitates which are distributed around cementite particles deserves future investigation. For example, one may speculate that these nanoparticles make a small contribution to strength because their localized distribution in the vicinity of existing cementite particles does not lead to a significant reduction in the dislocation mean free path. In this case, the cementite and the nanoparticles on/close to it could be considered as a single large precipitate which makes a small contribution to the overall strength. If these arguments are accurate, then in order to improve the YS of the studied material, the volume fraction of cementite should be reduced to inhibit the nucleation of the nanoparticles on the cementite.

**Table 5- 1. Calculation results based on Equations 5-(1-8).**

| Strength/Mpa / Microstructure | $\sigma_0 + \sigma_{ss} + \sigma_{iss}$ | $\sigma_g$ | $\sigma_d$ | $\sigma_p$ | Sum |
|---|---|---|---|---|---|
| **Ferrite** | 31 | 36 | / | / | 67 |
| **Lath Bainite** | 82 | 58 | 87 | 87 | 263 |
| **Granular bainite** | 49 | 40 | 37 | 68 | 166 |

## 5.6 Conclusions

The microstructure of a micro-alloy steel containing V and Nb was investigated by advanced characterization techniques including CLSM, EBSD, FIB, TEM, and EBSD. The

difference in precipitates in different areas has been analyzed by site-specific methods. Nano precipitates form preferentially on dislocations and grain/subgrain boundaries within the high KAM areas, identified at lath bainite. Precipitates are observed around cementite in the low KAM areas identified as granular bainite. Interphase clusters were found in the low KAM areas identified as ferrite. Analysis of the results indicates that the precipitation of micro-alloyed particles close to cementite could lower the precipitation hardening contribution that could be achieved by micro alloying. However, the precipitation of micro-alloyed precipitates in the vicinity of cementite particles requires further investigation. In particular, the driving force for the formation of these particles in the vicinity of cementite and their contribution to strengthening need to be determined.

## 5.7 Acknowledgment

The authors would like to acknowledge the sponsorships from EVRAZ North America steel corporations through an NSERC CRD Grant. The authors are grateful to Dr. Fateh Fazeli and Dr. Colin Scott from CanmetMATERIALS (Hamilton, Canada) for the dilatometer experiment and tensile test. The characterization work was carried out at the Canadian Centre for Electron Microscopy, a national facility supported by the Canada Foundation for Innovation under the Major Science Initiative program, NSERC and McMaster University.

## 5.8 Supplementary Data

**Figure 5- 13** presented the nanoparticles distributed around the dislocations in the thin foil TEM sample. The corresponding SAD pattern confirmed the presence of nanoparticles in the matrix, as marked by the circle in Fig S1(d-f).

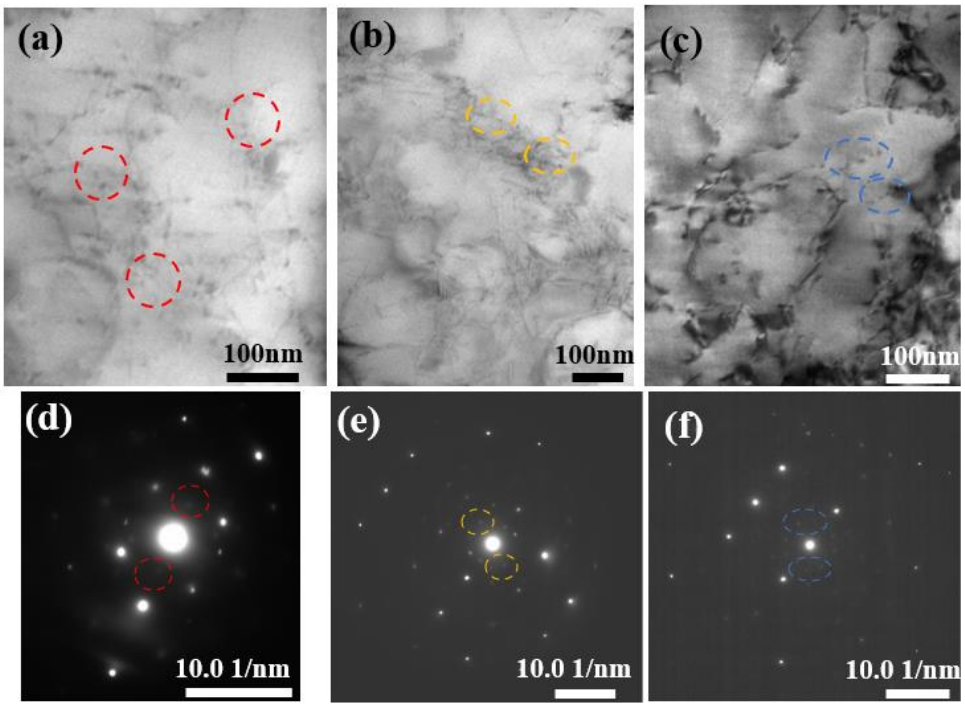


**Figure 5- 13. (a-b) nanoparticles around dislocations and (d-f) corresponding selected diffraction patterns.**

**Figure 5- 14** presents the atomic fraction of V, Nb, C, and N (decomposed)variation of cluster/precipitates vs. Guinier diameter of the cluster/precipitates in P1 and P2. Fig S-2c shows that N is built up at the interface between cementite and ferrite.

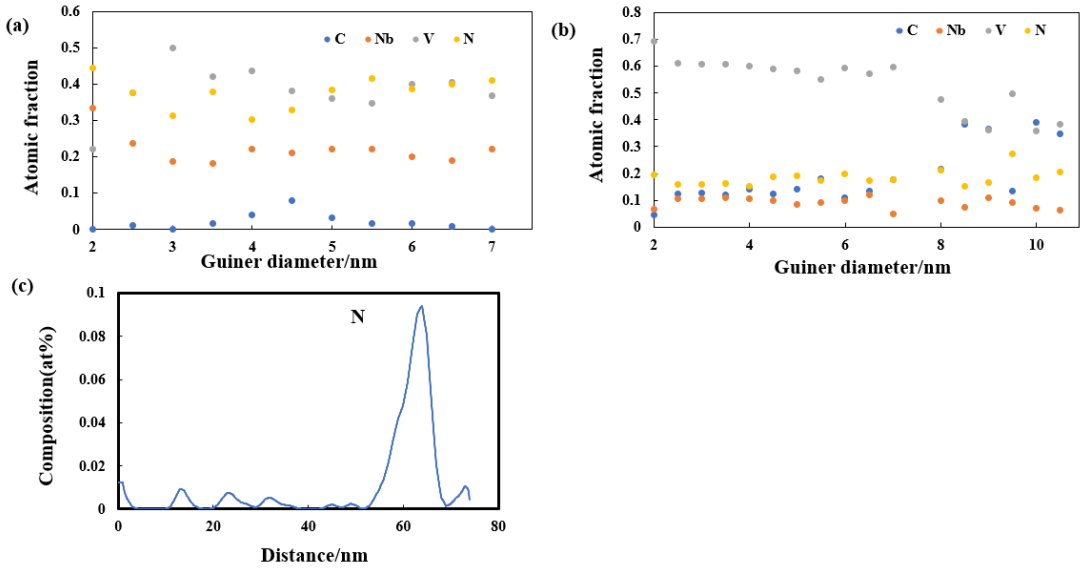


**Figure 5- 14. Atomic fraction of V, Nb, C and N (decomposed)variation of cluster/precipitates vs. Guinier diameter of the cluster/precipitates in (a) P1 and (b)P2. (c) Concentration map of N in the selected area(ROI-1) of P2.**

**Figure 5- 15** shows the 3D atomic map of C, Mn, V, VN Nb and NbN in the tip without cementite. It indicated that only some clusters are observed around the C segregation area.

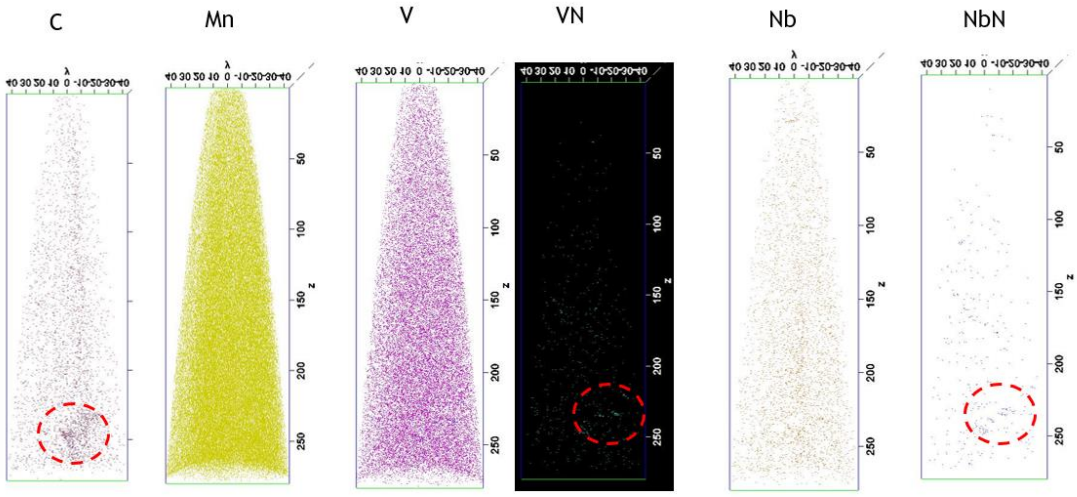


**Figure 5- 15. APT result of V + Nb steel in the high KAM area(p2): 3D atomic map of C, Mn, V, VN Nb and NbN, respectively in the tip without cementite.**

## 5.9 Reference

[1] V.M.H. KONSTRUKCIJSKA, High-strength low-alloy (HSLA) steels, Materiali in tehnologije 45(4) (2011) 295-301.

[2] D. Belato Rosado, W. De Waele, D. Vanderschueren, S. Hertelé, Latest developments in mechanical properties and metallurgical features of high strength line pipe steels, 5th International Conference on Sustainable Construction and Design, Ghent University, Laboratory Soete, 2013.

[3] T. Gladman, The physical metallurgy of microalloyed steels, Maney Pub1997.

[4] A. Davenport, L. Brossard, R. Miner, Precipitation in microalloyed high-strength low-alloy steels, JOM 27(6) (1975) 21-27.

[5] D. Poddar, P. Cizek, H. Beladi, P.D. Hodgson, Evolution of strain-induced precipitates in a model austenitic Fe–30Ni–Nb steel and their effect on the flow behaviour, Acta materialia 80 (2014) 1-15.

[6] H. Dong, H. Chen, W. Wang, Y. Zhang, G. Miyamoto, T. Furuhara, C. Zhang, Z. Yang, S. van der Zwaag, Analysis of the interaction between moving α/γ interfaces and interphase precipitated carbides during cyclic phase transformations in a Nb-containing Fe-C-Mn alloy, Acta Materialia 158 (2018) 167-179.

[7] M. Niu, G. Zhou, W. Wang, M.B. Shahzad, Y. Shan, K. Yang, Precipitate evolution and strengthening behavior during aging process in a 2.5 GPa grade maraging steel, Acta Materialia 179 (2019) 296-307.

[8] Z. Xiong, I. Timokhina, E. Pereloma, Clustering, nano-scale precipitation and strengthening of steels, Progress in Materials Science 118 (2021) 100764.

[9] A. Davenport, F. Berry, R. Honeycombe, Interphase precipitation in iron alloys, Metal Science Journal 2(1) (1968) 104-106.

[10] H.J. Kong, C.T. Liu, A review on nano-scale precipitation in steels, Technologies 6(1) (2018) 36.

[11] A. Pandit, A. Murugaiyan, A.S. Podder, A. Haldar, D. Bhattacharjee, S. Chandra, R. Ray, Strain induced precipitation of complex carbonitrides in Nb–V and Ti–V microalloyed steels, Scripta materialia 53(11) (2005) 1309-1314.

[12] S. Hong, K. Kang, C. Park, Strain-induced precipitation of NbC in Nb and Nb–Ti microalloyed HSLA steels, Scripta materialia 46(2) (2002) 163-168.

[13] C. Gu, M.J. Gaudet, J. Su, B. Langelier, H. Yuan, N. Bassim, H. Zurob, Advanced Characterization of Precipitation and Microstructure Heterogeneity in X70 Steel, Metallurgical and Materials Transactions A (2022) 1-8.

[14] A. Craven, K. He, L. Garvie, T. Baker, Complex heterogeneous precipitation in titanium–niobium microalloyed Al-killed HSLA steels—I.(Ti, Nb)(C, N) particles, Acta Materialia 48(15) (2000) 3857-3868.

[15] X. Ma, C. Miao, B. Langelier, S. Subramanian, Suppression of strain-induced precipitation of NbC by epitaxial growth of NbC on pre-existing TiN in Nb-Ti microalloyed steel, Materials & Design 132 (2017) 244-249.

[16] S. Liang, X. Wang, H.S. Zurob, NbC precipitation during multi-pass deformation of a nickel-based model alloy: Experiments and modelling, Materials Science and Engineering: A 772 (2020) 138748.

[17] S. Liang, X. Wang, C. Andrei, H.S. Zurob, NbC precipitation during two-pass hot deformation of a nickel-based model alloy at 700° C: Experiments and modelling, Materials Science and Engineering: A 802 (2021) 140447.

[18] F. Perrard, A. Deschamps, F. Bley, P. Donnadieu, P. Maugis, A small-angle neutron scattering study of fine-scale NbC precipitation kinetics in the α-Fe–Nb–C system, Journal of Applied Crystallography 39(4) (2006) 473-482.

[19] B. Ma, A study of processing, microstructure and mechanical properties of ultra-high strength microalloyed steel hot band coils for automotive applications, University of Pittsburgh, 2017.

[20] X. Li, H. Li, L. Liu, X. Deng, Z. Wang, The formation mechanism of complex carbides in Nb-V microalloyed steel, Materials Letters 311 (2022) 131544.

[21] X. Li, Z. Wang, X. Deng, Y. Li, H. Lou, G. Wang, Precipitation behavior and kinetics in Nb-V-bearing low-carbon steel, Materials letters 182 (2016) 6-9.

[22] X. Li, Z. Wang, X. Deng, G. Wang, R. Misra, The determining role of finish cooling temperature on the microstructural evolution and precipitation behavior in an Nb-V-Ti microalloyed steel in the context of newly developed ultrafast cooling, Metallurgical and Materials Transactions A 47 (2016) 1929-1938.

[23] C. Li, G. Habler, L.C. Baldwin, R. Abart, An improved FIB sample preparation technique for site-specific plan-view specimens: A new cutting geometry, Ultramicroscopy 184 (2018) 310-317.

[24] L.-H. Lee, C.-H. Yu, C.-Y. Wei, P.-C. Lee, J.-S. Huang, C.-Y. Wen, Plan-view transmission electron microscopy specimen preparation for atomic layer materials using a focused ion beam approach, Ultramicroscopy 197 (2019) 95-99.

[25] K. Thompson, D. Lawrence, D. Larson, J. Olson, T. Kelly, B. Gorman, In situ site-specific specimen preparation for atom probe tomography, Ultramicroscopy 107(2-3) (2007) 131-139.

[26] M.K. Miller, Atom probe tomography: analysis at the atomic level, Springer Science & Business Media2012.

[27] B. Gault, M.P. Moody, J.M. Cairney, S.P. Ringer, Atom probe microscopy, Springer Science & Business Media2012.

[28] Y. Chen, P.H. Chou, E.A. Marquis, Quantitative atom probe tomography characterization of microstructures in a proton irradiated 304 stainless steel, Journal of Nuclear Materials 451(1-3) (2014) 130-136.

[29] R.K. Marceau, A. de Vaucorbeil, G. Sha, S.P. Ringer, W.J. Poole, Analysis of strengthening in AA6111 during the early stages of aging: Atom probe tomography and yield stress modelling, Acta Materialia 61(19) (2013) 7285-7303.

[30] S. Zaefferer, P. Romano, F. Friedel, EBSD as a tool to identify and quantify bainite and ferrite in low-alloyed Al-TRIP steels, Journal of microscopy 230(3) (2008) 499-508.

[31] Y.-W. Chen, Y.-T. Tsai, P.-Y. Tung, S.-P. Tsai, C.-Y. Chen, S.-H. Wang, J.-R. Yang, Phase quantification in low carbon Nb-Mo bearing steel by electron backscatter diffraction technique coupled with kernel average misorientation, Materials Characterization 139 (2018) 49-58.

[32] J. Omale, E. Ohaeri, J. Szpunar, M. Arafin, F. Fateh, Microstructure and texture evolution in warm rolled API 5L X70 pipeline steel for sour service application, Materials Characterization 147 (2019) 453-463.

[33] J. Omale, E. Ohaeri, A. Tiamiyu, M. Eskandari, K. Mostafijur, J. Szpunar, Microstructure, texture evolution and mechanical properties of X70 pipeline steel after different thermomechanical treatments, Materials Science and Engineering: A 703 (2017) 477-485.

[34] S.-I. Lee, S.-Y. Lee, S.G. Lee, H.G. Jung, B. Hwang, Effect of strain aging on tensile behavior and properties of API X60, X70, and X80 pipeline steels, Metals and Materials International 24(6) (2018) 1221-1231.

[35] M. Ben Haj Slama, N. Gey, L. Germain, J.C. Hell, K. Zhu, S. Allain, Fast granularization of lath-like bainite in FeNiC alloys during isothermal holding at Ms+ 20 K (+ 20 C), Metallurgical and Materials Transactions A 47 (2016) 15-18.

[36] M. Ben Haj Slama, N. Gey, L. Germain, K. Zhu, S. Allain, Key parameters to promote granularization of lath-like bainite/martensite in FeNiC alloys during isothermal holding, Materials 11(10) (2018) 1808.

[37] F.A. Khalid, Copper precipitation in M23C6 grain boundary carbides in alloy steel, Scripta materialia 44(5) (2001) 797-801.

[38] I. Timokhina, M.K. Miller, J. Wang, H. Beladi, P. Cizek, P.D. Hodgson, On the Ti-Mo-Fe-C atomic clustering during interphase precipitation in the Ti-Mo steel studied by advanced microscopic techniques, Materials & Design 111 (2016) 222-229.

[39] Y.-J. Zhang, G. Miyamoto, K. Shinbo, T. Furuhara, T. Ohmura, T. Suzuki, K. Tsuzaki, Effects of transformation temperature on VC interphase precipitation and resultant hardness in low-carbon steels, Acta Materialia 84 (2015) 375-384.

[40] T. Sakuma, R. Honeycombe, Microstructures of isothermally transformed Fe-Nb-C alloys, Metal science 18(9) (1984) 449-454.

[41] B. Avishan, C. Garcia-Mateo, L. Morales-Rivas, S. Yazdani, F.G. Caballero, Strengthening and mechanical stability mechanisms in nanostructured bainite, Journal of Materials Science 48 (2013) 6121-6132.

[42] X. Zhang, G. Xu, X. Wang, D. Embury, O. Bouaziz, G.R. Purdy, H.S. Zurob, Mechanical behavior of carbide-free medium carbon bainitic steels, Metallurgical and Materials Transactions A 45 (2014) 1352-1361.

[43] A.A. Sayed, S. Kheirandish, Affect of the tempering temperature on the microstructure and mechanical properties of dual phase steels, Materials Science and Engineering: A 532 (2012) 21-25.

[44] A. Iza-Mendia, I. Gutiérrez, Generalization of the existing relations between microstructure and yield stress from ferrite–pearlite to high strength steels, Materials Science and Engineering: A 561 (2013) 40-51.

[45] I. Gutiérrez, M. Altuna, Work-hardening of ferrite and microstructure-based modelling of its mechanical behaviour under tension, Acta Materialia 56(17) (2008) 4682-4690.

[46] L. García-Sesma, B. López, B. Pereda, Effect of coiling conditions on the strengthening mechanisms of Nb microalloyed steels with high Ti addition levels, Materials Science and Engineering: A 748 (2019) 386-395.

[47] L. Sanz, B. Pereda, B. López, Effect of thermomechanical treatment and coiling temperature on the strengthening mechanisms of low carbon steels microalloyed with Nb, Materials Science and Engineering: A 685 (2017) 377-390.

[48] X. Mao, X. Huo, X. Sun, Y. Chai, Strengthening mechanisms of a new 700 MPa hot rolled Ti-microalloyed steel produced by compact strip production, Journal of Materials Processing Technology 210(12) (2010) 1660-1666.

[49] D.-B. Park, M.-Y. Huh, J.-H. Shim, J.-Y. Suh, K.-H. Lee, W.-S. Jung, Strengthening mechanism of hot rolled Ti and Nb microalloyed HSLA steels containing Mo and W with various coiling temperature, Materials Science and Engineering: A 560 (2013) 528-534.

[50] c.H. Young, H. Bhadeshia, Strength of mixtures of bainite and martensite, Materials Science and Technology 10(3) (1994) 209-214.

[51] Z. Wang, W. Hui, Z. Chen, Y. Zhang, X. Zhao, Effect of vanadium on microstructure and mechanical properties of bainitic forging steel, Materials Science and Engineering: A 771 (2020) 138653.

[52] L. Rancel, M. Gómez, S.F. Medina, I. Gutierrez, Measurement of bainite packet size and its influence on cleavage fracture in a medium carbon bainitic steel, Materials Science and Engineering: A 530 (2011) 21-27.

[53] T. Gladman, Precipitation hardening in metals, Materials science and technology 15(1) (1999) 30-36.

# Chapter 6 A Model for the Competition between Strain-Induced Precipitation and Epitaxial Growth in Microalloyed Austenite

This chapter is reproduced from the work: *Gu, Chen, , Yves Brechet, Fateh Fazeli, Colin Scott, Michael Gaudet, Nabil Bassim, Hatem Zurob. " A Model for the Competition between Strain-Induced Precipitation and Epitaxial Growth in Microalloyed Austenite.”*, which is under review in the Journal of Materials Research and Technology. The author of this thesis is the first author and the main contributor to this publication, including conceiving the initial ideas, development of approach and methodology, carrying out experiments and modeling, analysis of data, and preparation of the manuscript.

## 6.1 Abstract

A model has been developed for describing the competition between the formation of micro-alloyed carbonitrides by strain-induced precipitation (SIP) and by epitaxial growth on pre-existing TiN particles in γ-Fe. It is assumed that Nb and C/N atoms in the matrix will either feed the growth of pre-existing TiN precipitates or precipitate as new strain-induced particles. The model is successfully applied to the data set obtained by transmission electron microscopy (TEM) in a model alloy. Using this model, it is possible to estimate

the effects of process parameters (T, applied strain), the number density of pre-existing TiN, and the Nb, C, N and Mn content on precipitate evolution and precipitation hardening. Notably, it is shown that the presence of a high number density of pre-existing TiN precipitates can suppress SIP. The conditions where epitaxial growth dominates and those in which strain-induced-precipitation dominates are predicted and summarized in the form of processing maps.

**Keywords: HSLA, modelling, strain induced precipitates, epitaxial growth, process map.**

## 6.2 Introduction

High-strength low-alloy steel (HSLA) offers high strength, low impact transition temperature, good weldability and low cost. These steels have been widely used in oil and gas pipelines, and automobile components [1-4]. The precipitation of microalloyed carbonitrides plays an important role in the thermomechanical processing of HSLA steels[1, 3, 5-10]. Precipitation of carbides or carbonitrides is usually in the form of (MX) particles where M= Nb, V, Ti and X=C, N. The formation of a high number density of precipitates leads to the retardation of both recovery and recrystallization by impeding dislocation and grain-boundary movement [3, 8] during thermomechanical processing. Microalloyed precipitates that form during thermomechanical processing are commonly classified as strain-induced precipitates (SIP), interphase precipitates or matrix precipitates [8, 10-14].

Strain-induced precipitation refers to the formation of microalloyed carbonitrides on the dislocations formed during thermomechanical processing [3, 15]. Extensive research has been carried out on the thermodynamics and kinetics of strain-induced precipitation of NbC in austenite and their interaction with recovery and recrystallization [11, 15-19]. Strain-induced precipitation of Nb (C, N) during finish rolling plays the important role of effectively stopping recrystallization, thus allowing strain accumulation which in turn enhances ferrite nucleation on cooling [20-23].

The absence of strain-induced precipitation of NbC is occasionally observed in some Nb-Ti microalloyed steels [24-27]. Quantitative analysis using transmission electron microscopy and 3D atom probe tomography indicates that epitaxial growth of NbC on pre-existing TiN particles can suppress the occurrence of strain-induced precipitation of NbC on dislocations[24, 25]. Ma et al [24] suggested that the inter-spacing of TiN particles is an important parameter influencing the precipitation behavior of NbC during thermomechanical processing. In addition, the role of the dislocation density is found to be very critical in determining the kinetics of strain-induced-precipitation. Although the competition between epitaxial growth on pre-existing particles and strain induced precipitation has been discussed by several authors [24, 28, 29], processing maps for defining the conditions in which each phenomenon dominates have not been developed.

In this work, a new analysis of the competition between SIP and epitaxial growth is presented with special emphasis on the influence of variables such as applied strain,

deformation temperature, the number density of pre-existing TiN particles and steel composition.

## 6.3 Experimental Procedure

In our previous work [25], quantitative characterization of the precipitation NbC in an HSLA steel with 0.042C-1.32Mn-0.27Si-0.006N-0.087Nb-0.017Ti(wt%) was carried out. In spite of the fact that finishing was carried out well below the NbC dissolution temperature, strain-induced precipitates were not observed by transmission electron microscopy (TEM) or 3D atom probe tomography (APT). The absence of strain-induced precipitation was attributed to the depletion of Nb from solid solution as the result of the growth of NbC caps on pre-existing TiN particles.

In this work, the competition between SIP and epitaxial growth of NbC was investigated in an HSLA steel(X70) with 0.038C-1.59Mn-0.24Si-0.0072N-0.075Nb-0.014Ti(wt%). The steel was received in the form of a two-inch industrial transfer bar. Further rolling of this steel was carried out as part of this study, using the pilot rolling mill at CanmetMATERIALS (Hamilton, Canada). The slab was rolled with five passes with a strain around 0.2-0.3 per pass to a final thickness of 15.2 mm. **Figure 6- 1** and **Table 6-1**show the detailed rolling treatment for the 5-pass sample. Direct carbon replicas samples were prepared for 5-pass sample in order to estimate the size distribution of the precipitates.

TEM observations were performed with Philips CM12 and JEOL 2010F TEMs operating at 120 kV and 200 kV, respectively.

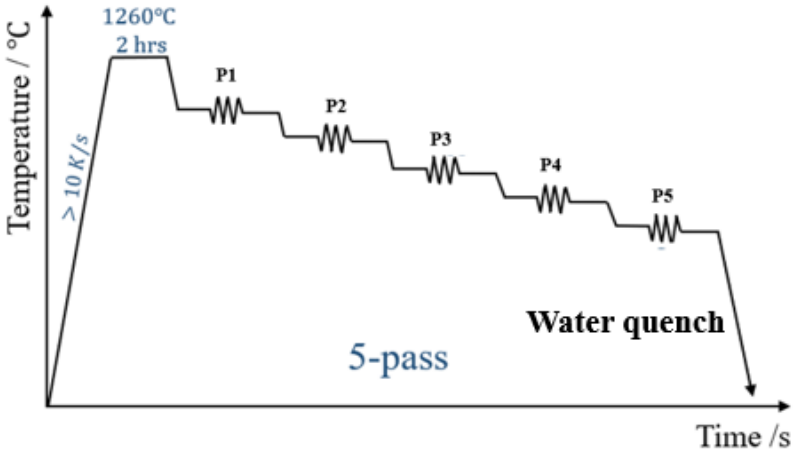


**Figure 6- 1. Processing diagrams for designed 5-pass schedules.**

**Table 6- 1. Processing conditions(measured) of multi-pass rolling.**

| PASS No.: | P1 | P2 | P3 | P4 | P5 |
|---|---|---|---|---|---|
| **Temperature (℃)** | 1068 | 1062 | 1050 | 1030 | 1034 |
| **Strain** | 0.21 | 0.26 | 0.26 | 0.28 | 0.33 |
| **Strain rate ($s^{-1}$)** | 5.31 | 6.47 | 7.32 | 8.52 | 10.61 |
| **Interpass time (s)** | 6.28 | 6.38 | 6.81 | 6.34 | 6.5 |

Examination of the extraction replicas after 5 deformations did not detect any fine precipitate particles, which confirmed the nucleation of new strain induced NbC particles was suppressed in this material too. **Figure 6- 2** shows a typical precipitate found in the

studied steel. Ti and N are mainly distributed in the center of the precipitation, Nb and C are mainly distributed in the outer epitaxial layer and the cap at the top of the figure. The particle size (more than 200 particles) measured is around (diameter) 85nm, as shown in **Figure 6- 3**. The surface density of these precipitates is around 0.3/um$^2$. Thus, the volume density of the precipitates is estimated as $10^{18}$/m$^3$, based on the direct extraction replica results assuming that the replica captured particles within a depth comparable to the particle diameter.

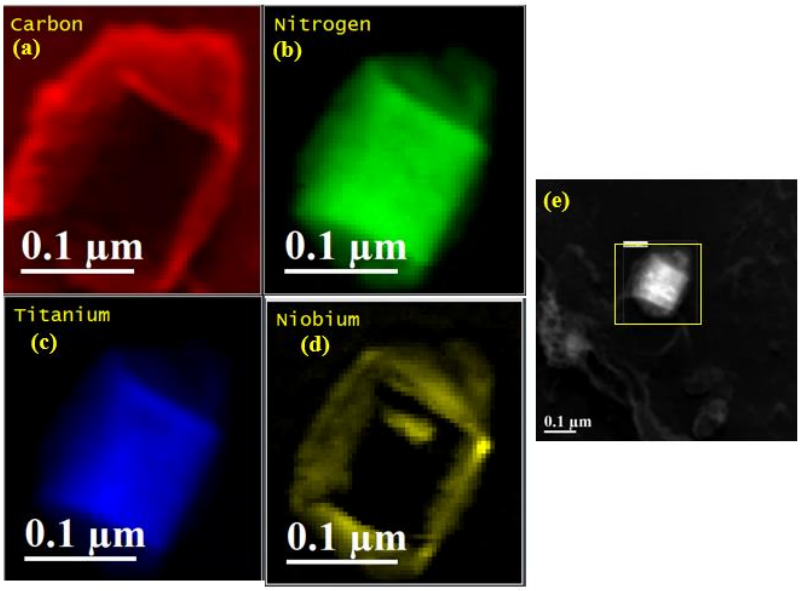


**Figure 6- 2.EELS results of (Ti, Nb) (C, N) in the carbon replica sample.**

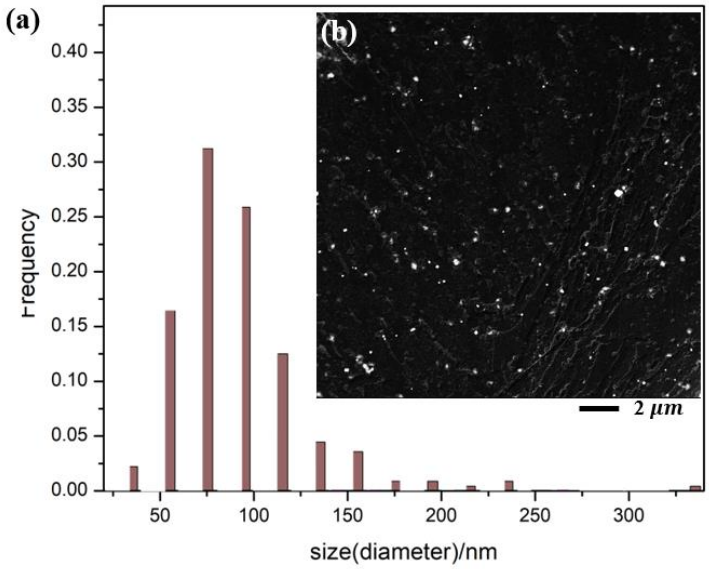


**Figure 6- 3. (a) Particle size of precipitations in 5 pass sample (b)(Ti,Nb)(C,N) precipitates (white particles) in the carbon replica sample**

## 6.4 Description of the Model

As temperature decreases below the solubility temperature for Nb(C,N) it is assumed that Nb atoms in the matrix will either feed the growth of pre-existing TiN particles or precipitate out through the nucleation of new strain-induced particles [24], as shown in **Figure 6- 4**.

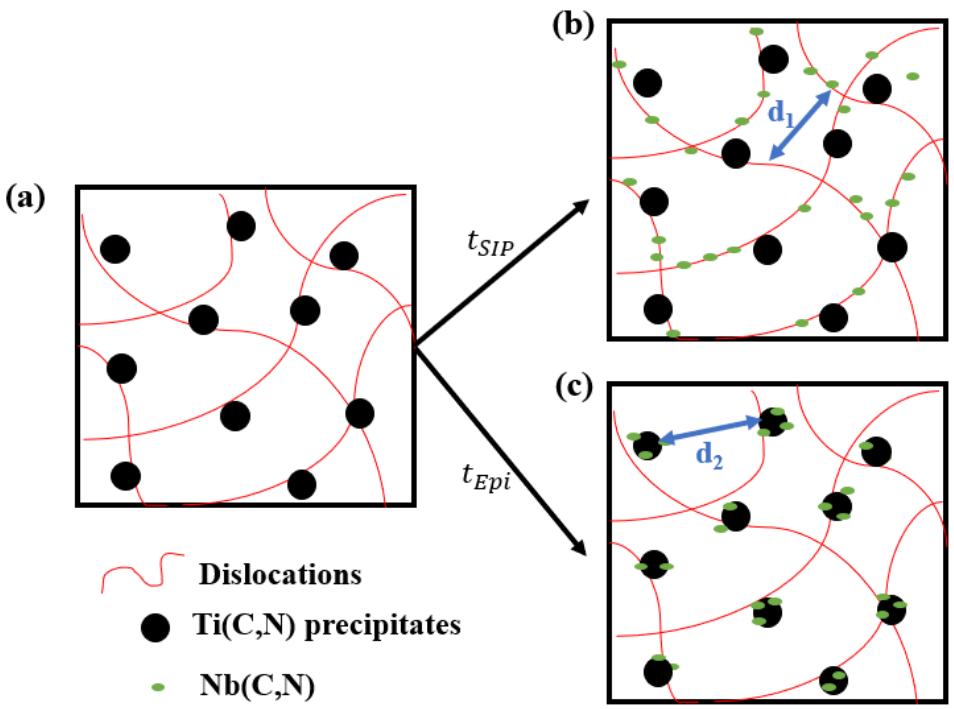


**Figure 6- 4.Schematic of the nucleation of(b) Nb(C, N) on the dislocations and(c) Nb(C,N) on the pre-exit TiN precipitates. ($d_1$ is the distance between dislocation, $d_2$ is the distance between pre-existing TiN precipitates.)**

### 6.4.1 Time for nucleation of SIP on Dislocations($t_{SIP}$)

Following Zurob et al [23], the steady-state nucleation rate for strain-induced precipitation in Nb microalloyed steels under isothermal conditions can be calculated as:

$$\frac{dN}{dt} = \left(1 - \frac{N}{N_{total}}\right)\left(\frac{F\rho}{b}\right)\left(\frac{D_{Nb}^{dis} C_{Nb}}{a^2}\right)\exp\left(\frac{-\Delta G_n}{K_B T}\right) \qquad \text{(Equation 6-1 )}$$

where $N_{total}$ is the number of nucleation sites and an Avrami-type term ($1-N/N_{total}$) has been added to the classical nucleation equation to account for the progressive consumption of

available nucleation sites. The density of nucleation sites was approximated as Fρ/b, where F is an adjustable factor smaller than unity (0.0025 is used in this work). ρ is the total dislocation density and b is the magnitude of the Burgers vector. $C_{Nb}$ is the instantaneous concentration of Nb in solution (expressed as the atom fraction) and a is the lattice parameter. $\Delta G_n$ is the activation barrier for the nucleation process and $K_B$ is the Boltzmann constant. $D_{Nb}^{dis}$ is the pipe/dislocation diffusion coefficient of Nb in austenite, which can be estimated as [3]:

$$D_{Nb}^{dis} = 4.1 \times 10^{-4} \times e^{\left(\frac{-172500\ J}{RT}\right)}\ m^2/s \qquad \text{(Equation 6-2)}$$

where R is the gas constant and T is the absolute temperature.

The nucleation rate, dN/dt, is calculated at each time step, leading to a time-dependent nucleation rate [30]. An incubation time was not explicitly introduced in Eq. (6-1). This is acceptable because in the case of the present steels, a large number of particles (e.g. $>10^{18}/m^3$) must be present in order to influence microstructure evolution. The time needed for this large number of particles to form introduces a delay/incubation time. For the purpose of examining the competition between strain-induced precipitation and epitaxial growth, the time($t_{SIP}$) needed to produce at least as many strain-induced precipitates as the number of pre-existing TiN particles was calculated by using Eq.6-1.

### 6.4.2 Time for diffusion to an existing particle ($t_{Epi}$)

The time, $t_{Epi}$, needed for the Nb(C,N) caps on TiN particles to deplete the Nb present along a dislocation which is connected to the TiN particle, can be estimated based on the nominal diffusion distance, L:

$$L = \sqrt{D_{Nb}^{dis} t_{\mathrm{Epi}}} = \frac{d_2}{2} \qquad \text{(Equation 6-3 )}$$

As before, $D_{Nb}^{dis}$ is calculated using Eq.2, $d_2$ is the average distance between 2 existing TiN particles, which equals $1/N_{lin}$, $N_{lin}$ is the linear density of the TiN, which is calculated as:

$$N_{lin} \approx \sqrt[3]{N_v} = \frac{1}{d_2} \qquad \text{(Equation 6-4)}$$

In this equation, $N_v$ is the volume number density of pre-existing TiN particles. By combining equations6-(3-4), the representative time for diffusion to an existing precipitate can be written as:

$$t_{\mathrm{Epi}} = \frac{1}{4N_{lin}^2 D_{Nb}^{disl}} \qquad \text{(Equation 6-5 )}$$

This time captures the growth of Nb(C, N) on the existing TiN without needing an extra nucleation time. $t_{Epi}$ would give an indication of how quickly the Nb can be removed from the area where it is needed to initiate SIP (i.e., dislocation).

### 6.4.3 Competition

The competition between strain-induced precipitation and epitaxial growth can be considered in terms of the characteristic times for the two processes, namely, $t_{SIP}$ and $t_{Epi}$. If $t_{SIP} > t_{Epi}$, it would take a longer time to nucleate Nb(C, N) on dislocations than to add Nb to pre-existing TiN particles. Under these conditions, precipitation of strain-induced NbC will be suppressed. When $t_{SIP} < t_{Epi}$, the SIP will nucleate on dislocations much faster than solute can be added to existing particles[28]. The critical temperature, $T_c$, is the temperature at which $t_{SIP} = t_{Epi}$ for a fixed applied strain and a fixed number of pre-existing TiN particles. $T_c$ can be used to quantify the competition between the two processes. When the deformation temperature is lower than $T_c$, SIP will dominate. If the temperature is higher than $T_c$, SIP will be suppressed, as described in **Figure 6- 5**.

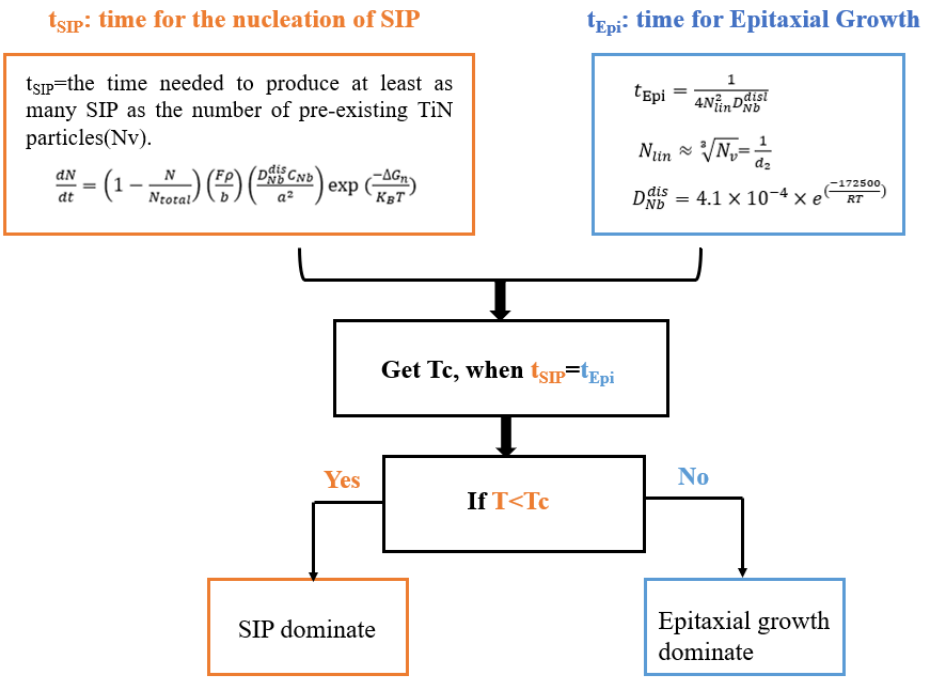

**Figure 6- 5. The workflow in the present model.**

## 6.5 Processing Maps

Processing maps were computed based on the composition of the X70 material which was listed in the experimental section. **Figure 6- 6** shows the dependence of $t_{SIP}$ and $t_{Epi}$ on temperature when the applied strain is 0.2 and the number density of TiN particles is $10^{18}(m^{-3})$. The figure is plotted based on the result calculated using Eqs 6-(1-5). It is clear that $t_{SIP}$ increases with increasing temperature due to the increase in the activation energy for nucleation, while $t_{Epi}$ decreased with increasing temperature due to the increase in the diffusion coefficient of Nb. The critical temperature $T_c$ (when $t_{SIP}=t_{Epi}$) in this example is 967℃. This suggests that when the deformation temperature is higher than 967℃, SIP will be suppressed. That is to say, SIP will dominate only below 967℃.

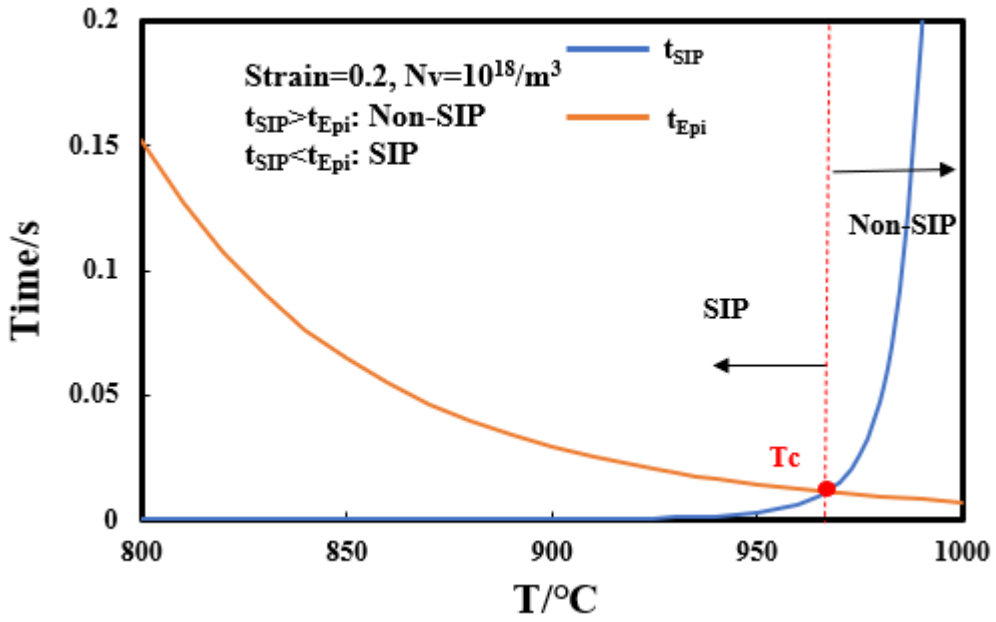

**Figure 6- 6. Time ($t_{SIP}$ and $t_{Epi}$) vs T graph when applied strain is 0.2 and the number density of pre-existing TiN is $10^{18}(m^{-3})$ for the studied X70 steel.**

### 6.5.1 Effect of strain

The time for the nucleation of SIP, $t_{SIP}$, is affected by strain because nucleation takes place on the dislocations created by the deformation process (Eq.6-1). In contrast, $t_{Epi}$ is, to a first order, independent of strain. As shown in **Figure 6- 7**a, when the strain is increased, $t_{SIP}$ will decrease, making it is easier to get SIP when the applied strain is large. The change of the critical temperature ($T_c$) with applied strain is shown in **Figure 6- 7**b. The curve shows that when the applied strain is increased, the critical temperature $T_c(t_{SIP}=t_{Epi})$ will increase too, meaning that the temperature range in which SIP dominates is enlarged. **Figure 6- 7**b also indicates that if the applied strain is fixed, the critical temperature ($T_c$) will decrease with the increasing number density of TiN. Consequently, the nucleation of SIP would be restricted to lower temperatures. Interestingly, when the applied strain is increased from 0.03 to 1, $T_c$ will only change by ~10°C for $N=10^{17}/m^3$ and by ~60°C for $N=10^{19}/m^3$. This shows that the effect of strain is closely linked to the number of pre-existing TiN particles. This point is discussed in detail in the following section.

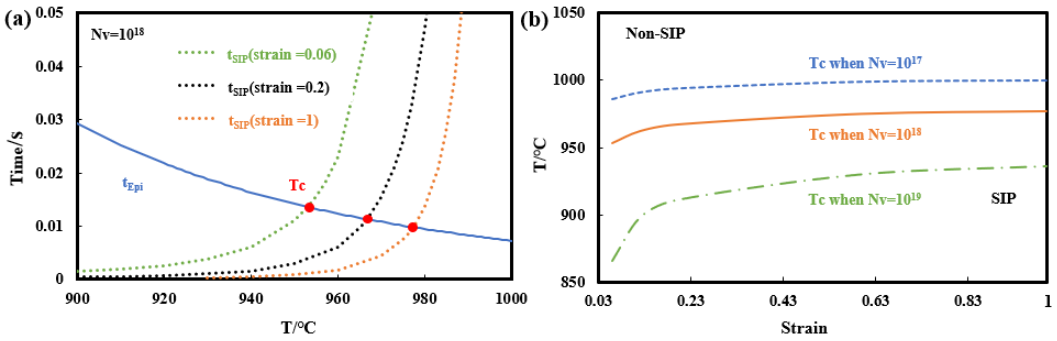


**Figure 6- 7. (a)Effect of applied strain (0.06, 0.2 and 1) on $t_{SIP}$, $t_{Epi}$ and $T_c$ when the pre-existing TiN number density ($N_v$) is $10^{18}(m^{-3})$. (b) Effect of applied strain (0.03-1) on the $T_c$ when the $N_v$ is $10^{17}$, $10^{18}$ and $10^{19}$ $(m^{-3})$ respectively.**

### 6.5.2 Effect of the number of pre-existing TiN particles

The number density of the pre-existing TiN particles is a key parameter influencing the nucleation of SIP during thermomechanical processing[24]. The relationship between time, temperature and number density of pre-existing TiN particles is shown in **Figure 6- 8**. At a fixed temperature, $t_{SIP}$ increases with the increasing number density of TiN particles because $t_{SIP}$ was defined as the time needed for the number of strain-induced precipitates to exceed the number of pre-existing TiN particles. In contrast, $t_{Epi}$ decreases as the number of TiN particles increases (smaller diffusion distance), as shown in **Figure 6- 8**b.

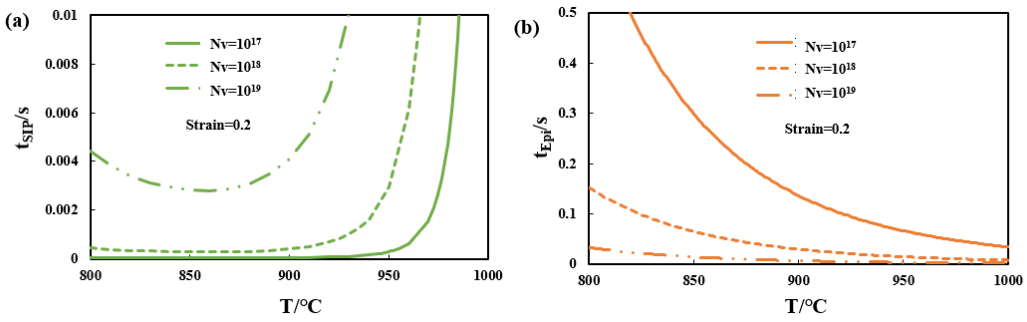


**Figure 6- 8. Effect of pre-existing TiN number density ($N_v/m^{-3}$) on (a) $t_{SIP}$ and (b) $t_{Epi}$ when applied strain=0.2.**

The effect of pre-existing number density of TiN on the critical temperature ($T_c$) was presented in **Figure 6- 7**b. The result shows that if the applied strain is fixed, the nucleation of SIP would be restricted to lower temperatures with an increasing number density of TiN. It is worth mentioning that if the pre-existing TiN number density is smaller than $10^{16}/m^3$, $t_{Epi}$ will always be higher than $t_{SIP}$, which means, SIP will dominate at all temperatures, as shown in **Figure 6- 9**a. However, if the pre-existing TiN number density is larger than $10^{20}/m^3$, $t_{Epi}$ will always be lower than $t_{SIP}$, which means, SIP will not take place no matter what the temperature is, as shown in **Figure 6- 9**b. Such a high number density of TiN particles, however, is not expected. This result may, however, offer an insight into what happens during multi-pass rolling. If a large number of strain-induced precipitates, Nb(C,N) is formed after the first pass, then additional nucleation is not expected after subsequent deformation passes because the number density of precipitates formed after the first pass is typically > $10^{20}$ $m^{-3}$[21, 31], the residual Nb atoms will diffuse to the pre-existing NbC particles instead of nucleating new SIP.

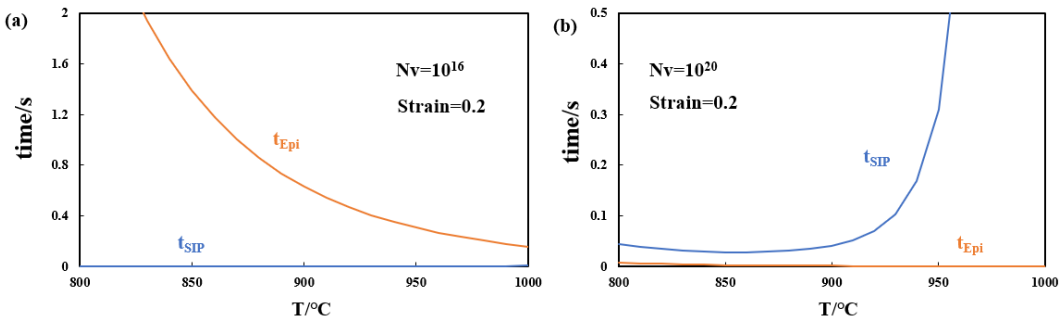


**Figure 6- 9. Time ($t_{SIP}$ and $t_{Epi}$) vs T graph with the number density of pre-existing TiN around (a)$10^{16}$ and (b)$10^{20}$($m^{-3}$) and applied strain=0.2.**

### 6.5.3 Effect of composition

It is worth mentioning that the change of the composition (Nb, C, N, Mn, etc) will also influence the critical temperature, $T_c$. **Figure 6- 10** shows the effect of Nb on $T_c$ when the applied strain is 0.2 and the number density of pre-existing TiN particles is around $10^{18}$($m^{-3}$). The result shows that the $T_c$ increases with the increasing Nb content, which suggests that it will be easier to get SIP in steels with more Nb. The same effect is seen for C and N as both contribute to increasing the driving force for precipitation. Smaller effects are observed for elements like Mn which modify the solubility product of Nb(C,N) and consequently have an indirect effect on $T_c$. The addition of Mn increases the solubility of Nb(C,N) in austenite ad as a result, $T_c$ will decrease with increasing Mn, which means that it will be more difficult to get SIP with higher Mn contents.

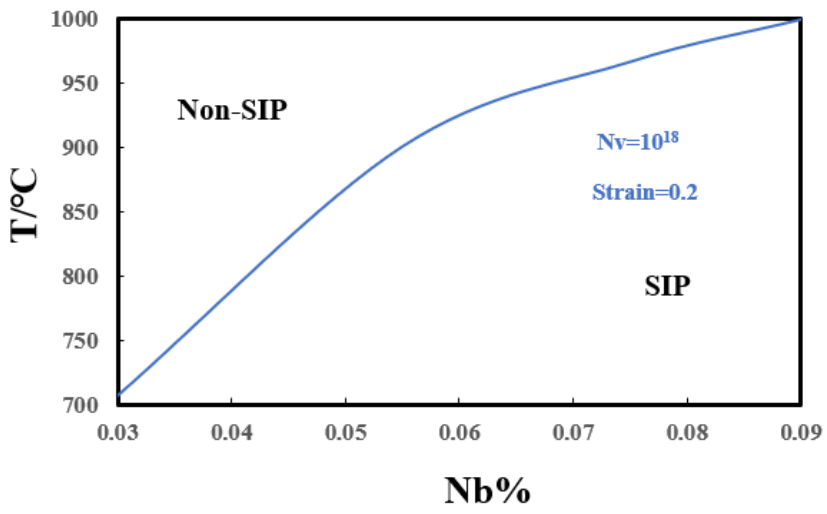


**Figure 6- 10. Effect of Nb% on $T_c$ for a TiN particle number density of $10^{18}$ $m^{-3}$ and an applied strain=0.2.**

### 6.5.4. Comparison to Experimental Data

For the X70 steel, which was studied in this work, the number density of pre-existing TiN particles was estimated to be ~ $10^{18}$ /$m^3$. Using an applied strain of 0.2, the calculated value of $T_c$ is ~967℃. Referring back to **Table 6- 1**, multi-pass deformation of the present steel was carried out above 1000ºC. The absence of SIP in the rolled samples can, therefore, be interpreted in terms of the suppression of SIP due to deformation taking place above $T_c$.

A similar calculation was made on the material the steel used in the study by Ma et al (0.05C-0.090Nb-0.0040N-1.95Mn) [24]. The rough rolling temperature used in his work was around 940 °C and the finish rolling was performed in the temperature range of 930°C–830 °C. Ma et al [24] reported that the volume fraction of pre-existing TiN particles was 0.00177 and the diameter was around 45nm. Thus, the number density of the pre-existing

TiN particles can be estimated very roughly as $10^{19}/m^3$. Using an applied strain of 0.2, $T_c$ was calculated to be around 830°C. This again suggests that SIP is suppressed under the processing conditions used by Ma et al [24].

As mentioned in the experiment section, our previous work [25] also reported the absence of SIP in an HSLA steel with 0.042C-1.32Mn-0.006N-0.087Nb-0.017Ti(wt%). Roughing was carried out between 1080 and 1030°C and finishing deformation was carried out between 920 and 820°C. The number density of the pre-existing TiN was reported to be ~ $10^{19}/m^3$. Using these values, $T_c$ is calculated to be ~885°C if the applied strain is 0.2. This would imply that SIP should have taken place in [25]. In reality, the situation is more complex due to the dynamic evolution of Nb, C and N during hot rolling. For the above steel, the dissolution temperature of Nb(C,N) is calculated to be 1150°C. As a result, epitaxial growth during roughing and early stages of finishing (above 885°C) could deplete Nb, C and N from the matrix. This will in turn reduce the driving force for SIP. As a result, $T_c$ would be expected to evolve during themomechanical processing. In general, $T_c$ is expected to gradually increase during themomechanical processing due to more strain accumulation. However, the decrease of $T_c$, due to the gradual depletion of Nb from solution may explain the suppression of SIP in our previous work [25].

## 6.6 Conclusions

A simple model has been developed to capture the competition between strain-induced precipitation and epitaxial growth. Using this model, it is possible to estimate the effects

of process parameters (T, applied strain), the number density of pre-existing TiN particles and steel composition on the precipitation process. $T_c$, which is the critical formation temperature of SIP, is calculated in this model. When $T>T_c$, SIP will be suppressed. The calculations suggest that Tc will increase with the increasing applied strain, decreasing the number density of pre-existing TiN particles, increasing Nb, C and N contents, and decreasing Mn content. Notably, the number density of pre-existing TiN particles and steel composition has the largest effect on $T_c$. Therefore, it is essential to control the number density of TiN particles in order to optimize SIP.

## 6.7 Acknowledgements

The authors would like to acknowledge the sponsorship from EVRAZ North America through an NSERC CRD Grant. The characterization work was carried out at the Canadian Centre for Electron Microscopy, a national facility supported by the Canada Foundation for Innovation under the Major Science Initiative program, NSERC and McMaster University.

## 6.8 Reference

[1] V.M.H. KONSTRUKCIJSKA, High-strength low-alloy (HSLA) steels, Materiali in tehnologije 45(4) (2011) 295-301.

[2] D. Belato Rosado, W. De Waele, D. Vanderschueren, S. Hertelé, Latest developments in mechanical properties and metallurgical features of high strength line pipe steels, 5th International Conference on Sustainable Construction and Design, Ghent University, Laboratory Soete, 2013.

[3] T. Gladman, The physical metallurgy of microalloyed steels, Maney Pub1997.

[4] A. Davenport, L. Brossard, R. Miner, Precipitation in microalloyed high-strength low-alloy steels, JOM 27(6) (1975) 21-27.

[5] M. Charleux, W. Poole, M. Militzer, A. Deschamps, Precipitation behavior and its effect on strengthening of an HSLA-Nb/Ti steel, Metallurgical and Materials Transactions A 32 (2001) 1635-1647.

[6] W. Bleck, E. Ratte, Fundamentals of Cold Formable HSLA Steels, International Symposium on Niobium Microalloyed Sheet Steel for Automotive Application, S. Hashimoto, S. Jansto, H. Mohrbacher, F. Siciliano, Eds. TMS (The Minerals, Metals & Materials Society), 2006, pp. 551-564.

[7] T. Gladman, Precipitation hardening in metals, Materials science and technology 15(1) (1999) 30-36.

[8] Z. Xiong, I. Timokhina, E. Pereloma, Clustering, nano-scale precipitation and strengthening of steels, Progress in Materials Science 118 (2021) 100764.

[9] F. Bu, X. Wang, S. Yang, C. Shang, R. Misra, Contribution of interphase precipitation on yield strength in thermomechanically simulated Ti–Nb and Ti–Nb–Mo microalloyed steels, Materials Science and Engineering: A 620 (2015) 22-29.

[10] H.J. Kong, C.T. Liu, A review on nano-scale precipitation in steels, Technologies 6(1) (2018) 36.

[11] D. Poddar, P. Cizek, H. Beladi, P.D. Hodgson, Evolution of strain-induced precipitates in a model austenitic Fe–30Ni–Nb steel and their effect on the flow behaviour, Acta materialia 80 (2014) 1-15.

[12] H. Dong, H. Chen, W. Wang, Y. Zhang, G. Miyamoto, T. Furuhara, C. Zhang, Z. Yang, S. van der Zwaag, Analysis of the interaction between moving α/γ interfaces and interphase precipitated carbides during cyclic phase transformations in a Nb-containing Fe-C-Mn alloy, Acta Materialia 158 (2018) 167-179.

[13] M. Niu, G. Zhou, W. Wang, M.B. Shahzad, Y. Shan, K. Yang, Precipitate evolution and strengthening behavior during aging process in a 2.5 GPa grade maraging steel, Acta Materialia 179 (2019) 296-307.

[14] A. Davenport, F. Berry, R. Honeycombe, Interphase precipitation in iron alloys, Metal Science Journal 2(1) (1968) 104-106.

[15] B. Dutta, E.J. Palmiere, C.M. Sellars, Modelling the kinetics of strain induced precipitation in Nb microalloyed steels, Acta materialia 49(5) (2001) 785-794.

[16] P. Gong, E.J. Palmiere, W.M. Rainforth, Characterisation of strain-induced precipitation behaviour in microalloyed steels during thermomechanical controlled processing, Materials Characterization 124 (2017) 83-89.

[17] S.F. Medina, A. Quispe, M. Gomez, Model for strain-induced precipitation kinetics in microalloyed steels, Metallurgical and Materials Transactions A 45(3) (2014) 1524-1539.

[18] Z. Wang, X. Mao, Z. Yang, X. Sun, Q. Yong, Z. Li, Y. Weng, Strain-induced precipitation in a Ti micro-alloyed HSLA steel, Materials Science and Engineering: A 529 (2011) 459-467.

[19] S. Hong, K. Kang, C. Park, Strain-induced precipitation of NbC in Nb and Nb–Ti microalloyed HSLA steels, Scripta materialia 46(2) (2002) 163-168.

[20] H. Zurob, Effects of precipitation, recovery and recrystallization on the microstructural evolution of microalloyed austenite, 2003.

[21] S. Liang, X. Wang, H.S. Zurob, NbC precipitation during multi-pass deformation of a nickel-based model alloy: Experiments and modelling, Materials Science and Engineering: A 772 (2020) 138748.

[22] H. Zurob, Y. Brechet, G. Purdy, A model for the competition of precipitation and recrystallization in deformed austenite, Acta materialia 49(20) (2001) 4183-4190.

[23] H. Zurob, C. Hutchinson, Y. Brechet, G. Purdy, Modeling recrystallization of microalloyed austenite: effect of coupling recovery, precipitation and recrystallization, Acta materialia 50(12) (2002) 3077-3094.

[24] X. Ma, C. Miao, B. Langelier, S. Subramanian, Suppression of strain-induced precipitation of NbC by epitaxial growth of NbC on pre-existing TiN in Nb-Ti microalloyed steel, Materials & Design 132 (2017) 244-249.

[25] C. Gu, M.J. Gaudet, J. Su, B. Langelier, H. Yuan, N. Bassim, H. Zurob, Advanced Characterization of Precipitation and Microstructure Heterogeneity in X70 Steel, Metallurgical and Materials Transactions A (2022) 1-8.

[26] A. Craven, K. He, L. Garvie, T. Baker, Complex heterogeneous precipitation in titanium–niobium microalloyed Al-killed HSLA steels—I.(Ti, Nb)(C, N) particles, Acta Materialia 48(15) (2000) 3857-3868.

[27] H. Zhang, H. Xiong, First-principles study of NbC heterogeneous nucleation on TiC vs. TiN in microalloy steel, Ironmaking & Steelmaking (2018).

[28] F. Perrard, A. Deschamps, P. Maugis, Modelling the precipitation of NbC on dislocations in α-Fe, Acta Materialia 55(4) (2007) 1255-1266.

[29] A. Deschamps, Y. Brechet, Influence of predeformation and ageing of an Al–Zn–Mg alloy—II. Modeling of precipitation kinetics and yield stress, Acta Materialia 47(1) (1998) 293-305.

[30] S. Liang, Thermomechanical processing of microalloyed steels: experiments and modelling, 2020.

[31] S. Liang, X. Wang, C. Andrei, H.S. Zurob, NbC precipitation during two-pass hot deformation of a nickel-based model alloy at 700° C: Experiments and modelling, Materials Science and Engineering: A 802 (2021) 140447.

# Chapter 7 Conclusions and Future Works

The aim of the current project is to use advanced characterization techniques to understand the relationship between the precipitates and different microstructures and develop a model for the competition of different precipitates. To accomplish these objectives, site-specific characterization techniques (CLSM, EBSD, FIB, TEM, and APT) were correlatively used to analyze the precipitates in different areas during rolling and coiling in the HSLA steel. A model for the competition of strain-induced precipitates and (Ti, Nb) (C, N) in γ-Fe was also created. The following conclusions can be drawn here:

1. The spatial distribution of precipitates and microstructure heterogeneity in X70 steel were investigated using advanced characterization techniques in this paper. Firstly, SIP of fine (2-10 nm) NbC particles on dislocations were not observed. The absence of SIP is believed to be due to the depletion of Nb from the solid solution because of the core-cap structure of NbC on pre-existing TiN particles. Secondly, core-cap structure precipitates (30-70 nm in diameter) (Ti, Nb) (C, N) were distributed homogenously in the studied steel because of the homogeneous distribution of TiN prior to hot rolling. The precipitate number density in the different regions is all about $10^{19}$ $m^{-3}$. This indicates that variations of grain size and KAM within the microstructure were not correlated with variations in the distribution of microalloyed precipitates in the studied material.

2. For the study on the evolution of the microstructure and mechanical properties in V-containing microalloyed steel during coiling: Fine nano precipitates (<10 nm) containing V and N were heterogeneously distributed. In samples S1, S2, and S3, VN-containing nano precipitates (< 5 nm) were most often found in the high KAM value areas. The particle size of nano precipitates increased with increasing holding time. The heterogeneous distribution of the nano precipitates at the early stages of isothermal holding is explained by higher dislocation densities in the high KAM value areas. These dislocations act as nucleation sites for the precipitates. An extended elastoplastic transition is observed in the present steels. An extended elastoplastic transition is observed in the present steels. This is most evident in the 80s sample and is attributed to the heterogeneity of the microstructure as well as the presence of microscopic residual stresses. The YS was lowest for S1 and increased for longer aging times. The limited increase of YS suggests that the contribution of precipitation strengthening is partially offset by the softening associated with the recovery of dislocation and granularization of bainite.
3. For the microstructure of a micro-alloyed steel containing V and Nb. Nano precipitates form preferentially on dislocations and grain/subgrain boundaries within the high KAM areas, identified at lath bainite. Precipitates are observed around cementite in the low KAM area from granular bainite. Interphase clusters were found in the low KAM area from ferrite. A small precipitation hardening contribution to the yield stress is observed in spite of the high number density of precipitate particles. This may be attributed to the fact that a large fraction of the micro-alloyed precipitates form in the vicinity of pre-

existing cementite particles and therefore do not contribute to reducing the dislocation mean free path. Reducing the extent of cementite precipitation may therefore contribute to a greater strengthening from microalloying additions.

4. A competition model has been developed specifically for the case where precipitation occurs on dislocations and pre-exists TiN. Using this model, it is possible to estimate the effects of process parameters (T, applied strain), pre-existing TiN number density and the composition on the final microstructure. Notably, it is shown that the number density of pre-existing TiN precipitates and composition have a pronounced influence on the nucleation of SIP. Given the alloy composition, the model is able to predict the precipitation of NbC by selecting desired temperature range, applied strain and number density of pre-existing TiN precipitates.

The aim to understand the relationship between the precipitates and different microstructures and develop the models has been accomplished during the course of Ph.D studies. This work provides a relatively new workflow to investigate the precipitates within the steel, especially in site-specific areas. However, there still are some interesting works worth investigating in the future.

- The cooling rate is different at different positions in the hot rolled sheet. If the cooling rate at the surface of the hot rolled sheet is around 30℃/s, the cooling rate at the quarter point will be around 15-20 ℃/s [1]. It is worth studying the effect of cooling rate on the phase transformation to better understand differences in the precipitate distribution at different points in the thickness.

- The precipitation of micro-alloyed precipitates in the vicinity of cementite particles requires further investigation. In particular, the driving force for the formation of these particles in the vicinity of cementite and their contribution to strengthening need to be determined.
- Besides, more research is needed to investigate the transformation from clusters to precipitates. The cluster density and precipitate density in different areas and their effect on the mechanical properties need to be quantified, respectively.
- Lastly, more experimental data is needed to make the competition model more robust.

[1] B. Wang, Z.-d. Wang, B.-x. Wang, G.-d. Wang, R. Misra, The relationship between microstructural evolution and mechanical properties of heavy plate of low-mn steel during ultra fast cooling, Metallurgical and Materials Transactions A 46 (2015) 2834-2843.